AFRL-SR-AR-TR-05-

0078

REPORT DOCUMENTATION PAGE

1. AGENCY USE ONLY (Leave Blank)	2. REPORT DATE 02/23/05	3. REPORT TYPE AND DATES COVERED Final (12/01/01 - 11/30/04)

4. TITLE AND SUBTITLE	5. FUNDING NUMBERS
Transition in High-Speed Boundary Layers: Numerical Investigations Using DNS and LES	F49620-~~2-1-0077~~ 02-1-0077

6. AUTHOR(S)

Dr. Hermann F. Fasel

7. PERFORMING ORGANIZATION NAME(S) AND ADDRESS(ES)	8. PERFORMING ORGANIZATION REPORT NUMBER
Department of Aerospace & Mechanical Engineering, College of Engineering, University of Arizona, Tucson, AZ 85721	

9. SPONSORING / MONITORING AGENCY NAME(S) AND ADDRESS(ES)	10. SPONSORING / MONITORING AGENCY REPORT NUMBER
USAF, AFRL AF Office of Scientific Research 4015 Wilson Blvd., Room 713 Arlington, VA 22203-1954	

11. SUPPLEMENTARY NOTES

12 a. DISTRIBUTION / AVAILABILITY STATEMENT	12 b. DISTRIBUTION CODE
Approved for public release; distribution unlimited.	

13. ABSTRACT (Maximum 200 words)

Direct Numerical Simulations (DNS) of supersonic flow over a flat-plate with and without adverse pressure-gradient at Mach 3 were carried out in close collaboration with the experimental effort at Princeton University by G. Brown and co-workers. To confirm that simulations and experiments were based on the same "baseflow," the experimental baseflow profiles were compared with our Navier--Stokes results. The downstream development and the spatial growth rates of the disturbances obtained from the Navier--Stokes computations and from experimental measurements were compared as well. Overall, a remarkably good agreement was achieved. Towards the understanding of the nonlinear mechanisms, we investigated numerous nonlinear resonance and breakdown scenarios. Our simulations have shown that due to the stabilizing effects of compressibility for supersonic boundary layers, the transition process can be stretched significantly in the downstream direction and sometimes the transition process may even be aborted so that a turbulent boundary layer is never fully established. The extent of the transition process and the intensity of the temperature fluctuations, and the resulting heat load, depend strongly on the nonlinear mechanisms.

14. SUBJECT TERMS		15. NUMBER OF PAGES 124
		16. PRICE CODE

17. SECURITY CLASSIFICATION OR REPORT UNCLASSIFIED	18. SECURITY CLASSIFICATION ON THIS PAGE UNCLASSIFIED	19. SECURITY CLASSIFICATION OF ABSTRACT UNCLASSIFIED	20. LIMITATION OF ABSTRACT UL

Enclosure 1

TRANSITION IN HIGH-SPEED BOUNDARY LAYERS: NUMERICAL INVESTIGATIONS USING DNS AND LES

A Final Report by

Hermann F. Fasel

Department of Aerospace and Mechanical Engineering
The University of Arizona
Tucson, AZ 85721
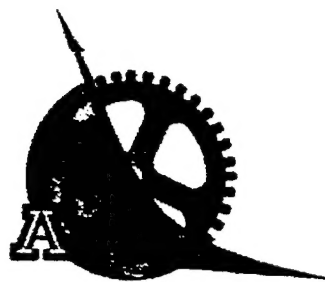
Submitted to

Dr. John Schmisseur, Program Manager

February 22, 2005

20050309 090

ABSTRACT

The lack of understanding of the physics of the transition in supersonic boundary layer flows is a major impediment in developing reliable transition prediction methods. This, in turn, represents a major obstacle in designing, developing, and operating high-speed flight vehicles such as the formerly proposed National Aerospace Plane (NASP), the future high-speed civil transport (HSCT), high-speed missiles, high-speed reconnaissance aircraft, and the Theater Missile Defense (TMD) interceptors. Transition to turbulence in high-speed flows is associated with significant increases in aerothermal loads on the flight vehicle, requiring additional thermal protection. Supersonic transition research suffers from the fact that reliable experiments are difficult and very expensive. Therefore, practically nothing is known about the later, nonlinear stages of transition and, in particular, about the final breakdown process. However, if and how the final breakdown occurs has to be understood in order to identify which disturbance scenarios lead to breakdown and which do not. This knowledge is essential for developing reliable transition prediction methods and it is critical for transition control, that is, to delay transition and thus reduce the aerothermal loads. To this end, Direct Numerical Simulations (DNS) of supersonic flow over a flat-plate with and without adverse pressure-gradient at Mach 3 were carried out in close collaboration with the experimental effort at Princeton University by G. Brown and co-workers. To confirm that simulations and experiments were based on the same "baseflow," the experimental baseflow profiles were compared with our Navier–Stokes results. The downstream development and the spatial growth rates of the disturbances obtained from the Navier–Stokes computations and from experimental measurements were compared as well. Overall, a remarkably good agreement was achieved. Towards the understanding of the nonlinear mechanisms, we investigated numerous nonlinear resonance and breakdown scenarios. Our simulations have shown that due to the stabilizing effects of compressibility for supersonic boundary layers, the transition process can be stretched significantly in the downstream direction and sometimes the transition process may even be aborted so that a turbulent boundary layer is never fully established. The extent of the transition process and the intensity of the temperature fluctuations, and the resulting heat load, depend strongly on the nonlinear mechanisms.

TABLE OF CONTENTS

TABLE OF CONTENTS — *Continued*

TABLE OF CONTENTS — *Continued*

1. INTRODUCTION

Transition in boundary layers at supersonic and hypersonic speeds is a major unresolved topic in Fluid Dynamics. Although significant progress has been made in recent years, crucial aspects of the transition physics are still in the dark. In fact, the lack of a basic understanding of high-speed transition, and as a consequence a lack of reliable transition prediction methods, was one of the key factors in the Defense Science Board's (1992) decision not to recommend the construction of a demonstrator vehicle for the National Aerospace Plane. For the future High-Speed Civil Transport (HSCT) (Parikh & Nagel, 1990), as well as for numerous defense-related applications such as high-speed missiles (Hingst, 1990; Korejwo & Holden, 1992), high-speed reconnaissance aircraft (Scott, 1996), and the Theater Missile Defense (TMD) interceptors (Johnson et al., 1997), considerable progress toward the understanding of high-speed boundary layer transition is required in order to develop reliable transition prediction methods that can be used for the design and safe operation of such advanced flight vehicles. The crucial need for reliable transition prediction methods for high-speed applications is due to the fact that transition to turbulence in supersonic/hypersonic boundary layers is associated with considerable increases in heat transfer. The increased heat loads (caused by transition) on the structure of the flight vehicles represent the main difficulties in designing and operating high-speed vehicles. Appropriate measures to guard against the heat transfer due to aerothermal loads are expensive and/or result in significant weight penalties. Good estimates of the transition location are of vital importance because only then can the aerothermal loads and surface temperatures be adequately predicted. In addition to surface heating, transition to turbulence also has a significant effect on the aerodynamic performance of high-speed flight vehicles as the skin friction for turbulent boundary layers is considerably higher than for the laminar boundary layer.

The understanding of transition for low-speed (incompressible) boundary layers is considerably ahead of that for high-speed (compressible) boundary layers, although many crucial aspects are also still not understood even for the low-speed case. There are several important reasons for the considerable gap in understanding of high-speed transition relative to low-speed transition. Of course, historically, high-speed flight, in particular hypersonic flight, has not been considered until recently and therefore the need to understand and predict transition did not exist earlier. However, there are two other main reasons why it is more difficult to obtain knowledge for high-speed boundary layer transition than for the low-speed case: i) Quality experiments for high-speed transition are considerably more difficult to carry out than for

incompressible transition and require high-speed testing facilities that are expensive to construct and expensive to operate. ii) The physics of high-speed boundary layer transition are much more complex than for low speeds. From linear stability theory (Mack, 1969), it is known that multiple instability modes exist for high-speed boundary layer flows, in contrast to only one mode (Tollmien-Schlichting, TS) for the incompressible case. The so-called first mode in supersonic boundary layers is equivalent to the TS mode in incompressible boundary layers. However, in contrast to incompressible boundary layers, where, according to the Squire's theorem, two-dimensional waves are more amplified than three-dimensional waves, for supersonic boundary layers three-dimensional (oblique) waves are more amplified than two-dimensional ones. Thus, experiments and theory always have to deal with the more complicated problem of three-dimensional wave propagation. In addition to the first mode, which is viscous, higher modes exist for supersonic boundary layers that result from an inviscid instability mechanism. According to linear stability theory (LST), the most unstable higher modes are two-dimensional and not oblique, as is the first mode. Also from linear stability theory, it is known that the first mode is dominant (higher amplification rates) for low supersonic Mach numbers while for Mach numbers above 4 the second mode is dominant (most amplified). In addition, for typical supersonic/hypersonic flight vehicle configurations, the three-dimensional nature of the boundary layers that occur, for example, on swept wings and/or lifting bodies, can give rise to so-called cross-flow instabilities and, as a consequence, cross-flow vortices that can be stationary or traveling.

Due to the difficulties in carrying out experiments (and "controlled" experiments, in particular) and due to the existence of multiple instability modes, the role and importance of the various instability modes in a realistic transition process are not understood at all. Of course, when amplitudes of the various instability modes reach high enough levels, nonlinear interactions of these modes can occur. As a consequence, the transition process in high-speed boundary layers is highly non-unique (and our simulations support this conjecture, see § 6), which means that slight changes in the environment or vehicle geometry may significantly alter the transition process.

An additional difficulty arises from the fact that for high-speed boundary layers the transition processes in free flight may be very different from those in the laboratory. As shown by Eissler & Bestek (1996), the difference between conditions for free flight ("hot," atmospheric conditions) and the laboratory ("cold," laboratory conditions) has a considerable effect on the stability behavior and, as a consequence, on the transition processes. This is best summarized by a quote from Stetson (1990), a pioneer in experimental high-speed transition research: "...one should not expect a transition Reynolds

number obtained in any wind tunnel, conventional or quiet, to be directly relatable to flight." This fact clearly defines the usefulness and critical importance of numerical simulations. The numerical simulation codes can be tested and validated by detailed comparison with laboratory experiments. Thereafter, they can then be applied with confidence to predict the effects of free-flight conditions on the transition processes and the resulting aerodynamic and aero- thermodynamic behaviors. Thus, only simulations can provide the crucial understanding and information for design and safe operation of high-speed vehicles.

2. RELATED PREVIOUS RESEARCH

2.1 Theoretical Investigations

There are a large number of scientific publications available on transition research, with the largest number of them dealing with low-speed transition. Recent investigations of transition, both high- and low-speed, were presented at the IUTAM Symposium on Laminar Turbulent Transition (Fasel & Saric, 2000). Some of the most important aspects of high-speed transition that are relevant to the proposed research are discussed below. The main body of the present knowledge concerning high-speed transition is still what was obtained using Linear Stability Theory (LST) by Mack (1969, 1975, 1984, 2000). Based on the findings by Mack, the linear stability behavior of compressible (supersonic) boundary layers differs from the incompressible case in several significant aspects:

i. More than one instability mode exists for $Ma > 2.2$: the first mode and the second and higher (multiple) modes.

ii. The first-mode disturbances are viscous (vortical) and are similar to the Tollmien-Schlichting (TS) modes of incompressible boundary layers. First-mode disturbances dominate (largest amplification rates) at low supersonic Mach numbers. However, in contrast to the incompressible case, the most amplified first-mode disturbances are three-dimensional (oblique) and not two-dimensional.

iii. The second and higher modes are inviscid (acoustic) and dominate at Mach numbers higher than about 4. The most unstable modes here are always two-dimensional (in contrast to the first mode).

iv. In addition to the inviscid (acoustic) higher modes, Mack identified additional viscous modes ('viscous multiple solutions') which, to date, have not been identified in experiments. However, they were also found in the Direct Numerical Simulations (DNS) of Eissler & Bestek (1996).

v. First-mode disturbances can be attenuated (as for the incompressible case for air) by wall cooling, wall suction, and favorable pressure gradients (Malik, 1989).

vi. The second and higher inviscid modes can be stabilized by favorable pressure gradients and suction; however, they are destabilized by wall cooling.

For linear stability theory analysis, the effects of the growing boundary layer on the disturbance growth are typically neglected ("parallel theory"). However, non-parallel effects can be included by using the Parabolized Stability Equations (PSE) approach (Bertolotti, 1991; Bertolotti *et al.*, 1992; Herbert, 1994). Depending on various parameters (Mach number, Reynolds number, frequency, etc.), non-parallel effects can significantly influence the disturbance growth rates. LST and linear PSE are only applicable for the first (linear) stage of the transition process where disturbance amplitudes are small and nonlinear interactions are negligible. Nonlinear PSE, on the other hand, is applicable to the nonlinear stages of transition (Bertolotti *et al.*, 1992; Herbert, 1994), although the computational effort becomes overwhelming when the development becomes strongly nonlinear in the later stages of transition. Also, analogous to incompressible boundary layer transition, several attempts have been made to apply secondary instability theory to model the initial three-dimensional nonlinear development (see, Masad & Nayfeh, 1990; El-Hady, 1991, 1992; Ng & Erlebacher, 1992, for example). However, whether or not any of these secondary instability mechanisms are relevant for supersonic transition is an open question because it is very difficult to unequivocally identify them in experiments (see § 2.2).

2.2 Experimental Investigations

Transition experiments in high-speed flows are extremely difficult and very expensive. Therefore, relatively few successful experimental efforts have been discussed in the open literature. Most experiments have emphasized investigations of the linear regime and the early stages of the transition process. Some examples are the experiments by Laufer & Vrebalovich (1960); Kendall (1975); Stetson *et al.* (1983); Stetson (1988); Kosinov *et al.* (1990); Stetson & Kimmel (1992*a*); Schneider *et al.* (1996), and Corke (see Cavalieri, 1995). An overview of the experimental efforts up to 1992 is given by Stetson & Kimmel (1992*b*). The experiments essentially verified some of the important parts of the linear theory. However, quantitative differences often occur that may be explained by the fact that in the experiments the transition process was "natural," i.e., it was initiated by the environmental disturbances, and not by "controlled" disturbance input (analogous to a vibrating ribbon as in incompressible transition experiments). Also, quantitative differences between experimental measurements and LST may be caused by the effects of the growing boundary layer being neglected in the linear stability theory analysis ("parallel theory").

All experimental efforts suffered more or less from difficulties in controlling the disturbance environment (such as sound radiated from turbulent

boundary layers on the tunnel walls). Nevertheless, these "natural" transition experiments could identify first and second instability modes (Kendall, 1975; Stetson et al., 1983). However, for example for Mach 2, considerable discrepancies arose between boundary layers on a flat plate and boundary layers on axisymmetric cones when "blow down" facilities were used. For axisymmetric cones, high-frequency second modes were dominant, while only low-frequency first mode disturbances were observed for the flat plate (Stetson & Kimmel, 1992b). In contrast, in an experiment using a Ludwieg tube for a sharp-nosed cone at Mach 5, no dominant second-mode disturbances could be detected (Wendt, 1993).

With the more recent experiments for a flat plate and axisymmetric cones at Mach number 3.5 in the NASA-Langley "Quiet Tunnel," a number of discrepancies between LST and other experiments were resolved (Chen et al., 1989; Cavalieri, 1995). Indications of nonlinear developments in the transition process were observed by Stetson et al. (1983) for a cone at Mach 8. Most of the experimental efforts suffered from the deficiency that no "controlled" disturbances could be introduced to allow for detailed quantitative comparisons with linear theory and, in particular, to allow for systematic investigations of the nonlinear stages of transition. Because of the lack of experimental evidence concerning the process in the later stages of transition, it is totally unclear which instability modes and which nonlinear mechanisms are responsible for the final breakdown to turbulence in supersonic boundary layers. The controlled experiments for a Mach 2 boundary layer by Kosinov & Tumin (1996) using a harmonic point source for the disturbance excitation have indicated, however, that secondary instability mechanisms were present. In fact, Kosinov & Tumin speculated that it was a subharmonic resonance with "oblique" fundamental disturbances. More recently, Maslov and co-workers (see Shiplyuk et al., 2003) reported "controlled" experiments for a sharp-nosed cone at $Ma = 5.95$ using a glow- discharge actuator to generate harmonic point source disturbances. They investigated several nonlinear interactions and identified a "classical" subharmonic resonance (with the 2-D second mode as primary disturbance) as a possible breakdown mechanism involving possibly a 3-D first mode as the subharmonic. However, in order to confirm this conjecture, detailed spatial and temporal resolution of the measurements would be required which, of course, is difficult experimentally. Shiplyuk et al. (2003) state in their paper, that numerical calculations would be helpful to clarify the scenarios of nonlinear interactions that are identified in the present work.

2.3 Numerical Simulations

Due to the difficulties in experimental investigations of high-speed boundary
layer transition and due to the limitations of linear stability theory, so-called
Direct Numerical Simulations (DNS) represent a promising tool for high-
speed transition research. In DNS the complete Navier–Stokes equations are
solved directly by proper numerical methods without making restricting as-
sumptions with regard to the baseflow and the form and amplitude of the
disturbance waves. Therefore, DNS is particularly well suited for investiga-
tions of the nonlinear development that is characteristic of the later stages of
high-speed boundary layer transition. Two fundamentally different models
are used for DNS: First, the so-called "temporal model," which is based on the
assumption that the baseflow does not change in the downstream direction
(thus excluding nonparallel effects). Also, assuming spatial (downstream)
periodicity of the disturbances, the disturbance development (growth or de-
cay) is then in the time-direction. The temporal model is analogous to the
temporal approach in LST with the frequency being complex and the spatial
wave number real. Due to the underlying assumptions, the temporal model
can only provide qualitative results. On the other hand, since a relatively
short integration domain can be used in the downstream direction (typically
one or two wave lengths of the fundamental wave) temporal simulations are
relatively inexpensive.
In contrast, in the "spatial model" no assumptions are made with regard
to the baseflow (thus nonparallel effects are included). The disturbance de-
velopment (growth or decay) is in the downstream direction as in physical
laboratory or free-flight situations. Thus, the spatial model allows realistic
simulations of high-speed transition and direct comparison with wind-tunnel
or free-flight experiments. However, simulations based on the spatial model
are typically much more costly than for the temporal model because a much
larger downstream integration domain is required (many wave lengths of the
fundamental disturbance wave). This is particularly true for simulations of
high-speed boundary layer transition, where the growth rates of the distur-
bance waves are much smaller than for the incompressible case and where
the growth rates of certain modes decrease with increasing Mach number.
Thus, relatively large (in the downstream direction) integration domains are
required to allow small disturbances to grow to the large amplitudes that
characterize the nonlinear stages of the transition process and finally lead to
the breakdown to turbulence. As a consequence, spatial simulations of high-
speed transition are computationally very challenging. Detailed discussions
of the DNS methodology for investigations of boundary layer transition, in
particular, discussions of the temporal and spatial approach, are given by

Fasel & Konzelmann (1990) , Kleiser & Zang (1991), and Reed (1993).
Probably the first transition simulation for supersonic boundary layers, al-
though restricted to two- dimensional, yet spatially evolving, disturbances,
was by Bayliss *et al.* (1985), who employed an approach analogous to that by
Fasel (1976) for incompressible boundary layers. The first three-dimensional
yet temporal DNS for flat-plate high-speed boundary layer transition was
performed by Erlebacher & Hussaini (1990). Here, only the linear and early
nonlinear stages were explored. Other temporal simulations were performed
by Normand & Lesieur (1992), Pruett & Zang (1992), Dinavahi & Pruett
(1993), Adams & Kleiser (1993). From such temporal simulations, Normand
& Lesieur (1992) found that, for their case of a flat-plate boundary layer with
$Ma = 5$, transition occurred via a subharmonic secondary instability for the
second mode. This finding was consistent with results from simulations by
Adams & Kleiser (1993), Pruett & Zang (1992), and Dinavahi & Pruett
(1993) for a boundary layer at Mach 4.5 on a hollow cylinder (the axisym-
metric analog of a flat-plate boundary layer). However, the main weakness of
these "temporal" simulations is the fact that they do not take the boundary
layer growth into account. In fact, experiments by Stetson & Kimmel (1993)
and PSE calculations by Chang *et al.* (1991) indicated that subharmonic
resonance may not be the preferred route to transition in realistic, growing
boundary layers (which include nonparallel effects).
Realistic simulations of transition scenarios including the effects of the grow-
ing boundary layer require the use of the spatial simulation model. The
first three-dimensional spatial simulations of transition in supersonic bound-
ary layers were reported by Thumm (1991) for a Mach number of 1.6. In
fact, from these, and follow-up simulations (Fasel *et al.*, 1993), it was dis-
covered that a new "Oblique Breakdown" mechanism produces much larger
growth rates than either subharmonic or fundamental resonance and requires
much lower disturbance amplitudes. Therefore, the "Oblique Breakdown" is
a likely candidate for a viable path to transition for supersonic boundary lay-
ers. Using PSE calculations, Chang & Malik (1993) confirmed the validity of
this oblique breakdown for a flat-plate boundary layer at $Ma = 1.6$. Based
on our DNS code (see Fasel *et al.*, 1993), Bestek & Eissler (1996) performed
simulations for Mach 4.8 and investigated various nonlinear mechanisms in-
cluding the "oblique breakdown" mechanism. Bestek & Eissler also found,
for the first time, an additional "higher viscous" mode, which Mack (1969)
had predicted using LST analysis. Pruett & Chang (1993) carried out spa-
tial DNS for a flat-plate boundary layer at Mach 4.5 and provided a detailed
comparison with PSE results. Later, an improved version of the code (Pruett
et al., 1995) was applied to a simulation of transition on axisymmetric sharp
cones at Mach 8 (Mach 6 after the shock; Pruett & Chang, 1995). The

simulation was combined with PSE calculations such that the linear and moderately nonlinear stages were computed by PSE while the strongly non-linear and breakdown stages of transition were computed by spatial DNS. This approach was motivated by the experience that linear and moderately nonlinear wave propagations can be computed more efficiently with PSE while the strongly nonlinear and breakdown stages (requiring many spanwise Fourier modes) are computed more efficiently with DNS. In this simulation, a second-mode-breakdown resonance was also investigated. The so-called rope-like structures obtained from numerical flow visualizations of the simulation data for this breakdown process are similar to those observed in high-speed transitional boundary layers on cones (see Pruett & Chang, 1995). Using numerical simulations, the leading edge receptivity of high-speed boundary layers has been investigated extensively by Zhong and co-workers (see Zhong, 2001). More recently, the magnetic field effects on the second-mode insta-bilities for a weakly ionized boundary layer at $Ma = 4.5$ using numerical simulations were investigated by Cheng et $al.$ (2003).

Relatively few attempts have been made to employ Large-Eddy Simulation (LES) for transitional flows in supersonic boundary layers (see, for example, Normand & Lesieur, 1992; Zang et $al.$, 1992). These simulations reported in the literature have to be viewed as being of an exploratory nature with regard to the applicability of LES for boundary layer transition. Nevertheless, these attempts demonstrated that LES could be employed advantageously for supersonic transition simulations. The main issues in applying LES for supersonic transition simulations are the use of proper subgrid-scale (SGS) models that are physically consistent through the entire transition process. Of course, LES would be a highly valuable tool for investigating the late stages of transition. As mentioned previously, DNS for supersonic boundary layer transition is very expensive due to the large computational domains that are required in the downstream direction. In addition, for simulations that include the final stages of transition (the actual breakdown to turbulence), an extremely fine grid would be required which, as a consequence, would place high demands with regard to computer memory and computation times. LES on the other hand would require considerably less resolution and, as a consequence, the amount of computer memory and computation times would be reduced accordingly.

3.   COMPUTATIONAL METHOD

The time-dependent flow over a flat plate is investigated using the spatial
DNS model. This model allows for a direct comparison with experiments
where disturbances develop in the downstream direction. The complete
Navier–Stokes equations for compressible flow form the governing equations
and thus include all non-parallel and nonlinear effects. In this chapter, details
on the governing equations, boundary and initial conditions, buffer domains
and introduction of controlled disturbances are given followed by a brief sum-
mary of the numerical method. Details on the numerical method and code
performance can be found in Harris (1997) and von Terzi (2004).

3.1   Governing Equations

Conservation of mass (continuity equation), conservation of momentum, and
conservation of total energy form the set of governing equations. These
are applied to a three-dimensional Cartesian coordinate system. The non-
dimensional form of the governing equations is obtained by by using a length
scale (the length of the plate in the experiments L_∞^*) and free-stream values
of velocity, temperature, density, and specific heat (U_∞^*, T_∞^*, ρ_∞^* and $C_{p\infty}^*$,
respectively) for normalization of all variables. The non-dimensional length
of the flat plate becomes equal to one and the following non-dimensional
variables are obtained:

$$x_i = \frac{x_i^*}{L_\infty^*} \quad , \quad t = \frac{t^*}{t_\infty^*} = \frac{t^*}{L_\infty^*/U_\infty^*}$$

$$u_i = \frac{u_i^*}{U_\infty^*} \quad , \quad \rho = \frac{\rho^*}{\rho_\infty^*} \quad , \quad T = \frac{T^*}{T_\infty^*} \quad , \quad p = \frac{p^*}{\rho_\infty^* U_\infty^{*2}} \quad , \quad E_t = \frac{E_t^*}{\rho_\infty^* U_\infty^{*2}}$$

$$\mu = \frac{\mu^*}{\mu_\infty^*} = \frac{\mu^*}{\mu^*(T_\infty^*)} \quad , \quad k = \frac{k^*}{\mu_\infty^* C_{p\infty}^*} = \frac{\mu}{Pr} \,.$$

The Mach and Reynolds numbers are introduced as

$$Ma = \frac{U_\infty^*}{a_\infty^*} = \frac{U_\infty^*}{\sqrt{(\kappa-1)C_{p\infty}^* T_\infty^*}} \quad , \quad Re = \frac{\rho_\infty^* U_\infty^* L_\infty^*}{\mu_\infty^*}, \tag{3.1}$$

respectively. The non-dimensional continuity, momentum and energy equa-
tions are given by

$$\frac{\partial \rho}{\partial t} + \frac{\partial}{\partial x_j}\left(\rho u_j\right) = 0 \tag{3.2}$$

$$\frac{\partial \rho u_i}{\partial t} + \frac{\partial}{\partial x_j}\left(\rho u_i u_j + \delta_{ij}p - \tau_{ij}\right) = 0 \tag{3.3}$$

$$\frac{\partial E_t}{\partial t} + \frac{\partial}{\partial x_j}\left([E_t + p]u_j - u_i\tau_{ij} + q_j\right) = 0. \tag{3.4}$$

The total energy, viscous stress and heat flux terms are

$$E_t = \rho\left(\frac{T}{\kappa(\kappa-1)Ma^2} + \frac{u_k u_k}{2}\right), \tag{3.5}$$

$$\tau_{ij} = \frac{\mu}{Re}\left(\frac{\partial u_i}{\partial x_j} + \frac{\partial u_j}{\partial x_i} - \frac{2}{3}\delta_{ij}\frac{\partial u_k}{\partial x_k}\right) \tag{3.6}$$

and

$$q_i = -\frac{\mu}{(\kappa-1)Ma^2 RePr}\frac{\partial T}{\partial x_i}, \tag{3.7}$$

respectively. The viscosity is obtained using Sutherland's law and the equation of state becomes

$$p = \frac{\rho T}{\kappa Ma^2}. \tag{3.8}$$

3.2 Computational Domain
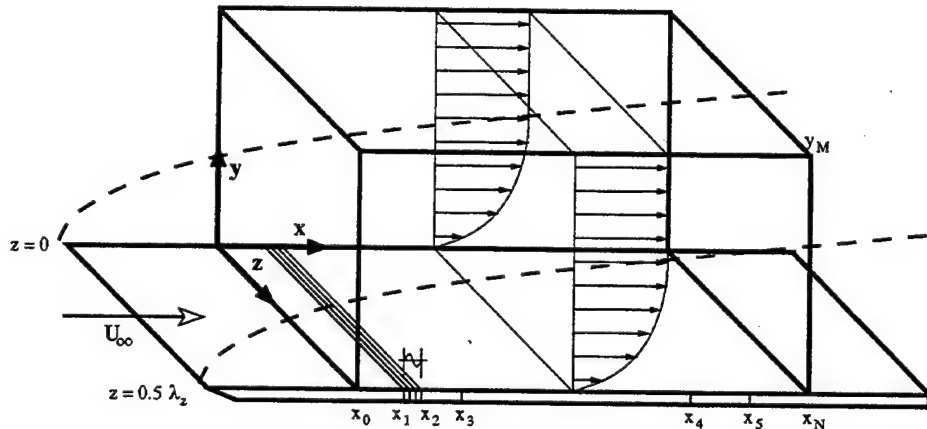
Figure 3.1 Computational domain and boundaries.

The equations are discretized and solved in the computational domain shown in figure 3.1. The dashed lines indicate the boundary layer that forms when a uniform flow with velocity U_∞ encounters the flat plate. An example for a computational domain is represented by a box which starts at x_0 and ends at x_N. The value for the domain height is y_M. Disturbances are introduced between the locations x_1 and x_2. All simulations performed in this work deal with 3D waves generated in pairs in the disturbance slot with Ψ and $-\Psi$ as

their wave angle. The wave angle determines their spanwise wave number since

$$\tan(\Psi) = \frac{\gamma}{\alpha_r} \,. \tag{3.9}$$

The wave with Ψ and the wave with $-\Psi$ as its wave angle have the same spanwise wave number γ. The domain width is chosen such that it matches half of one wavelength λ_z of the 3D waves. Locations x_3, x_4 and x_5 specify the start and end locations of the pressure gradient (if applied). They are explained in more detail in § 3.4.4.

3.3   Initial Conditions

All simulations are carried out in two parts. First, a "baseflow" is computed as the steady solution to the Navier–Stokes equations and, second, this base-flow is used as an initial condition for the stability investigations, where controlled disturbances are then introduced. For the (unsteady) forced flow simulations, the baseflow is also required as input for the inflow, outflow and free-stream boundary conditions (see § 3.4).

3.3.1   Using Compressible Blasius Similarity Solution

All simulations at supersonic speeds use the compressible boundary layer similarity solution as initial condition for obtaining the baseflow. The similarity solution is obtained from the Blasius boundary layer ordinary differential equation (ODE) where the prime denotes a derivative with respect to the independent (similarity) variable η.

$$(Cf'')' + ff'' = 0 \tag{3.10}$$

$$\left(\frac{C}{Pr}g'\right)' + fg' + C\left(f''\right)^2 = 0 \tag{3.11}$$

with

$$C = \frac{\rho^*\mu^*}{\rho_\infty^*\mu_\infty^*}$$
$$f = f(\eta)$$
$$g = g(\eta)$$

and

$$\eta = \frac{u_\infty^*}{\sqrt{2\rho_\infty^* u_\infty^* \mu_\infty^* x^*}} \int \rho^* dy^* \,. \tag{3.12}$$

Several simplifications in deriving this ODE were made so that the Navier–Stokes solution will differ from this initial condition. These perturbations will

travel downstream and, finally, will be convected out of the computational domain. The resulting flow field is the desired baseflow for the simulations without a pressure-gradient. However, for the simulations with an adverse pressure-gradient (APG) in the downstream direction, the above "baseflow" is taken as an initial guess. Then, a constant pressure gradient was introduced through the free-stream boundary condition and the baseflow with APG is computed (see figure 3.2).
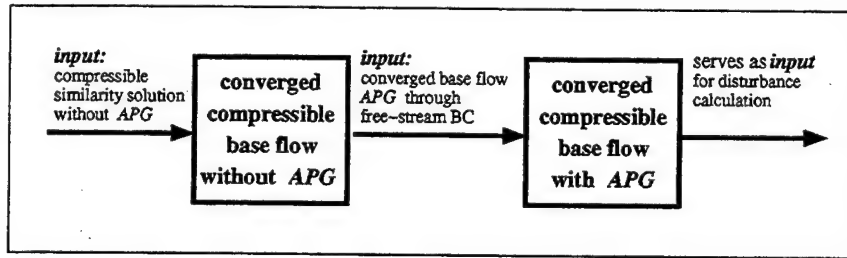

Figure 3.2 Generation of a compressible baseflow with APG.

3.3.2 Using Falkner–Skan Similarity Solution

For the incompressible validation simulation with an adverse pressure gradient in the streamwise direction, the solution to the third-order ODE of Falkner & Skan (1931) (c.f. Schlichting & Gersten, 2000) is used as the initial condition for obtaining the baseflow. These equations were derived by introducing the similarity variable

$$\eta = y\sqrt{\frac{(m+1)}{2}\frac{U_e(x^*)^*}{\mu^* x^*}} = y\sqrt{\frac{(m+1)}{2}\frac{U_e(x)Re}{x}}, \qquad (3.13)$$

as the independent variable and f as the dependent variable with

$$f' = \frac{u^*}{U_e^*(x^*)} = \frac{u}{U_e(x)} \qquad (3.14)$$

(again a prime denotes a derivative with respect to η). This transformation is only possible if the following assumption for the free-stream velocity $U_e(x)$ is made:

$$U_e(x) = U_0 x^m, \qquad (3.15)$$

with $U_0 = x_0^{-m}$ and $m = \beta_H/(2 - \beta_H)$ where β_H is the Hartree parameter. For $\beta_H = -0.1988$ the flow separates.

The x-momentum equation provides an expression for the pressure gradient

$$\frac{\partial p}{\partial x} = -U_e(x)\frac{\partial U_e(x)}{\partial x}.$$
(3.16)

Integrating this expression in x leads to the pressure distribution at the free-stream

$$p = \frac{1}{2}(1 - (\frac{x}{x_0})^{2m}) + \frac{1}{\kappa Ma^2}$$
(3.17)

with $1/(\kappa Ma^2)$ as the integration constant. Equation (3.17) is the final equation which is implemented into the compressible DNS code. The integration constant represents the value of the pressure at the free-stream at location $x = x_0$ and is obtained by equation (3.8) for $\rho = T = 1$. The Mach number appears in equation (3.17) since the DNS code used for the present research is compressible.

Finally, the third-order ODE derived by Falkner & Skan has the form

$$f''' + ff'' + \beta_H(1 - f'^2) = 0$$
(3.18)

with the boundary conditions

$$f(0) = 0; \qquad f'(0) = 0; \qquad f'(\infty) = 1.$$
(3.19)

It is solved numerically and the solution serves as an initial condition for the DNS code.

Since the DNS code solves the compressible Navier–Stokes equations and the initial condition is incompressible, a value for the temperature has to be computed. The total enthalpy h_t is assumed to be constant over y. This means that the enthalpy in the free-stream is equal to the enthalpy in the boundary layer

$$h_{te}^* = h_t^* = const.$$
(3.20)

The substitution of $h_t^* = c_p^* T^* + 1/2\,(u^{*2} + v^{*2})$ into equation (3.20) gives

$$\cdot c_p^* T^* + \frac{(u^{*2} + v^{*2})}{2} = c_p^* T_e^* + \frac{U_e^{*2}}{2}$$
(3.21)

which is put in non-dimensional form and solved for T

$$T = 1 + \frac{\kappa - 1}{1}Ma^2(U_e^2 - u^2 - v^2);$$
(3.22)

where v has the form

$$v = \sqrt{\frac{m+1}{2}\frac{U_e(x)}{x\,Re}}\left(\frac{1-m}{m+1}\eta f' - f\right).$$
(3.23)

Table 3.1 summarizes the equations that are used in the DNS code to generate an appropriate initial condition for the incompressible validation case with adverse pressure gradient.

quantity	equation
u_{IC}	$f'U_e$
v_{IC}	$\sqrt{\frac{m+1}{2}\frac{U_e(x)}{xRe}}\left(\frac{1-m}{m+1}\,\eta\, f' - f\right)$
p_{IC}	$\frac{1}{2}(1 - (\frac{x}{x_0})^{2m}) + 1/(\kappa Ma^2)$
T_{IC}	$1 + \frac{\kappa-1}{1}Ma^2(U_e^2 - u_{IC}^2 - v_{IC}^2)$
ρ_{IC}	$\kappa\, Ma^2 p_{IC}/T_{IC}$

Table 3.1 Equations used for initial condition of incompressible validation case with APG.

3.4   Boundary conditions

The computational domain and its boundaries are shown in figure 3.3. In the lateral direction z, periodicity is assumed. More details about the lateral boundary can be found in von Terzi (2004). The baseflow and the forced flow simulations are computed with the same boundary conditions with the exception of the free-stream, where for the baseflow the pressure is fixed and for the unsteady simulations a decay condition is employed for all disturbance quantities.
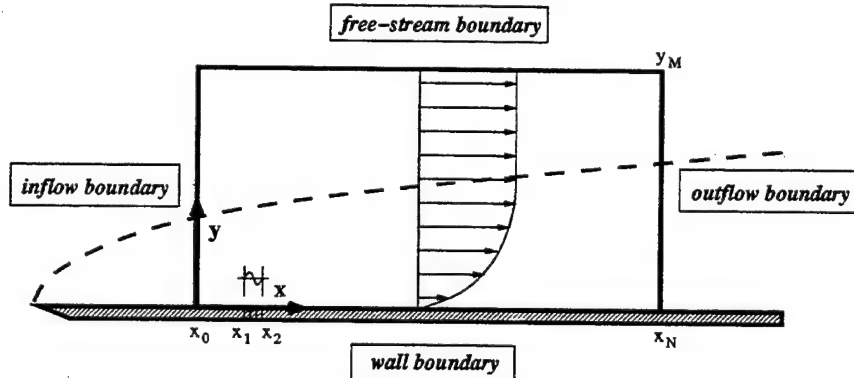

Figure 3.3 Boundaries of the computational domain.

3.4.1   Inflow

Incompressible Flow

At the inflow, all quantities except for the pressure are fixed with the value of the initial condition

$$\phi = \phi_{IC}.\tag{3.24}$$

For the pressure, a gradient condition is employed. Because of the pressure gradient in streamwise direction, its derivative is not equal to zero. The change of the pressure in y is neglected so that its derivative in x has the same value as at the free-stream over the entire inflow

$$\frac{\partial p}{\partial x} = -U_0^2 m x^{2m-1} \text{ and } \frac{\partial p}{\partial x} = 0, \tag{3.25}$$

for flow with and without APG, respectively. Since T and ρ are fixed the equation of state is violated. Nevertheless, upstream-traveling sound waves can pass through the boundary.

Compressible Flow

For a compressible flow all quantities are fixed to the value of the initial condition

$$\phi = \phi_{IC}, \tag{3.26}$$

except for the subsonic region of the boundary layer where the pressure derivative is set to zero

$$\frac{\partial p}{\partial x} = 0. \tag{3.27}$$

This is not valid for a streamwise pressure gradient but the subsonic region is very small and the ill-posed problem did not produce any difficulties.

3.4.2 Outflow

Incompressible Flow

The outflow is treated by applying

$$\frac{\partial^2 \phi}{\partial x^2} = 0, \tag{3.28}$$

where ϕ symbolizes the conservative variables ρ, ρu_i and E. Since the pressure is not held constant at the inflow, a Dirichlet condition must be employed to the outflow

$$p = p_{IC}, \tag{3.29}$$

otherwise the pressure field drifts from its specified value. For the incompressible validation case, the fixed pressure was responsible for strong reflections of pressure waves. The reflections caused upstream-traveling waves in all other quantities that were reflected at the inflow. A remedy for this problem was found by ramping down the disturbances before they reach the inflow or outflow boundary (see § 3.5).

Compressible Flow

For all conservative variables as well as for the pressure, the condition

$$\frac{\partial^2 \phi}{\partial x^2} = 0 \tag{3.30}$$

is applied. Reflections of disturbances were very weak, however this condition fails where $u < 0$ or $u \approx 0$. For that reason, a buffer domain (see § 3.5), which ramps the disturbances to zero, had to be used, in particular for the oblique breakdown investigations.

3.4.3 Wall

The incompressible and compressible calculations are performed with the same wall boundary conditions. The previously described computational boundary conditions are artificial and usually do not represent the physical solution at the enforced location. An exception for that is the wall. The no-slip and no-penetration conditions are used, thus

$$u = v = w = 0. \tag{3.31}$$

Note that v is non-zero at the disturbance slot. The wall is assumed to be adiabatic, i.e.,

$$\frac{\partial T}{\partial y} = 0, \tag{3.32}$$

and the pressure is calculated from the y-momentum equation

$$\frac{\partial p}{\partial y} = -\frac{\partial}{\partial y}(\rho v^2) + \frac{\partial}{\partial x}(\tau_{xy}) + \frac{\partial}{\partial y}(\tau_{yy}) + \frac{\partial}{\partial z}(\tau_{yz}). \tag{3.33}$$

Note that the time derivative is zero for the steady baseflow and neglected at the forcing slot for the simulations with forcing.

3.4.4 Free-Stream

One focus of this report is the investigation of the influence of an APG on transition for a compressible boundary layer. For this purpose, an APG has to be introduced. The simplest way of achieving this goal is to provide an appropriate free-stream boundary condition. In experiments a pressure gradient can be created at the free-stream through geometrical changes. For supersonic flows, a decreasing of the cross-sectional area of the flow passage and, for subsonic flows, an increasing of the cross-sectional area of the flow passage generate an APG.

Incompressible Flow

For the baseflow calculation, as an initial condition, a Falkner-Skan similarity solution is employed (see § 3.3.2) which already has the correct pressure distribution at the free-stream. Therefore p only needs to be fixed to the initial value

$$p = p_{IC} \, . \tag{3.34}$$

For u and ρ, von Neumann conditions are used, hence

$$\frac{\partial u}{\partial y} = 0 \tag{3.35}$$

and

$$\frac{\partial \rho}{\partial y} = 0 \, . \tag{3.36}$$

This is a good approximation because the density should be constant (incompressible flow) and u should not change in y outside of the boundary layer. From the continuity equation the derivative of the v-velocity can be obtained,

$$\frac{\partial v}{\partial y} = -\frac{\partial u}{\partial x} = -\frac{\partial U_e(x)}{\partial x} \, . \tag{3.37}$$

Using

$$U_e(x) = U_0 \, x^m \tag{3.38}$$

equation (3.37) yields

$$\frac{\partial v}{\partial y} = -U_0 \, m \, x^{m-1} \, . \tag{3.39}$$

For the unsteady simulations, an important issue is the imposition of the pressure gradient. A boundary condition at the free-stream should not modify the specified pressure distribution of the baseflow and, at the same time, allow disturbances to pass the domain boundary. Kloker (1993), in his code, divided the flow quantities into a disturbance flow and a baseflow. For the disturbance quantities he applied a decay condition. The u-velocity of the baseflow was set to the similarity value of equation (3.15) and the pressure derivative in x to equation (3.16). This has the advantage that the base pressure distribution is fixed and disturbances can travel out of the domain. Similar conditions are applied in this work. All quantities are divided into a baseflow and disturbance flow at the free-stream

$$\phi = \phi_{IC} + \phi' \, . \tag{3.40}$$

For the disturbances, the decay condition is applied and the base part is kept constant. A detailed derivation of the decay condition can be found

in Thumm (1991). Here, only the final equation is presented. For the most general case, a compressible flow, the decay condition has the form

$$\frac{\partial \phi'}{\partial y} = -\sqrt{\alpha^2(1 - Ma_\infty^2(1-c)^2) + \gamma^2}\ \phi'. \tag{3.41}$$

In the limit

$$\lim_{Ma_\infty \to 0} \frac{\partial \phi'}{\partial y}, \tag{3.42}$$

equation (3.41) reduces to the incompressible version (c.f. Kloker, 1993)

$$\frac{\partial \phi'}{\partial y} = -\sqrt{\alpha^2 + \gamma^2}\ \phi'. \tag{3.43}$$
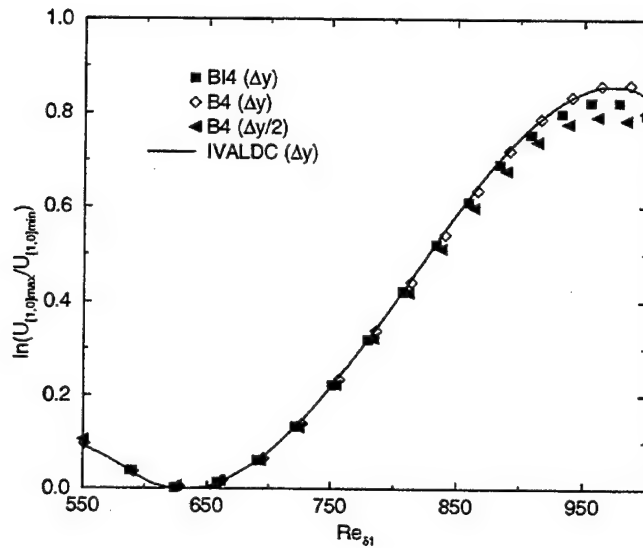

Figure 3.4 Validation of the decay-condition. Amplitude distribution of a TS–wave versus $Re_{\delta 1}$. $BI4$ and $B4$: calculations by von Terzi (2004) with decay condition on total flow variables; $IVALDC$: decay condition only on disturbance variables.

Figure 3.4 shows a test calculation (see appendix C for the computational parameters) where the previously described decay condition is employed. As a test case, the primary instability behavior of an incompressible flow over a flat plate is simulated. The amplitude of the 2D disturbances, that are introduced into the computational domain, is small, so that a TS wave in the linear stage is excited. The graph illustrates the logarithm of the downstream amplitude distribution of the u-velocity normalized with its minimum. Simulations by von Terzi (2004) are utilized as comparison. Case $BI4$ agrees

very well with Fasel & Konzelmann (1990) and is taken as the result which reproduces the correct amplitude distribution. It was obtained from an incompressible code. For higher Reynolds numbers (based on the displacement thickness), the coarse and fine version of $B4$ vary from $BI4$. Both versions of $B4$ are conducted with the compressible code which is also used for the present research, but with a different implementation of the decay condition which did not fix the pressure gradient at the free-stream boundary. $IVALDC$, the case with the new decay condition does not deteriorate the solution of the case without APG.

Compressible Flow

Figure 3.2 illustrates the steps which have to be taken to start a forced flow simulation with APG. First, a baseflow without any pressure gradient is generated. Then, at the free-stream, a specified pressure distribution is introduced and the solution converged out. Finally, this baseflow serves as initial condition for the unsteady simulation. These three steps need different free-stream boundary conditions which are explained in the following paragraphs.

For the baseflow calculation without APG, a characteristic boundary condition derived by Harris (1997) is used

$$\frac{\partial \phi}{\partial \vec{c}} = 0 . \tag{3.44}$$

All variables do not change along the direction of the characteristics that is denoted by $\vec{c}$ and given by the Mach angle.
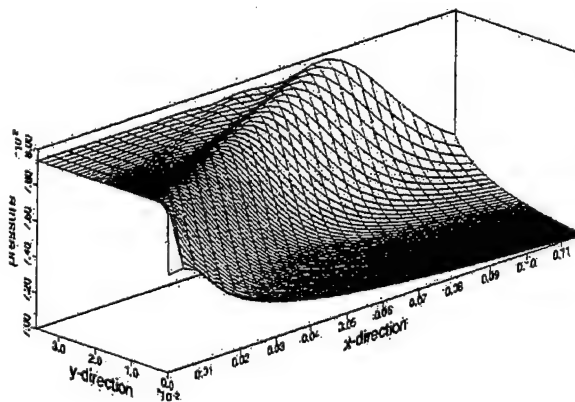

Figure 3.5 Adjustment between similarity solution and DNS solution. The pressure distribution of the first 30 points is plotted.

At the inflow, the adjustment between the similarity solution and the DNS

solution causes an effect similar to an expansion fan which leaves the domain along characteristics (figure 3.5). If the pressure is fixed to prescribe a desired pressure distribution at the free-stream, which is explained later, the expansion fan is reflected and makes it impossible to create a clean baseflow with APG. Therefore, the grid points where the pressure is strongly influenced by the expansion fan are cut off the computational domain and a smaller domain is used for the generation of the baseflow with APG.
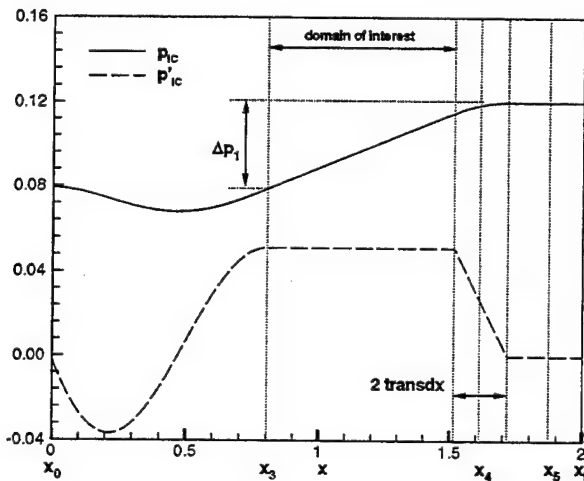

Figure 3.6 Pressure distribution at the free-stream (p_{IC}) and its derivative $(\partial p_{IC}/\partial x)$. x_3 is the location where the linear distribution with positive slope starts and $x_4 - transdx$ is its end. $x_4 + transdx$ can serve as a start location for a linear distribution with negative slope which ends at x_5. Here no distribution with negative slope is used. $transdx$ is a parameter which can be specified in the DNS code and which defines the interval where a quadratic Bézier–curve is employed.

In order to obtain a baseflow with APG, the pressure has to be fixed at the free-stream. Figure 3.6 shows one example. In all calculations, a constant gradient was employed. It is not possible to prescribe this pressure distribution throughout the domain from the inflow to the outflow, because at the corner between inflow and free-stream a shock would be generated which would travel along a characteristic to the wall. Therefore a blending function has to be used which smoothly connects the original pressure distribution (from the calculation with zero pressure gradient) with the new APG distribution. For this purpose a $\sin^2$-function is employed that starts at x_0 and ends at x_3. The solid line represents the pressure along the x-direction

at the upper boundary and the dashed line its first derivative. From x_3 on, the pressure is increased until $x_4 - transdx$ and its distribution has the slope $\Delta p_1/(x_4-x_3)$. $transdx$ is a parameter of the DNS code which specifies half of the interval which is used to connect the pressure distribution upstream of x_4 with the distribution downstream of x_4. As a blending function, a quadratic Bézier–curve is prescribed. A Bézier–curve is defined by a set of control points which determines its shape. It is a polynomial and was invented by the French engineer Pierre Bézier in the 60ies. The domain downstream of $x_4 - transdx$ represents a buffer domain that can be used to accelerate the flow by decreasing the pressure linearly with the slope $-\Delta p_2/(x_5 - x_4)$ from location $x_4 + transdx$ to x_5. The domain for the forced flow calculation is indicated as "domain of interest." After the baseflow with the APG is converged out, the unusable parts of the domain are cut off (for example upstream of x_3 and downstream of $x_4 - transdx$). The derivative of the pressure shows no jumps at the locations where the blending functions connect different pressure distributions and this is necessary for the x-momentum equation of the governing equations (3.3) since there the derivative is calculated. The other flow variables are treated by applying equation (3.44).

The unsteady simulations for the compressible flow are carried out with the same free-stream boundary condition as for the incompressible flow. All variables are treated by employing equation (3.41).

3.5   Buffer Domains at Inflow and Outflow

The buffer domain technique, especially ramping down disturbances before they reach the outflow or even the inflow, is very effective to avoid reflections of disturbance waves at the boundaries. Kloker (1993), Eissler (1995) and Meitz (1996) used the ramping method in their investigations. Here, this technique is applied mainly for the outflow. For the incompressible validation, a ramping function is also used for the inflow. In the buffer domain all quantities, $\rho, \rho u_i$ and E_t are multiplied by a function which ramps the disturbance values to zero, such that the total quantities reach their base (initial) values:

$$f_r(x) = f_{IC}(x) + c(\xi)(f(x) - f_{IC}(x)). \qquad (3.45)$$

In equation (3.45), $f(x)$ symbolizes the total flow quantities and f_{IC} their base values. The difference of $f(x) - f_{IC}(x)$, which is the disturbance value, is multiplied by a weighting function $c(\xi)$. $f_r(x)$ is the final value in the buffer region. Meitz (1996) applied a weighting function of the form

$$c(\xi) = e^{-\frac{\xi^4}{10}}(1 - \xi^{50})^4, \qquad (3.46)$$

where ξ is defined as

$$\xi = \frac{x_{end}^{in} - x}{x_{end}^{in} - x_{start}^{in}}\,, \tag{3.47}$$

for the inflow, and

$$\xi = \frac{x - x_{start}^{out}}{x_{end}^{out} - x_{start}^{out}}\,, \tag{3.48}$$

for the outflow. x_{start} and x_{end} are the start and end location of the buffer domain.

During the simulation, the weighting function is applied at every Runge–Kutta timestep so that

$$f_{\tau}^{newstep}(x) = c(\xi) f_{\tau}^{oldstep}(x). \tag{3.49}$$

If this operation is performed n times, then a wave that travels through the buffer domain with the flow "experiences" the multiplication with $c(\xi)$ n times. This leads to an "effective ramping function" of $c(\xi)^n$. The time a wave requires to travel through the buffer domain is determined by its phase speed and the length of the buffer domain. From this time, n can be calculated. If n becomes large, repeated multiplications of $c(\xi)$ with itself cause an increasing slope of the effective ramping function. This is definitely not desirable because a too steep effective ramping function can again lead to reflections of disturbances. For all calculations, n was small enough, such that the ramping function defined in equation (3.46) could be applied on buffer domains with the length of one or two streamwise wavelengths λ_x.

3.6 Disturbance Generation

Harmonic disturbances are introduced to the boundary layer by periodic blowing and suction through a slot in the plate. The slot is located about one Tollmien–Schlichting wavelength downstream of the inflow (see figure 3.1). All other boundary conditions are not affected. Note that the pressure boundary condition of equation (3.33) is only approximately valid for a non-zero wall-normal velocity, however, it is a reasonable approximation as long as $A\beta/Re = AF \ll 1$, where β is the forcing frequency and A the forcing amplitude. The disturbance velocity v is given as

$$v(x,t) = A\,v_p(x)\,\sin(\beta t)\,. \tag{3.50}$$

For this study, the amplitude is ramped up from zero over the first forcing period, i.e., for $0 \leq t \leq T = 2\pi/\beta$. In addition, a zero net mass flux enters the computational domain due to the prescribed spatial disturbance profile $v_p(x)$ (see figure 3.7, with the circles indicating the values for a 16-points

resolution on a slot of width $\lambda_x/2$). In order to balance considerations with respect to receptivity and resolution requirements, the slot should be between $\lambda_x/4$ and λ_x long with a minimum of eight points in the x-direction. The slot itself should be far enough away from the inflow (see appendix B.1.4).
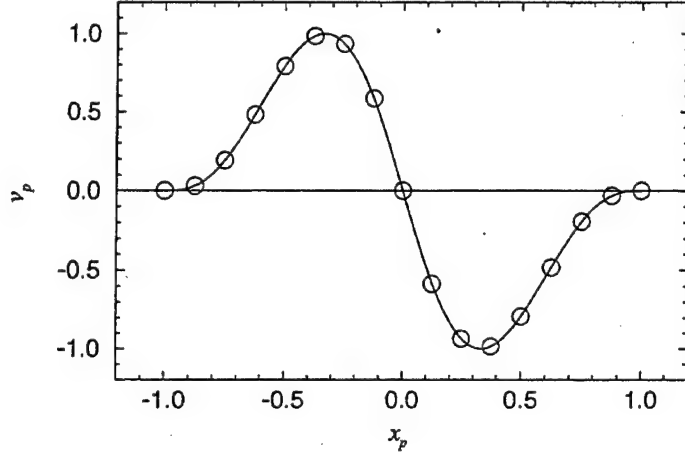

Figure 3.7 Disturbance profile $v_p(x)$ (reproduced from Harris, 1997).

3.7   Numerical Method for Solving the Governing Equations

A spatial DNS model is used with a fourth-order Runge–Kutta method for time-advancement and "fourth-order" split finite differences in the x- and y-directions. In the z-direction, a periodic solution is assumed and, consequently, a Fourier transformation is applied. Note that, for three-dimensional calculations, the nonlinear terms of the governing equations are computed in physical space and are then transformed back to spectral space for differentiation and integration. Variables are symmetric over one-half of the spanwise wavelength (except for w, which is antisymmetric over this distance). Thus only half a wavelength in the z-direction needs to be computed. In order to avoid aliasing errors, the number of physical planes is chosen to be greater to 3/2 spectral planes. The numerical method is explained in detail in Harris (1997) and von Terzi (2004).

4.   VALIDATION CASES

The original code, written by Harris (1997) for investigations of compressible, plane wakes, has already been extensively validated (c.f. von Terzi, 2004). Here, several additional validation cases demonstrate that the code is able to perform stability investigations of supersonic flow over a flat-plate with and without adverse pressure-gradient (APG). Nonetheless, physical and computational parameters must be chosen carefully to accurately capture the physics of the flow and to ensure the stability of the numerical method. First two cases from the literature are recomputed. The references (Eissler, 1995; Thumm, 1991) performed supersonic stability investigations–one at a Mach number lower and the other at a higher one than for the present study. The validation of the code with pressure gradient is divided into three sections. First, the code is validated for an incompressible flow. For comparison, case A of Kloker (1993) is recomputed. In the following section the LST solver of Mack is described, especially the steps that were required to get a solution for a flow with pressure gradient. Finally, two DNS calculations (one without and one with APG) are compared with the corresponding solutions of the linear stability solver of Mack.
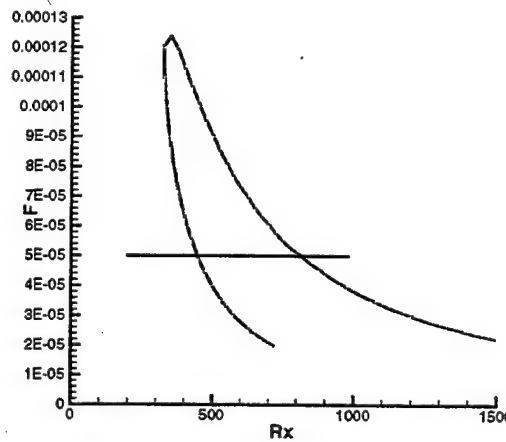

Figure 4.1 Linear stability diagram for $Ma = 1.6$; the solid horizontal line denotes case A1 of Thumm (1991).

4.1 Supersonic Flow at Mach 1.6

Case A1 of Thumm (1991) allows for validating the growth of a three-dimensional TS–wave with results from DNS and linear stability theory. The integration domain ranges from $R_x = 200$ to $R_x = 980$ with a forcing frequency of $\beta = 5.0025$. This case is marked in the corresponding stability diagram (see figure 4.1). The computational parameters are summarized in appendix C, table C.1. As can be seen in figure 4.2 the amplitude and phase distributions agree with the results of Thumm (1991). The amplification rate
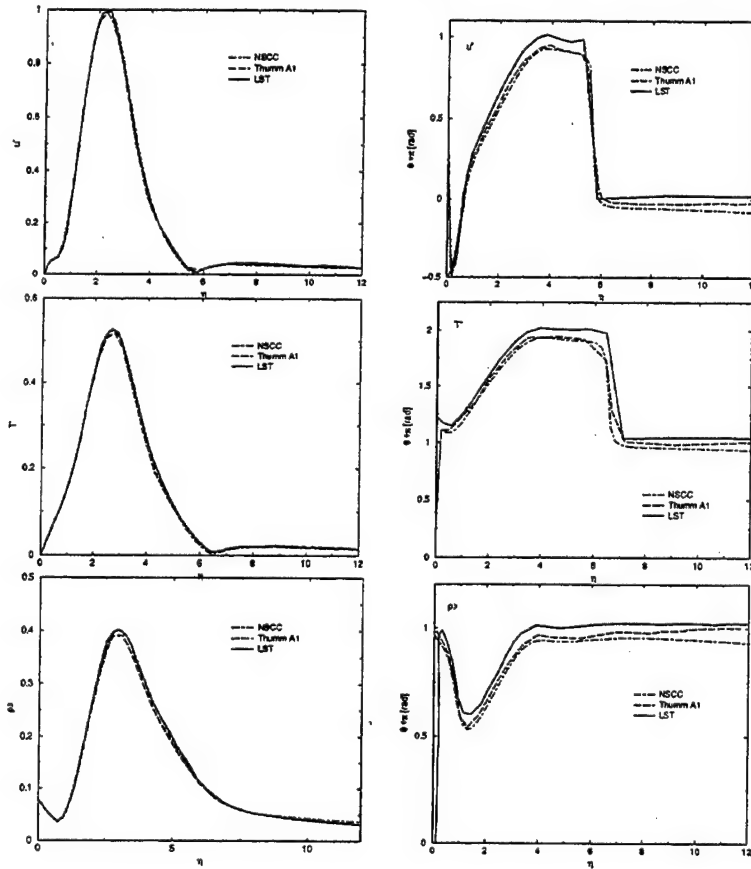

Figure 4.2 Distributions of amplitude (left) and phase (right) for u', T' and ρ' (from top to bottom) at $R_x = 680$, for case A1 of Thumm (1991).

$-\alpha_i$ is plotted in figure 4.3. It matches the calculation of Thumm (1991) and LST fairly well demonstrating that the DNS–code is capable of simulating the growth of instability waves in a supersonic boundary layer.
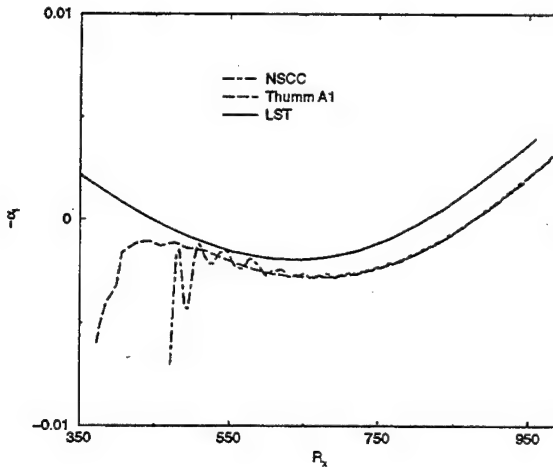
Figure 4.3 Comparison of amplification rates for case A1 of Thumm (1991).

4.2   Supersonic Flow at Mach 4.8

Case C of Eissler (1995) simulates a flow under atmospheric conditions with constant wall-temperature. The computational parameters are summarized in appendix C, table C.1. To keep the wall-temperature constant, the wall has to be "cooled," thus stabilizing the first mode and, at the same time, destabilizing the higher modes (Mack, 1969). Indeed, the second mode for the chosen frequency of $F = 10 \times 10^{-5}$ is the most unstable as can be seen in the stability diagram of figure 4.4.
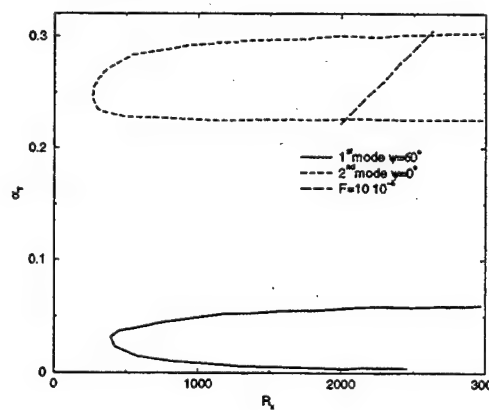

Figure 4.4 Linear stability diagram for $Ma = 4.8$, the dashed straight line denotes case C of Eissler (1995).
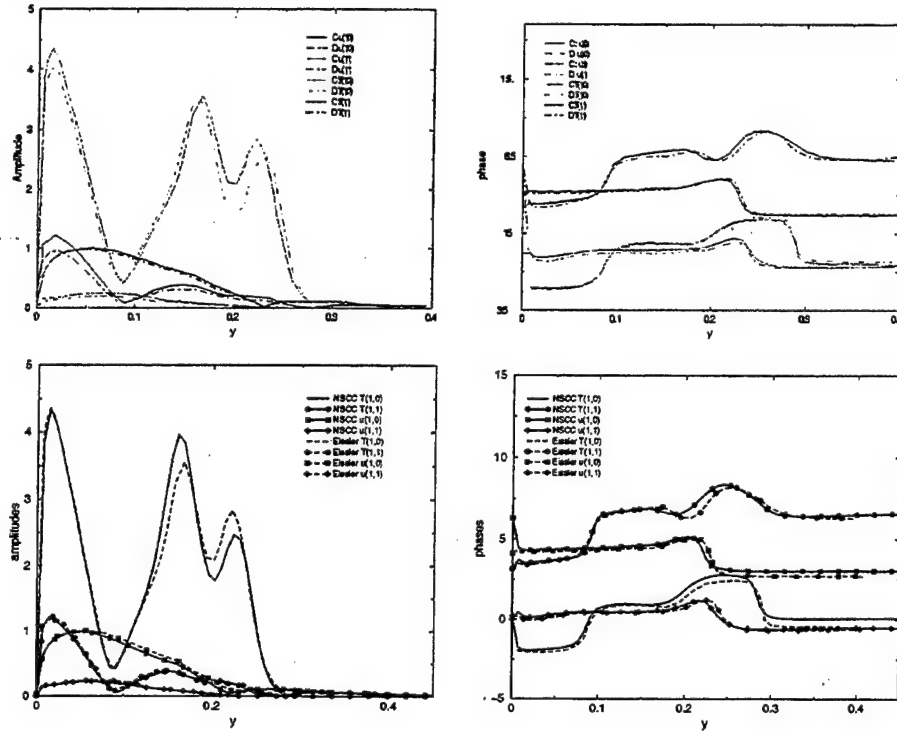
Figure 4.5 Distributions of amplitude (left) and phase (right) for u' and T'; data from Eissler (1995,top) and current investigation (bottom).

Eissler (1995) chose this case to show that computations with a thermally perfect gas are not worth the additional computational cost in comparison to computing with a calorically perfect gas. The velocity field is practically identical while the temperature distribution of the computation with a thermally perfect gas ranges slightly above the one with the calorically perfect gas (see figure 4.5). Since thermodynamic aspects are not under investigation, the higher computational cost calculating with a thermally perfect gas is not justified. For this reason, all further computations are carried out with a calorically perfect gas.

Note that, with respect to stability considerations, this validation case is calculated such that all disturbances in the streamwise and the spanwise direction have the same frequency (fundamental resonance). The amplitude and phase distribution of the velocity and temperature disturbances for the 2D and first 3D mode shown in figure 4.5 agree well. The slightly higher temperature amplitude in the baseflow disturbance, $T(1,0)$, is likely due to convergence problems of Eissler (1995).

The fact that the amplitudes employed by Eissler (1995) and the location of
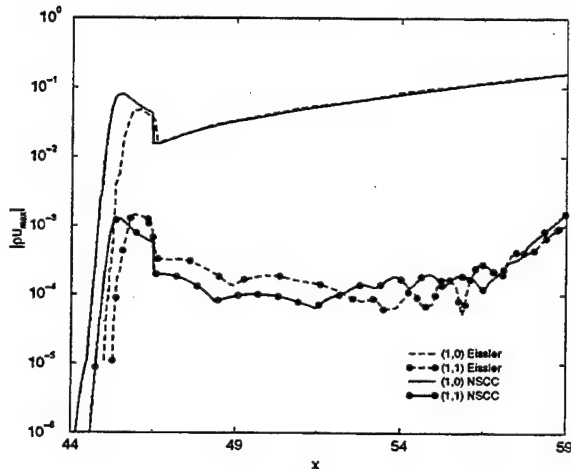
Figure 4.6 Comparison of the downstream development of the maximum amplitudes of $\rho u'$ for case C of Eissler (1995).

the disturbance slot are unknown, complicates the comparison of the downstream development of the maximum amplitudes. Nevertheless, the maximum $\rho u'$ amplitudes agree perfectly after the disturbance slot for the 2D disturbance. The 3D disturbances show similar behavior, i.e., the wiggles look alike and the fundamental resonance occurs at the same downstream location (see figure 4.6).

4.3   Incompressible Flow With Pressure-Gradient

4.3.1   Baseflow Simulation

As mentioned earlier, a Falkner–Skan similarity solution serves as initial condition for the generation of the baseflow. This initial condition has a Hartree parameter of $\beta_H = -0.181$ because, during the convergence of the baseflow, the shape-factor obtained from the DNS drifts to the theoretical value associated with $\beta_H = -0.18$. This is due to the domain height used for the DNS which is twice as high as the domain height of the simulations of Kloker (1993). The pressure distribution of the initial condition is kept constant at the free-stream. The flow properties for case ICVALFR are specified in appendix C, table C.2. The computational domain starts at $x = 1.585$ and ends at $x = 5.844$. The converged baseflow and the Falkner–Skan solution are plotted in Figure 4.7 and 4.8.

Figure 4.7 shows the u-velocity over η. The u-velocity is normalized by its free-stream value and η is calculated employing equation (3.13). Since this
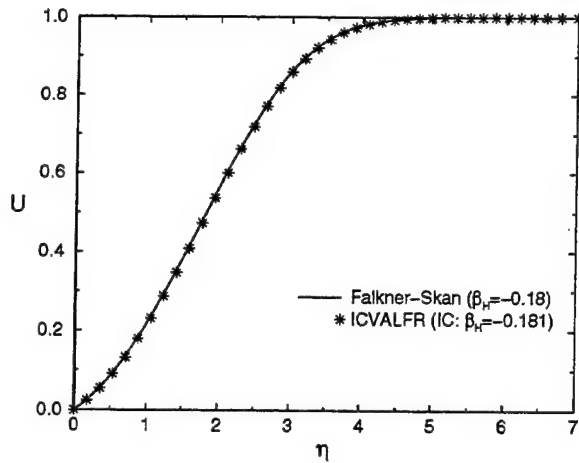
Figure 4.7 Comparison between Falkner–Skan solution and the baseflow obtained from DNS. The u-velocity profile is plotted over the similarity variable η.
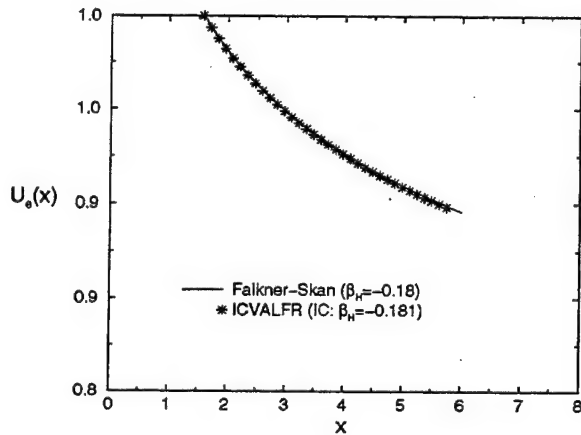
Figure 4.8 Comparison between Falkner–Skan solution and the baseflow obtained from DNS. Shown is the u-velocity at the free-stream over x.

profile is a similarity solution it does not change in the downstream direction. In Figure 4.8 the distribution of the edge velocity U_e over x is plotted. The Falkner-Skan values are calculated using equation (3.15). The baseflow matches the theoretical values of the Falkner-Skan solution except for a slight shift which is due to the initial condition. However, it is very important to compare more than only these variables to find out whether the same baseflow is predicted as by Kloker (1993). A very significant quantity is

the shape-factor H_{12}, which is defined as the ratio between the displacement thickness δ_1 and the momentum thickness δ_2, thus,

$$H_{12} = \frac{\delta_1}{\delta_2}. \tag{4.1}$$

The displacement thickness of an incompressible flow is given by the equation

$$\delta_1 = \int_0^\infty (1 - \frac{u}{U_e})dy. \tag{4.2}$$

It accounts for the growth of the boundary layer and defines the displacement of the potential flow at the free-stream by the value δ_1. The equation for the momentum thickness has the form

$$\delta_2 = \int_0^\infty \frac{u}{U_e}(1 - \frac{u}{U_e})dy. \tag{4.3}$$

Since the flow near the wall experiences friction, it loses momentum which is captured by the momentum thickness. The ratio of these quantities is a constant for a laminar flow which possesses a similarity characteristic. The reason for this fact is the similarity characteristic of the flow. The shape-
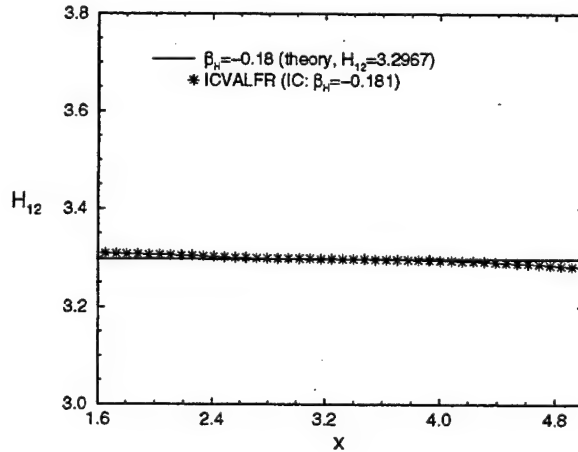
Figure 4.9 Shape-factor of the Navier–Stokes baseflow and the theoretical value of the similarity solution with $\beta_H = -0.18$.

factor obtained from the DNS (figure 4.9) matches the theoretical value for a flow with $\beta_H = -0.18$ between $x = 2.2$ and $x = 4.2$. The disturbance slot for the unsteady simulation with controlled forcing is located between $x = 2.082$ and $x = 2.293$. For this reason, the results of the unsteady calculation with

forcing are only compared to the results of Kloker (1993) downstream of $x = 2.2$. Downstream of $x = 4.2$, the 2D wave and the 3D wave start to interact with each other nonlinearly. The resolution of the simulation is too coarse to reproduce the correct physics for this stage. For this reason, it is not attempted to match Kloker's curves obtained from the high resolution simulation (case G) downstream of $x = 4.2$.

Before the results of the forced flow simulation are discussed, attention is being devoted to the Hartree parameter β_H. The initial condition has a constant Hartree parameter. It is of interest to see if this value is conserved in the DNS calculation. β_H can be computed in a post-processing step with its compressible definition. A program that reads in the data of the converged baseflow was written and tested with the previously described baseflow. The definition of β_H is

$$\beta_H = \frac{2\xi}{U_e(x)}\frac{dU_e(x)}{d\xi}\,, \tag{4.4}$$

with

$$\xi(x) = \int_0^x U_e(x)\rho_e(x)\mu_e(x)dx\,. \tag{4.5}$$

For incompressible flows with constant viscosity, μ_e and ρ_e are independent of x. Equation (4.5) is part of the Levy–Lee transformation (c.f. Schlichting & Gersten, 2000) which can be used with equation (4.4) to derive a self-similar compressible boundary layer with streamwise pressure gradient.

Since the inflow of the computational domain (see figure 3.1) is shifted by x_0 from the leading edge of the flat plate, ξ has to be calculated with

$$\xi(x) = \int_{x_0}^x U_e(x)\rho_e(x)\mu_e(x)dx + \xi_0\,, \tag{4.6}$$

where

$$\xi_0 = \int_0^{x_0} U_e(x)\rho_e(x)\mu_e(x)dx\,. \tag{4.7}$$

In most cases, the distribution of $U_e(x)$, $\rho_e(x)$ and $\mu_e(x)$ are not known upstream of the computational domain. That is the reason why equation (4.4) is easier to apply. If the Hartree parameter is given at the inflow, ξ_0 has the value

$$\xi_0 = \frac{\beta_H^{in}U_e^{in}}{2\frac{dU_e^{in}}{d\xi}}\,, \tag{4.8}$$

with

$$\frac{dU_e^{in}}{d\xi} = \frac{dU_e^{in}}{dx}\frac{dx}{d\xi} \tag{4.9}$$

and

$$\frac{dx}{d\xi} = \frac{1}{U_e^{in}\rho_e^{in}\mu_e^{in}}\,. \tag{4.10}$$

For β_H^{in} equal to zero, dU_e^{in}/dx is also zero. For this case, equation (4.7) leads to

$$\xi_0 = x_0 \,. \tag{4.11}$$

Figure 4.10 shows the result of the previous mentioned post-processing tool. The Hartree parameter of the DNS agrees very well with the theoretical value of the initial condition.
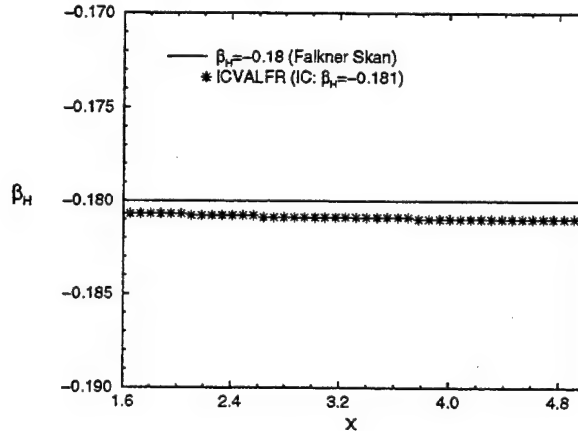

Figure 4.10 Hartree parameter distribution over x for the baseflow obtained from DNS.

4.3.2 Forced Flow Simulation

As comparison, a calculation is chosen in which Kloker (1993) simulated aligned Λ-vortices generated due to a strong pressure gradient. This physical process which creates aligned Λ-vortices is called fundamental resonance. Three Tollmien–Schlichting waves, one 2D and two 3D, interact which each other. When the 2D Tollmien–Schlichting wave reaches large amplitudes, it experiences a 3D deformation which is caused by the 3D waves. According to linear theory, 2D waves are more amplified than 3D waves for subsonic flows. However, when the 2D wave has a large amplitude, energy is being transferred to the 3D waves and their amplification rate changes significantly. The amplitude of the 2D wave saturates and the 3D waves can reach amplitudes of the order of the amplitude of the 2D wave.

The forced flow calculation of ICVALFR is conducted with almost the same computational setup as Kloker (1993) used for his simulation. Disturbances with the angular frequency $\beta = 10.8$ are introduced into the domain between $x = 2.082$ and $x = 2.293$. One streamwise wavelength λ_x contains 25 points and the domain height is about four boundary layer thicknesses high (Kloker

used only two boundary layer thicknesses). The computational parameters
are summarized in appendix C, table C.2. First, 2D calculations, where only
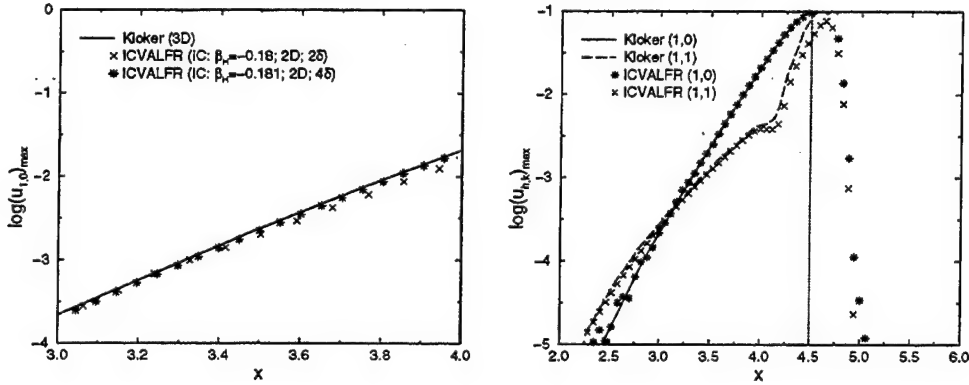

Figure 4.11 Amplitude distribution of the u-velocity versus x for the 3D
calculation with APG according to Kloker (1993): 2D (left) and 3D (right).

the 2D Tollmien–Schlichting waves were exited, were performed to determine
the correct domain height. The results of these simulations can be compared
to Kloker's 3D simulation since the development of the 2D wave for small
amplitudes behaves according to linear stability theory.
Figure 4.11 (left) illustrates the influence of the domain height on the am-
plitude distribution of the 2D wave. The calculation with four boundary
layer thicknesses as domain height can reproduce Kloker's data. The results
of the 3D calculation match Kloker's data as well. The amplitude distribu-
tion of the 3D Tollmien–Schlichting wave shown in figure 4.11 (right) attains
the same amplification as the 3D wave in Kloker's simulation for the linear
stage. At $x = 4.0$ the onset of the fundamental resonance can be observed.
Therefore, the slope of the amplitude distribution of the 3D wave deviates
from the slope predicted by linear stability theory. At $x = 4.25$, ICVALFR
starts to deviate significantly from Kloker's values. This is due to the buffer
domain which starts at $x = 4.5$.

4.4 Linear Stability Theory With Pressure Gradient

The linear stability solver of Mack is a very powerful tool with many options
to compute the linear stability behavior of different flow types. It contains
an additional tool that can generate the similarity solution for a compressible
flow over a flat plate without a pressure gradient. The output of this tool is
then read into the solver and the complex wavenumber for a specified local

Reynolds number, frequency and wave angle is calculated from this initial guess. Although the similarity solution of a compressible boundary layer has a different definition of the similarity variable η than the incompressible version, Mack still used the incompressible definition to transform the linear stability equations into the η coordinate system (c.f. Thumm, 1991) with

$$\eta = \frac{y}{x}R_x .$$ (4.12)

We demonstrated before, that for Mach 3, this procedure is a very good approximation.

Since the global Reynolds number of $Re = 100,000$ is fixed in the stability solver, Mack scaled the complex wavenumber by the factor R_x/Re to be independent of the Reynolds number

$$\alpha_r^{mack} = \alpha_r \frac{R_x}{Re}, \ \ \alpha_i^{mack} = \alpha_i \frac{R_x}{Re} .$$ (4.13)

For comparison with the DNS data, the complex wavenumber has to be rescaled by the Reynolds number which is used in the DNS simulation, i.e.,

$$\alpha_r^{DNS} = \alpha_r^{mack} \frac{Re^{DNS}}{R_x^{DNS}}, \ \ \alpha_i^{DNS} = \alpha_i^{mack} \frac{Re^{DNS}}{R_x^{DNS}} .$$ (4.14)

Flow properties:		Initial values:	
Ma	3	R_x	280
T_∞	$103.6K$	F	6.0×10^{-5}
Re	1578102	α_i	3.490×10^{-4}
$Wall$	$adiabatic$	α_r	2.712×10^{-2}

Table 4.1 Physical properties of the experiments (Brown, 2002) and the initial values for the 2D linear stability analysis.

How can a stability analysis with pressure gradient be performed without having any corresponding similarity solution? The solution for that problem can be found using the DNS data. The DNS calculations provide a converged baseflow with APG. This data must be transformed into the format which is read into the stability solver. A program was written in order to retrieve the necessary information from the DNS data at specified streamwise locations and to create the input data for the stability solver. Since, for this case, η (according to equation 4.12) is not a similarity variable, the linear stability analysis can only be performed locally. For every streamwise location a new

input profile must be generated. As initial guess, the complex wavenumber of a previous stability analysis of a similarity profile with the same physical properties (except APG) is used. To validate this procedure, a 2D stability analysis with the physical properties of the experiments by Graziosi & Brown (2002) and without APG was performed (see table 4.1). The investigated profiles were the similarity solution of Mack's similarity solver and the input profiles created from the corresponding DNS data by the procedure discussed above. In table 4.1 the flow properties, disturbance frequency, start location and the initial eigenvalues are listed. The stability analysis started at $R_x = 280$ and ended at $R_x = 880$. The initial eigenvalues are the local solution for position $R_x = 280$.
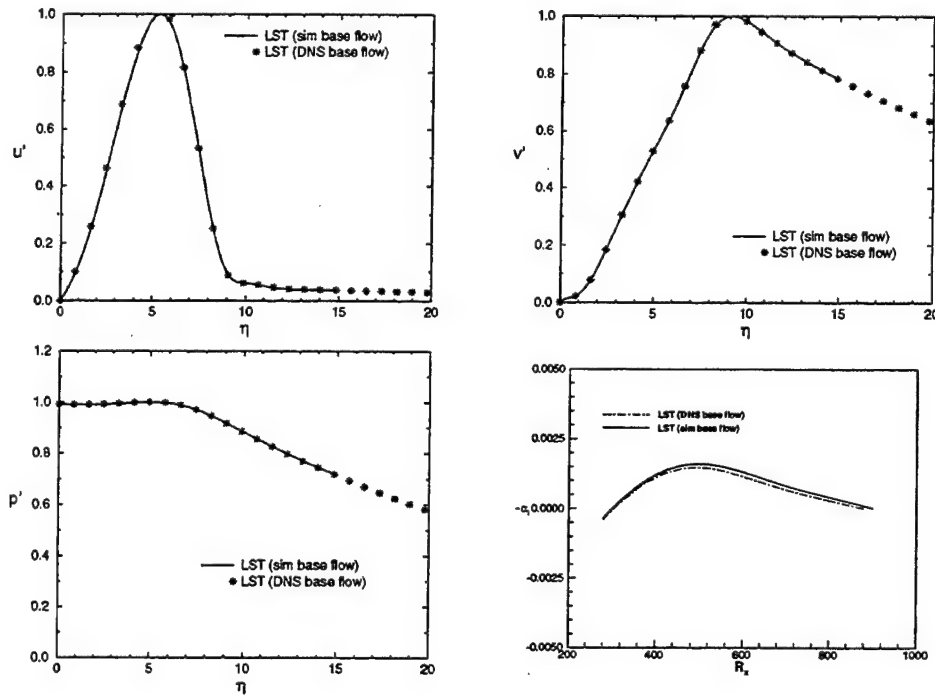

Figure 4.12 Eigenfunctions of u-velocity (top left), v-velocity (top right) and pressure (bottom left) disturbances at $R_x = 280$ and amplification rate α_i over R_x (bottom right) from stability calculations using the similarity solution and the DNS profiles.

Figure 4.12 shows the results obtained using this stability analysis. The eigenfunctions of u, v and p at position $R_x = 280$ and t the amplification rate α_i over R_x are plotted. Like for every numerical simulation, the optimal domain height of the integration domain and the largest spatial stepsize

that still gives the correct physical result had to be determined. Therefore, for the DNS baseflow profile, which was read into the stability solver, a resolution and domain height study was carried out. It was observed that for a large number of points in the boundary layer in the wall-normal direction (more than 200 points) Mack's stability solver could not produce a correct amplification rate α_i anymore. This fact marks a limit for all DNS based linear stability investigations for the present research and it could be the explanation for the difference of approximately 7.5% between the growth rate using the similarity solution as input profile and the growth rate using the DNS data as an input shown in figure 4.12. The difference of around 7.5% of the growth rate is determined at the location of the maximum growth rate using the similarity solution as input and is based on this maximum value. However, the difference could also be caused by the slight discrepancy in the profiles of the similarity solution and the DNS data.

## 4.5   Compressible Flow With Adverse Pressure-Gradient
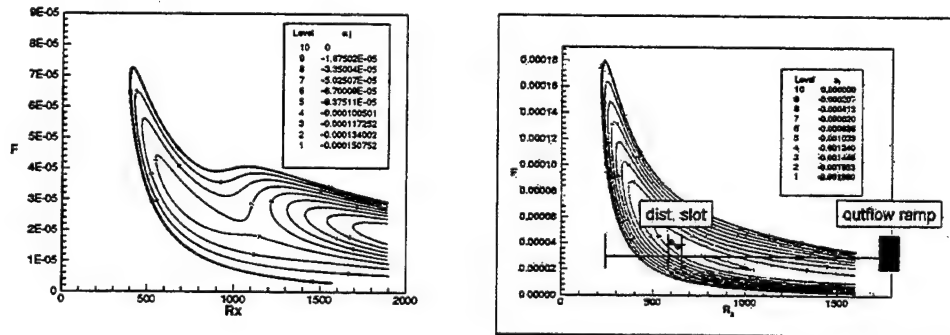
Figure 4.13 Linear stability diagrams for $Ma = 3$, $T_\infty = 103.6K$, adiabatic wall: $\Psi = 0°$ (left) and $\Psi \simeq 65°$ (right). The region outside of the contours represents the region of damped frequencies.

In this section two DNS calculations, one with and one without APG, are presented. The flow properties are listed in table 4.1. A more detailed table which summarizes the computational parameters for the DNS can be found in appendix C, table C.2. Both calculations were performed with small disturbance amplitudes, so that they can be compared to LST. 3D disturbances were excited in the disturbance slot. This choice was motivated by the stability properties of the flow. The 2D linear stability diagram is shown in figure 4.13 (left). Two instability modes are present, a viscous (Tollmien–Schlichting type) and a second (inviscid or Mack) mode. The latter is more amplified. It is very difficult to excite only one particular instability mode

without exciting the other one. Preliminary 2D DNS revealed that both instability modes were always present in the flow field and that the Mack mode, which was not of interest, was only weakly damped. In contrast, the 3D linear stability diagram (figure 4.13, right) contains only the first (TS-type) mode. This simplifies the post-processing of the computational data since it is not necessary to decompose the flow field into the different instability modes. The disturbance waves are introduced at a wave angle of $\Psi \simeq 65°$. This angle is chosen because it represents the angle of the most amplified wave (Mack, 1984). For one frequency the spanwise wavenumber is a constant and the streamwise wavenumber is a function of x. For this reason, the wave angle varies and cannot have the value of $\Psi = 65°$ in the whole computational domain. The spanwise wavenumber which is used for the linear stability analysis is defined by the following equation (Eissler, 1995)

$$\gamma = d\,F\,Re\,,\qquad(4.15)$$

where d is a constant that defines in which range the wave angle is located. In Mack's stability solver the streamwise wavenumber α is normalized by the ratio R_x/Re (see section 4.4). This scaling is also applied to the spanwise wavenumber. Therefore, equation (4.16) can be modified to

$$\gamma^{mack} = dFR_x\,.\qquad(4.16)$$

Table 4.2 lists the values of d for both linear stability analyses. d is chosen in a way such, that Ψ is equal to 65° at the R_x locations where the amplitude distributions of the DNS and the eigenfunction of the LST are compared to each other.

No pressure gradient:		Pressure gradient:	
d	3.0	m	3.5

Table 4.2 Constant d for the two different simulations.

4.5.1 Simulation Without Pressure Gradient

Figure 4.13 (right) shows the stability diagram for the simulation without any pressure gradient. The domain starts at $R_x = 250$ and ends at $R_x = 1893$. Disturbances of frequency $F = 3 \times 10^{-5}$ are introduced into the domain between $R_x = 594$ and $R_x = 655$. The buffer domain starts at $R_x = 1722$. The computational domain is very long since at the location $R_x = 1400$, where the DNS is compared to the LST data, influences of the disturbance

slot and non-parallel effects are required to be weak. The resolution in the x- and y-directions is chosen such that one streamwise wavelength λ_x is resolved by eleven points and at the end of the domain, 100 points are within the boundary layer in the wall-normal direction. The domain height is two boundary layer thicknesses at the outflow. This domain height is also used by Thumm (1991) for his linear stability investigations.
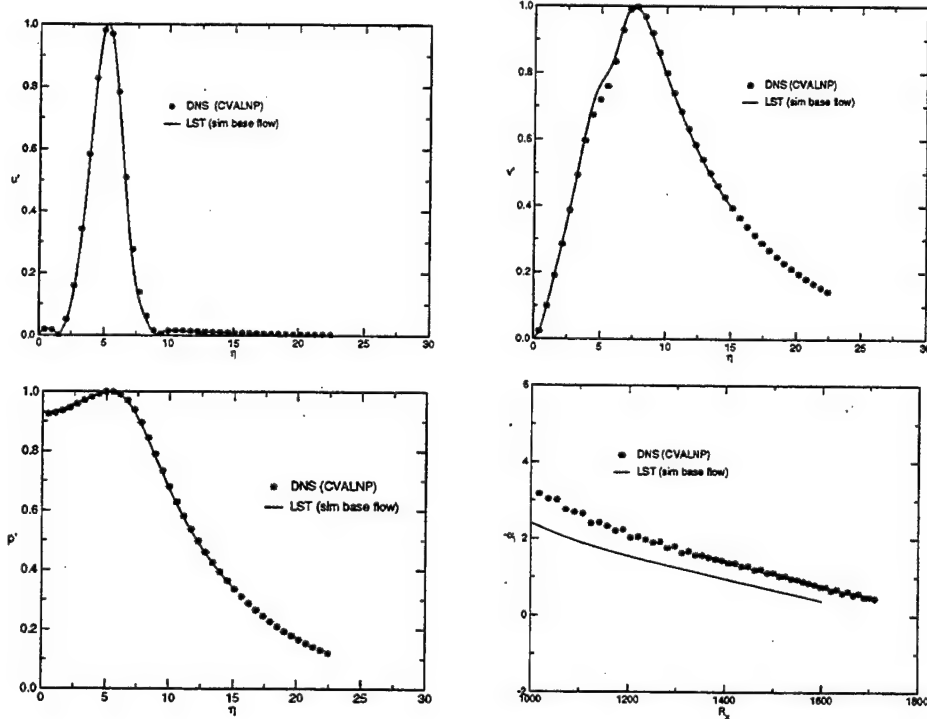

Figure 4.14 Amplitude distribution of the u-velocity (top left), v-velocity (top right) and pressure (bottom left) at $R_x = 1400$ and amplification rate α_i over R_x for $\Psi \simeq 65°$ (bottom right).

In figure 4.14, the amplitude distributions obtained by the DNS are compared to the eigenfunctions of the LST. In the plot for the u-velocity (top left), it is visible that for a 3D wave the eigenfunction has a second maximum close to the wall. Next to the location of the second phase shift, the amplitude distribution from the DNS varies slightly from the LST. This discrepancy was also observed by Thumm (1991). The v-velocity from the DNS shows a large difference to the LST results for $4 \leq \eta \leq 6$. The deviation becomes smaller when the DNS baseflow is used for the linear stability analysis (see section 4.5.2). In figure 4.14 (bottom right) the amplification rate α_i over R_x is plotted. It is calculated from the maximum value of the u-velocity

perturbations in y. The value based on the LST deviates by 27% from the DNS solution and the deviation increases to infinity for α_i^{DNS} equal to zero. This means that the DNS predicts a higher amplification rate than LST. Thumm (1991) concluded that the non-parallel effects, which are caused by the growth of the boundary layer, are responsible for this behavior. But he did not present any proof for this statement.
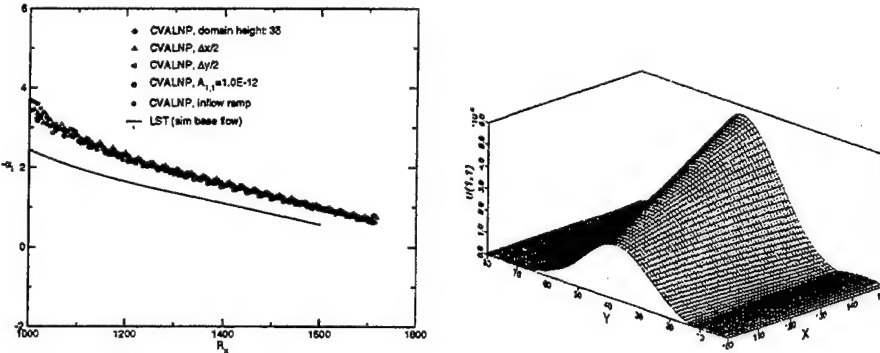

Figure 4.15 Amplification rate α_i of the resolution study over R_x for $\Psi \simeq 60°$ (left) and Fourier-transformed u-velocity in time (right, the amplitude distribution between points $100 - -150$ in x and points $1 - -80$ in y is plotted).

To validate if the DNS values are correct a resolution study was carried out. The results are shown in figure 4.15 (left). All cases (with different resolution in the x- and y-directions, larger domain height, smaller disturbance amplitude and different inflow buffer domains) reproduced identical results, thus, indicating a well-resolved simulation. The saw-toothed shape of the curves in figure 4.15 is an artifact of the post-processing and can be eliminated by interpolating the locations of the u-velocity maxima. Figure 4.15 (right) illustrates that the original DNS data after the Fourier-transformation in time has indeed a very smooth distribution.

4.5.2 Simulation With Adverse Pressure Gradient

Figure 4.16 shows the linear stability diagram for the compressible validation case with APG. The dashed-dotted line represents the neutral curve of figure 4.13 (right). Only the region between $R_x = 1000$ and $R_x = 1600$ includes an APG. For the case with APG, the neutral curve is shifted to higher frequencies and the highest amplification rate α_i is approximately three times larger than for the case with $\beta_H = 0$. β_H is not a constant and it is plotted in figure 4.17. The value of β_H is calculated with the post-processing tool
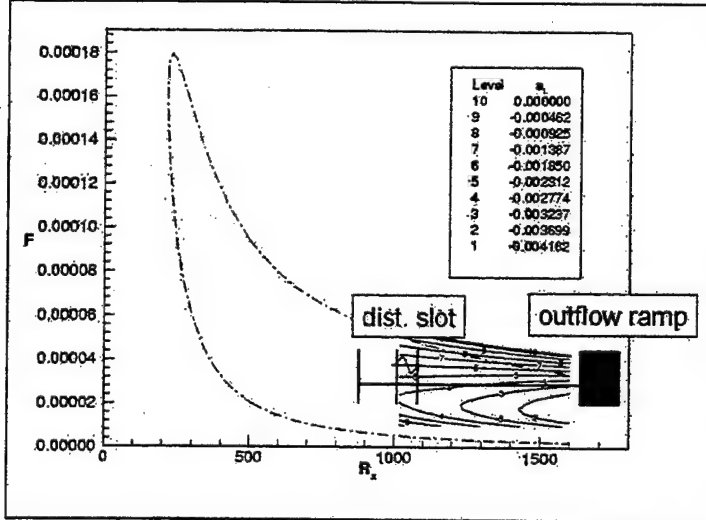
Figure 4.16 Stability diagram for $Ma = 3$, $T_\infty = 103.6K$, adiabatic wall and $\Psi \simeq 65°$. Dashed-dotted line indicates the neutral curve without APG. The region between $R_x = 1000$ and $R_x = 1600$ is the stability diagram with APG.
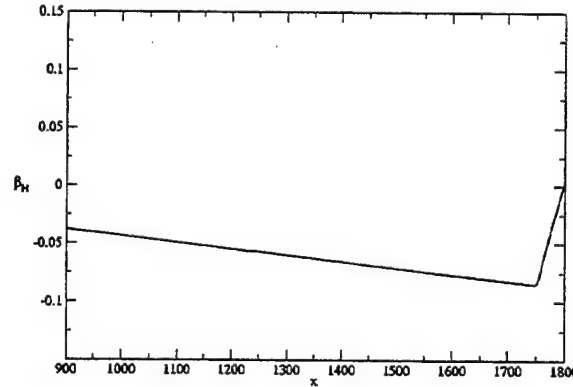

Figure 4.17 β_H for compressible validation case with APG (case CVALPG).

described in section 4.3.1. The pressure distribution of the DNS calculation is plotted in figure 4.18 (left). In § 3.4.4, it was already discussed how a converged baseflow with adverse pressure-gradient is obtained. A pressure distribution is introduced on a baseflow through the upper boundary. This baseflow is converged out and then the regions which are not needed are cut off. Figure 4.18 (right) shows the original pressure distribution.

The computational domain of the forced flow calculation starts at $R_x = 899$ and ends at $R_x = 1822$. Disturbance waves with the angular frequency of $F = 3 \times 10^{-5}$ are introduced through the disturbance slot located between
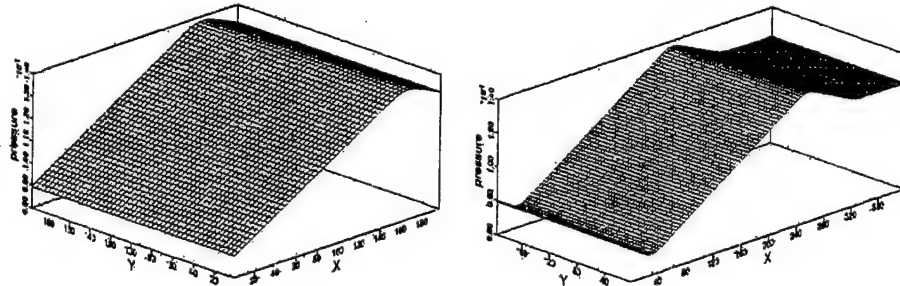
Figure 4.18 Pressure distribution of the DNS calculation (case CVALPG): after (left) and before (right) the computational domain is cut; only every fourth point is shown for clarity.

$R_x = 1048$ and $R_x = 1083$. The buffer domain starts at $R_x = 1640$. The resolution in x and y is the same as for the calculation without APG (case CVALNP). Therefore, only ten points resolve one streamwise wavelength λ_x and 80 points in the wall-normal direction are within the boundary layer at the end of the computational domain. Compared to the case without pressure gradient (case CVALNP), the boundary layer for case CVALPG is thinner. Incompressible flow behaves very differently. An APG always thickens an incompressible boundary layer in order to conserve its mass flux. For compressible flows, an APG causes the density to increase and, consequently, produces a larger mass flux in the boundary layer without the need to thicken it. If the increase in density is strong enough, the boundary layer can even become thinner.

In figure 4.19, the amplitude distributions from the DNS are compared to the eigenfunctions obtained using LST. The u-velocity (figure 4.19, top left) matches the theoretical values pretty well. The discrepancy between the DNS and the LST results for the v-velocity at $\eta \approx 5$ is much smaller than for case CVALNP. This corroborates the previous statement that it makes a difference whether the DNS baseflow or the similarity solution is used for the LST analysis. For higher values of η, the amplitude distribution of the DNS deviates from the theory. After a domain height study it was concluded that this deviation is caused by the upper boundary condition of the stability solver. With increasing domain height this difference decreases. In figure 4.19 (bottom right) the amplification rate α_i versus R_x is plotted. Like for case CVALNP, the waves predicted by the LST calculations are amplified about 25% less than the waves obtained by employing DNS.

Figure 4.20 shows the results of the domain height study for the stability
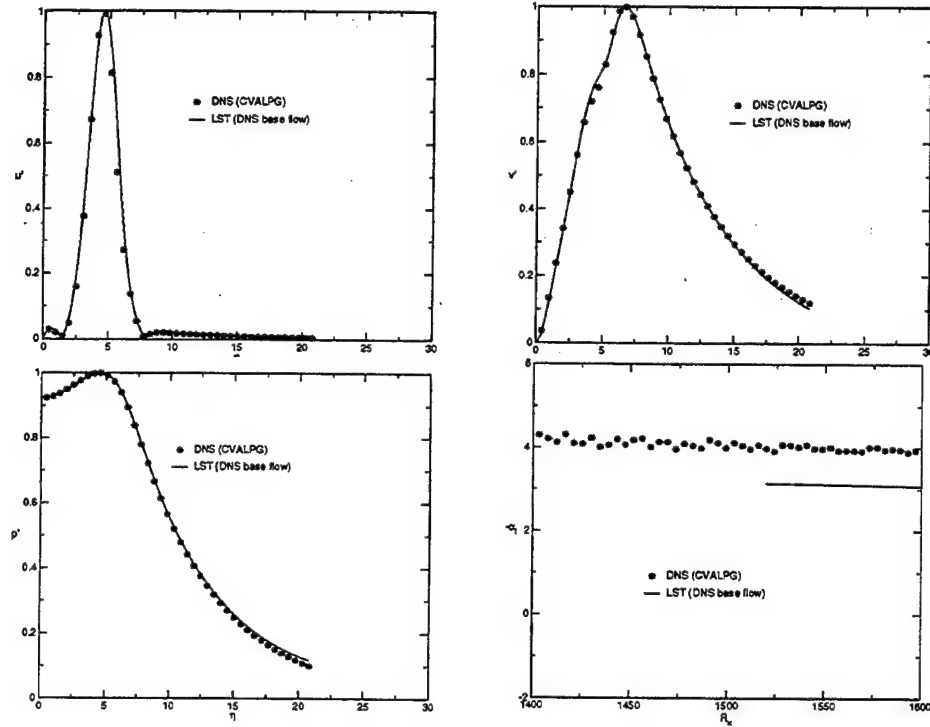
Figure 4.19 Amplitude distribution of the u-velocity (top left), v-velocity (top right) and pressure (bottom left) at $R_x = 1510$ and amplification rate α_i over R_x for $\Psi \simeq 65°$ (bottom right).
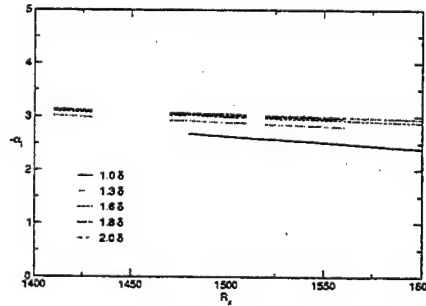
Figure 4.20 Amplification rate α_i versus R_x. Domain height study for the linear stability solver of Mack ($\Psi \simeq 61°$).

solver of Mack. The graph indicates that the domain height has a significant impact on the amplification rate α_i. With increasing domain height, α_i converges to the value that is obtained when the domain height of the stability solver is chosen to be two boundary layer thicknesses.

5. PRINCETON EXPERIMENTS

At Princeton University, Professor Brown and co-workers performed an experimental study of stability, receptivity and transition of a flat plate boundary layer at Mach 3. For a detailed description see Graziosi (1999) and Graziosi & Brown (2002). In the following, only a short summary of their work is presented.
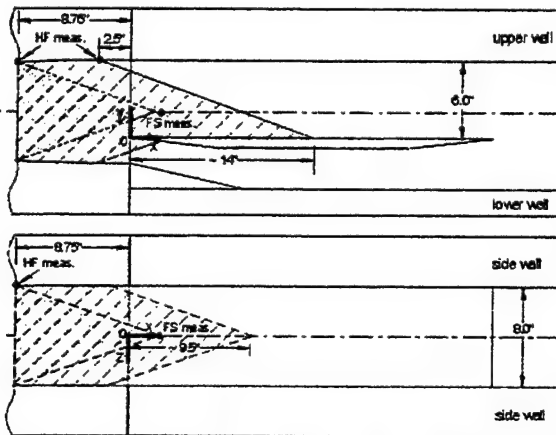

Figure 5.1 Quiet region of LVTG windtunnel (reproduced from Graziosi & Brown, 2002).

The Low Turbulence Variable Geometry (LTVG) wind tunnel with a turbulence rate of 0.11% to 0.39% provides a 28.5" long and 8" wide flat-plate in the test section. However, the quiet region, i.e., the region before a shock wave is reflected at a tunnel wall and hits the boundary layer again, is about 9.5" long and, consequently, reaches only a maximum local Reynolds number of $R_x = 725$ (see figure 5.1).

Mean flow investigations were performed at a stagnation pressure of

$$p_s = 5psia$$

whereas, due to the lower turbulence level, the transition investigation was carried out at a stagnation pressure of

$$p_s = 4psia.$$

For a summary of the operating conditions see table 5.1.

Hot wire measurements were performed at five different downstream locations between $R_x = 400$ and $R_x = 800$ along the centerline of the plate. The data acquisition locations were chosen from the location of the critical Reynolds

p_0	$[psia]$	4.0	4.2	5.0
ρU_∞	$[\frac{kg}{m^2 s}]$	15.8	16.5	19.7
U_∞	$[\frac{m}{s}]$	610.5	610.5	610.5
Re/m	$[-]$	2.18×10^6	2.29×10^6	2.72×10^6
$< \rho u > /\rho_\infty U_\infty$	$[\%]$	0.11	0.16	0.39

Table 5.1 Operating condition of LTVG and measuered free-stream turbulence level.

number on downstream. Intensive calibration and mean flow surveys assured a relatively small error in the measured data.

Natural disturbances coming from the upper edges of the wind tunnel penetrated the boundary layer and excited disturbances. For recent studies a loudspeaker was located in the free-stream to introduce controlled disturbances. For both cases, free-stream turbulence was present influencing the measurements. Frequencies under investigation were:

- $F = 1.4 \times 10^{-5}$–begin of the instability region (branch I),

- $F = 5 \times 10^{-5}$–region of maximum amplification of disturbances,

- $F = 8.1 \times 10^{-5}$–end of the instability region (branch II),

i.e., 3,000 Hz, 10,500 Hz and 17,000 Hz, respectively. All cases under investigation are illustrated in the linear stability diagram of figure 5.2.
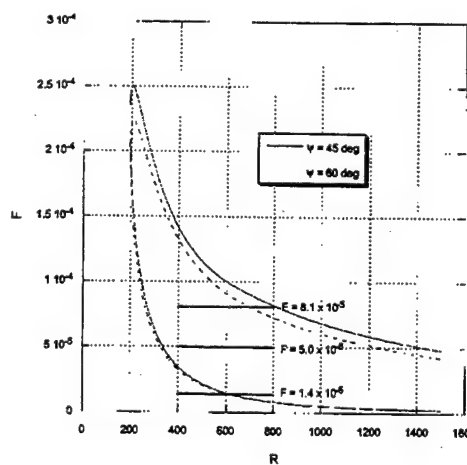

Figure 5.2 LST–diagram with investigated cases (reproduced from Graziosi, 1999).

6. RESULTS AND DISCUSSION

6.1 Baseflow Simulations

All computations are carried out on a grid according to the results of the grid convergence study in appendix B.1, i.e., the domain length is twelve λ_x of the corresponding TS–wave, the domain height is nine $\delta_{outflow}$ with an equidistant grid for the first two boundary layer thicknesses and a stretched grid above. The disturbance slot is located one wavelength downstream of the inflow boundary and is $1/2\,\lambda_x$ long (exemptions are clearly stated). The resolution is 32 points per λ_x and ten points per δ_{inflow}.

6.1.1 Comparison With Similarity Solution

The difference between the similarity solution and the baseflow, i.e., the steady solution to the Navier–Stokes, equations should be small. This conjecture is corroborated in the following. First, the boundary layer thickness is compared in table 6.1, where δ^* denotes the dimensional boundary layer thickness. As reference case serves the boundary layer thickness after von Mises (c.f. Schlichting & Gersten, 2000) for a laminar, zero pressure-gradient, incompressible flat-plate boundary layer:

$$\delta^* = 5\sqrt{\frac{\nu^* x^*}{u_\infty^*}}\,.\tag{6.1}$$

$\delta^*\ [10^{-3}m]$	von Mises	Navier–Stokes	similarity solution
$R_x = 467$	1.0711	1.99097	1.962
$R_x = 636$	1.4872	2.68348	2.6546
$R_x = 769$	1.76371	3.34714	3.2029
$R_x = 864$	1.981655	3.6645	3.6357

Table 6.1 Boundary layer thickness comparison.

Table 6.1 shows that the estimate according to von Mises is only a rough guess for compressible flows, while the small difference between the similarity solution and the Navier–Stokes solution is most likely due to the presence of a small favorable pressure-gradient (see below). The maximum deviation within the flow field is about 3% in the u-velocity. In figure 6.1, the similarity solution and the baseflow, normalized with the value at the edge of the boundary layer, are compared. The increased boundary layer thickness, as already shown in table 6.1, can be observed for the u-velocity. While the
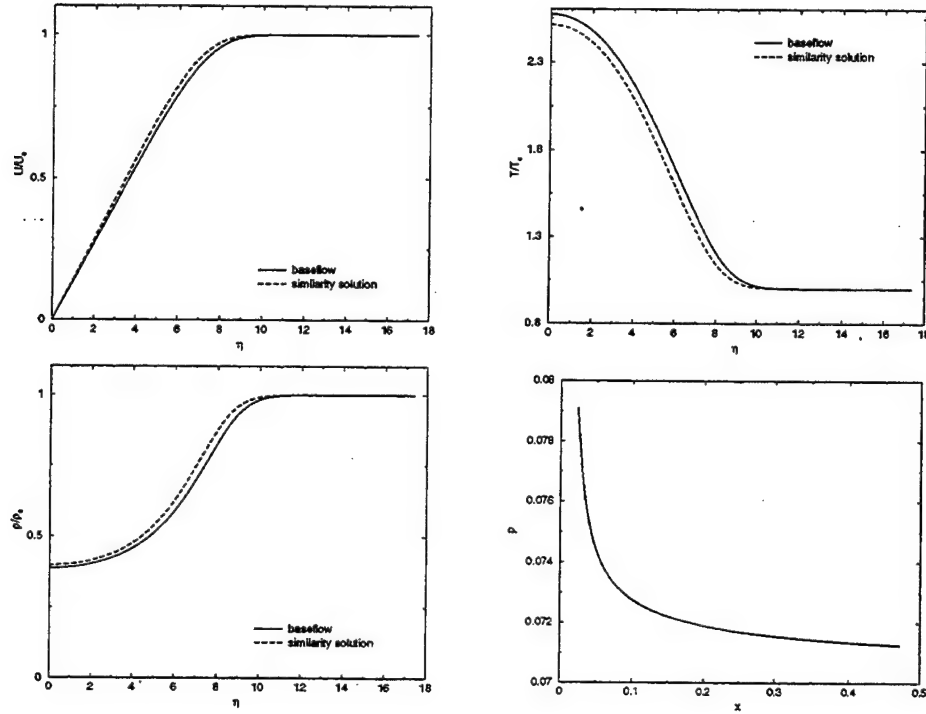
Figure 6.1 Comparison of Navier–Stokes and similarity solution: u-velocity (top left), temperature (top right), density (bottom left) and the pressure distribution of the Navier–Stokes solution in the streamwise direction (bottom right).

density ρ shows only a minor deviation, the temperature at the wall is larger for the Navier–Stokes baseflow than for the similarity solution. However, the difference at the wall is only $6K$. This discrepancy is considered to have an insignificant impact on the stability characteristics of the flow. Nevertheless, the difference in the density and temperature results in a favorable pressure gradient in the streamwise direction because the equation of state governing the pressure still has to be valid. Figure 6.1 (bottom right) shows a typical pressure distribution in streamwise direction while the pressure in the y-direction is constant.

By scaling data at three different downstream locations using the similarity variable η, figure 6.2 shows that all three profiles perfectly match. This demonstrates that the flow is indeed self-similar. Matching the pressure gradient in the region of interest with a Falkner–Skan similarity velocity profile led to a Hartree–parameter of 4.2×10^{-3} which is close enough to zero to assume a zero pressure-gradient flat-plate boundary layer flow. However,
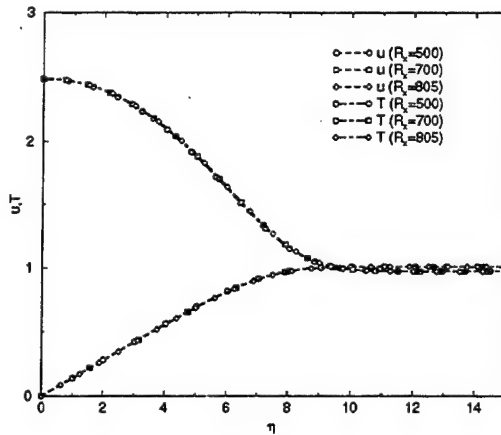
Figure 6.2 Navier–Stokes solution profiles in similarity variable η for different downstream locations.

using profiles of the the Navier–Stokes solution as a baseflow for a LST analysis results in a smaller unstable region due to the favorable pressure gradient (see figure 6.3). One could, therefore, conclude that the Navier–Stokes baseflow should be more stable with respect to disturbances than the similarity solution. However, a later discussion will show that this statement is not generally true (see § 6.2.4).
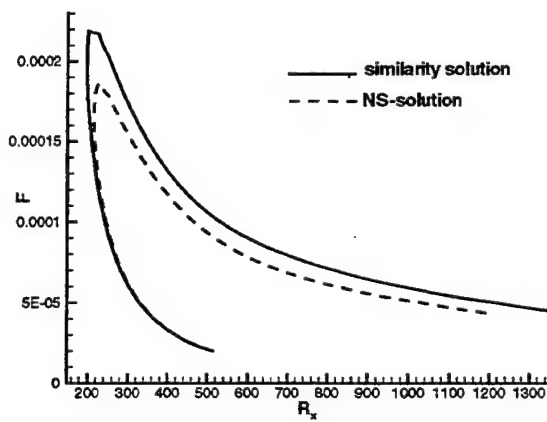
Figure 6.3 LST diagram of similarity and Navier–Stokes solution for $\Psi = 60°$.
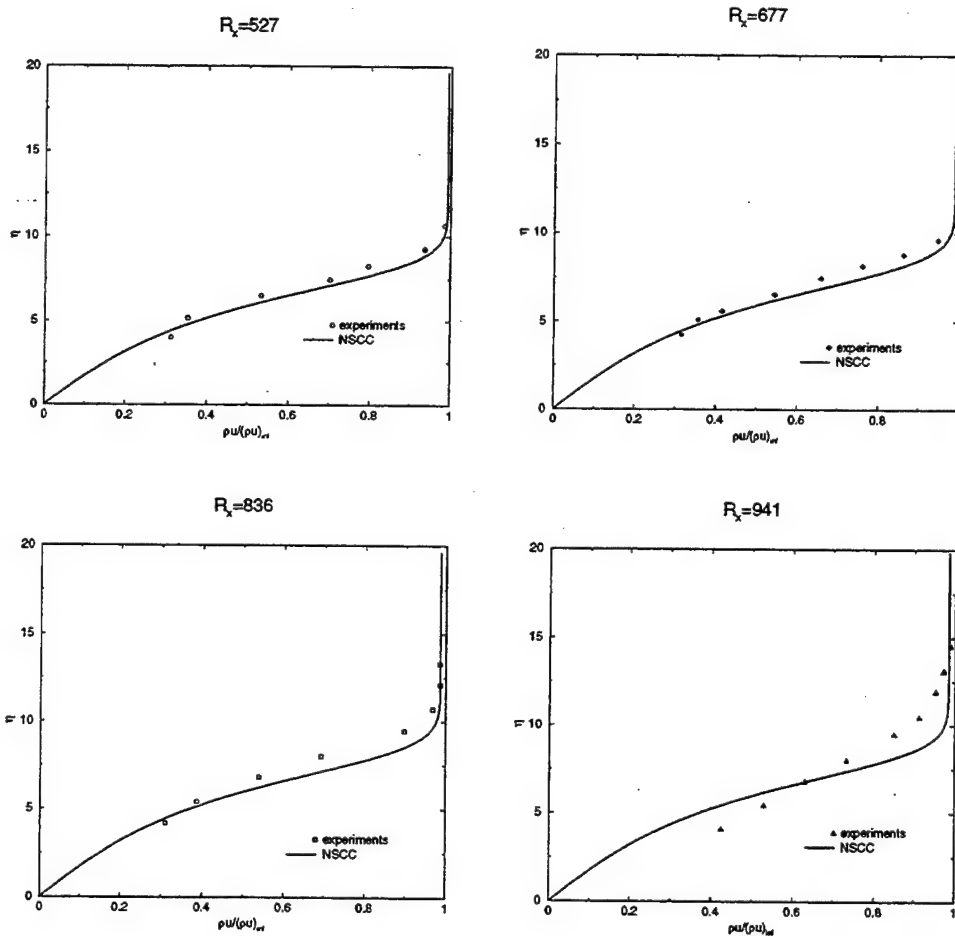
Figure 6.4 Comparison of computation and experiment at different downstream locations.

6.1.2 Comparison with Experiments

In the experiments, baseflow investigation at a stagnation pressure of 5 psia are performed. Hot wire measurements of the mass flux at different downstream locations and the computed streamwise momentum are compared in figure 6.4. The very good agreement also confirms that the baseflow simulation captures the mean flow properties at Mach 3 correctly. The slightly different profiles farther downstream stem from the reflected shock wave (see figure 5.1). In the experiments, the pressure distribution (figure 6.5) shows only small pressure deviations in the streamwise direction, but, because of the uncertainty in the experimental measurements, an overall (favorable)

pressure-gradient could still be present, explaining the good agreement with the computations.
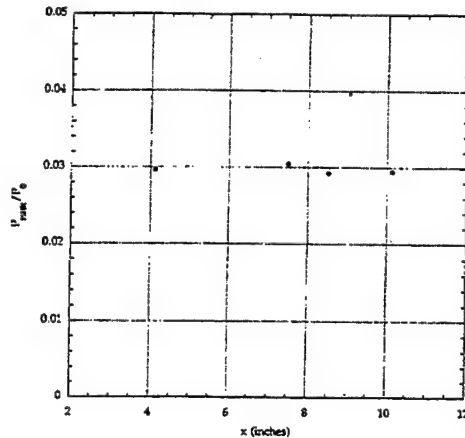
Figure 6.5 Pressure distribution along the middle axis of the plate (reproduced from Graziosi, 1999).

6.2 Linear Stability Behavior

6.2.1 Disturbance Frequency $F = 1.4 \times 10^{-5}$

From a computational point of view, the disturbance frequency of $F = 1.4 \times 10^{-5}$ ($f^* = 3,000Hz$) is problematic because a very large TS–wavelength of $\lambda_x = 0.127m$ is linked to this set up. Because of the space needed for
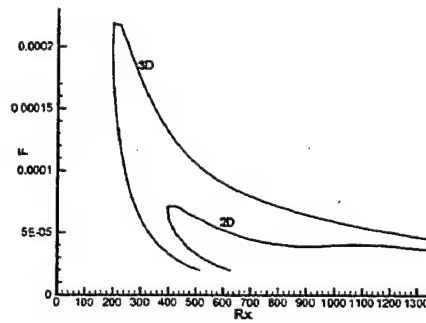
Figure 6.6 LST stability diagram for $\Psi = 60°$ and $\Psi = 0°$.

disturbance generation (see § 3.6), the inflow boundary approaches the virtual origin $(x_0 \to 0)$ in figure 3.1 and a very fine computational grid has to be used in order to maintain numerical stability. To reduce the computational cost, computations on an immediately stretched grid were carried out and the forcing slot was located only 15 grid points from the inflow boundary with an extremely small width of only five grid points. Even using this disturbance generation configuration, there is only half a wavelength space in the downstream direction before the disturbance wave enters the unstable region (branch I). For all other computational parameters, see appendix C, table C.3.

Comparison with Experiments

To check, if the right disturbances are introduced, the TS–wavelength obtained in the computations is compared to the experimental data in table 6.2. The result is off by a single Δx indicating that the correct TS–wave is captured.

	λ_x
computation [m]	0.127
experiments [m]	0.122

Table 6.2 Wavelength comparison of computation with experiments for $F = 1.4 \times 10^{-5}$.
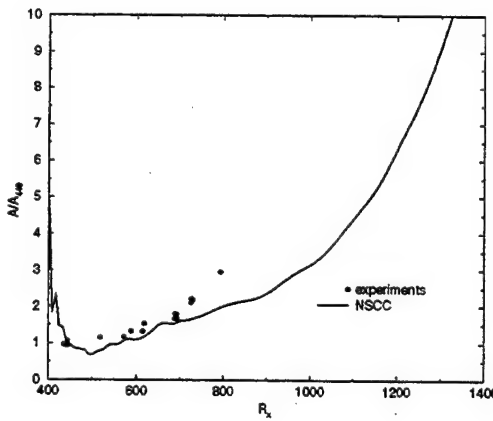

Figure 6.7 Amplitude distribution comparison of experiment with computation for $F = 1.4 \times 10^{-5}$ $(f^* = 3,000Hz)$.

In figure 6.7, the amplitude distribution in the streamwise direction is plotted. The amplitude of the introduced disturbance initially decreases rapidly.

Therefore, the flow is not fully developed causing the wiggles in the amplitude distribution. So it is questionable if the physically right amplitude at $R_x = 440$ is used for normalization. In both cases, the amplitude grows at about $R_x = 500$ which is earlier than predicted by LST. Farther downstream, the computation shows a smaller amplitude than the experiments, probably caused by the normalization. Nevertheless, the data match reasonably well.
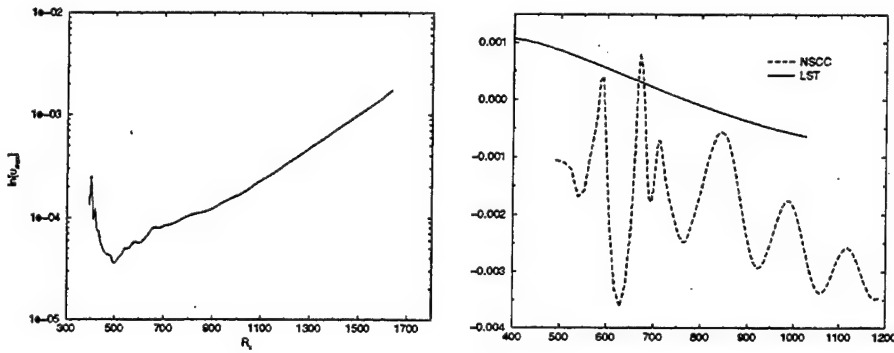

Figure 6.8 Maximum u'-amplitude (left) and amplification rate (right) over R_x for $F = 1.4 \times 10^{-5}$.

Comparison with LST

The region of interest is too close to the disturbance slot (see figure 6.6). Due to the reasons mentioned above, this fact cannot be changed easily. As a consequence, the TS-wave is still developing which causes the waviness of the amplitude and amplification rate plots in figure 6.8. Instead of the amplification rate, the maximum u'-amplitude is therefore used to give some indication of the flow instability. The maximum amplitude in figure 6.8 shows a growing amplitude from $R_x = 500$ which coincides with the experiments but is earlier than LST (see figure 6.6). Due to the lack of data farther upstream, it is inconclusive what causes this effect. From $R_x = 700$ on, the logarithmic plot (figure 6.8) shows linear behavior, i.e. exponential growth of the disturbance amplitude, which is consistent with LST.

In figure 6.9, the eigenfunctions of LST do not differ too much–their shape stays the same. The discrepancies stem mainly from the different instability modes present during wave development. The phase distributions show an earlier phase shift for the similarity solution than for the Navier–Stokes solution because of the thicker boundary layer of the latter. Comparing the eigenfunctions with the amplitude distribution from the DNS computation, the second maximum at $\eta = 10$ is considerably larger, while for ρ' and T', the first maximum is smaller. The shape of the eigenfunctions of the computa-

tion is not similar to the two LST–eigenfunctions, because at $R_x = 700$, the disturbances have only travelled one wavelength downstream so that the first maximum has not yet fully developed. The absolute value of the phase distribution is different but the phase shifts are consistent with the eigenfunctions.
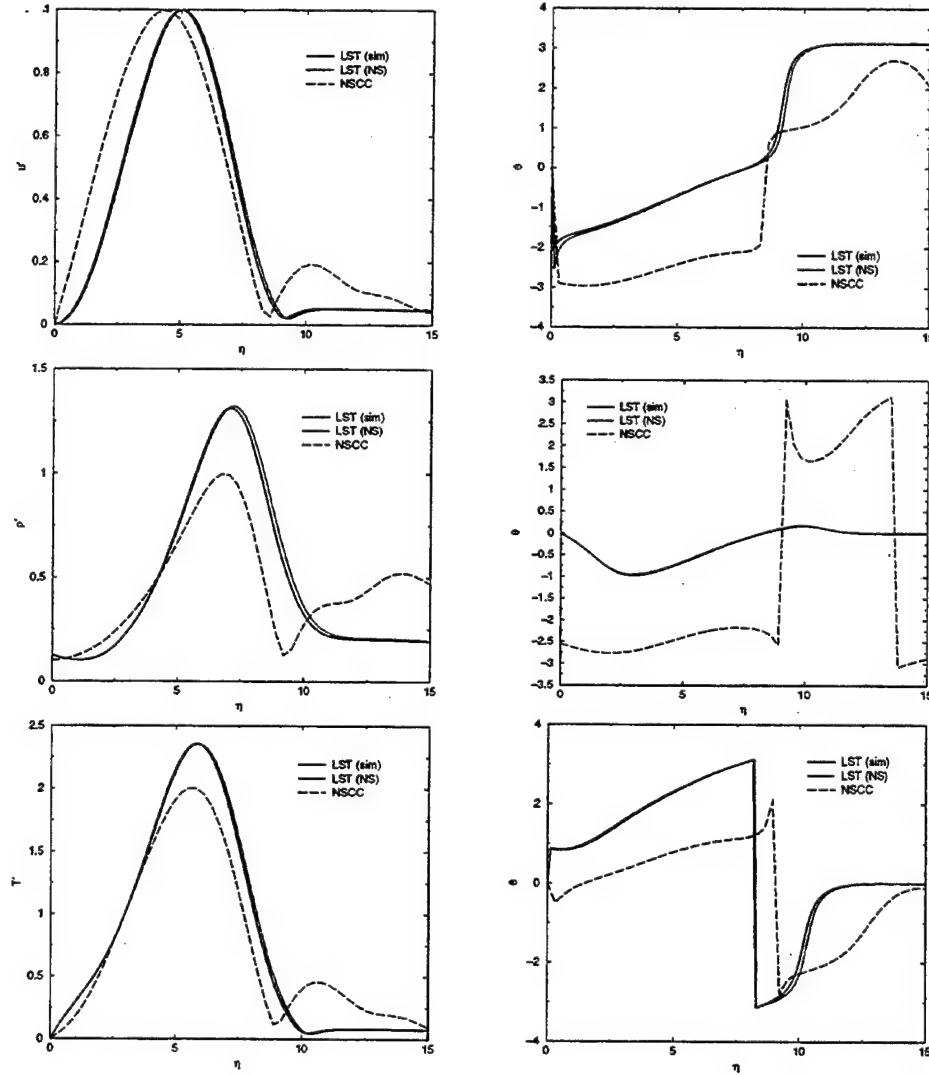

Figure 6.9 Comparison of amplitude (left) and phase (right) distribution of the computation to LST based on the similarity and the Navier–Stokes solution; shown are u-velocity (top), density (center) and temperature (bottom); $F = 1.4 \times 10^{-5}$, $R_x = 700$.

6.2.2 Disturbance Frequency $F = 5.0 \times 10^{-5}$

This case was chosen due to its proximity to the region of maximum amplification rate. For computational parameters, see appendix C, table C.4.

Comparison with Experiments

Comparison of the TS–wavelengths gives confidence that the same disturbances as in the experiments are introduced (see table 6.3).

	λ_x
computation [m]	0.0376
experiments [m]	0.0376

Table 6.3 Wavelength comparison of computation with experiments for $F = 5 \times 10^{-5}$.

In figure 6.10, the DNS results are compared with the experimental data. Shown are the amplitude distribution for different downstream locations and the amplification rate at $R_x = 500$ for different frequencies. The simulations and the experiments match fairly well at lower R_x. The larger amplitude for the computation farther downstream suggests that non-linearities are present in the experiments–probably because of the reflected shockwave at $R_x \simeq 700$ (see § 5).
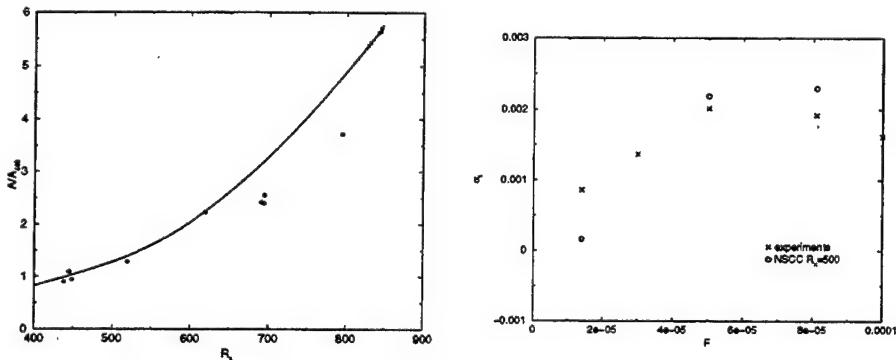

Figure 6.10 Comparison of experiment with computation for $F = 5 \times 10^{-5}$: amplitude distribution over R_x (left) and amplification rate at $R_x = 500$ for different frequencies.
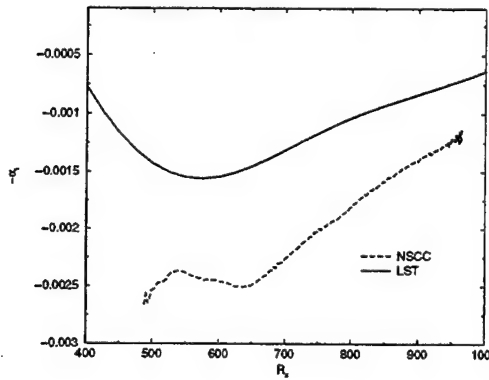
Figure 6.11 Amplification rate comparison of computations with results from LST for $F = 5 \times 10^{-5}$ $(f^* = 10,500 Hz)$.

Comparison with LST

The computations and the experimental data both show a larger amplification rate than LST, where the amplification rate of the computations is even larger than in the experiments (see figure 6.10, right). In figure 6.11, the maximum amplification rate is significantly larger compared to LST. Farther downstream, the amplification rate curve approaches the LST-curve which can also be seen in figure 6.11. As shown in figure 6.12 the amplitude distributions of the computation are wider compared to the LST-eigenfunctions, both with similarity and Navier–Stokes baseflows. The first maximum of the u'-amplitude distribution of the computation is not as large, but all eigenfunctions match in the free-stream ($\eta \geq 10$). The phase distributions are similar with the phase shifts consistent to the eigenfunctions.

6.2.3 Disturbance Frequency $F = 8.1 \times 10^{-5}$

In this case, the branch II of the stability diagram for a wave angle $\Psi = 60°$ is crossed at $R_x = 700$ with $F = 8.1 \times 10^{-5}$ (see figure 6.6). For a complete list of computational parameters, see appendix C.

	λ_x
computation [m]	0.0241
experiments [m]	0.0249

Table 6.4 Wavelength comparison of computation with experiments at $F = 8.1 \times 10^{-5}$.
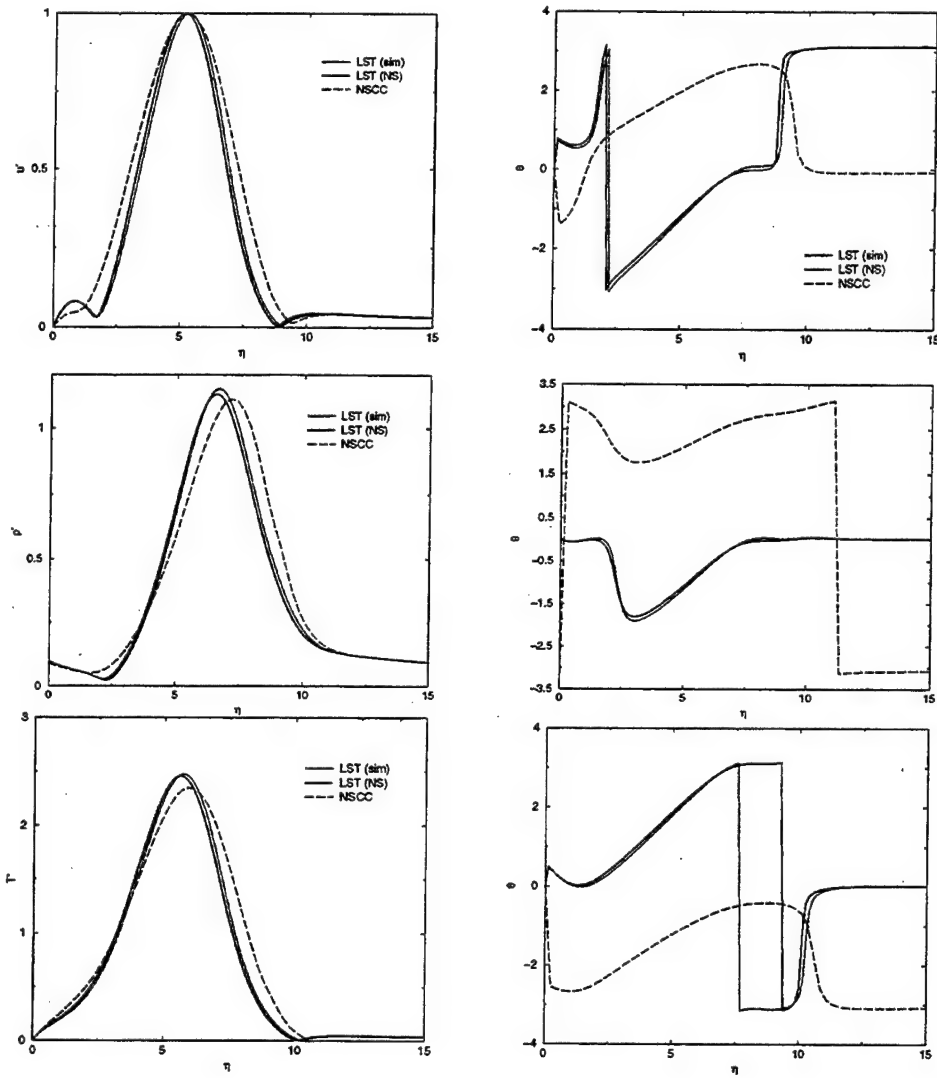
Figure 6.12 Comparison of amplitude (left) and phase (right) distribution of the computation to LST based on the similarity and the Navier–Stokes solution; ahown are u-velocity (top), density (center) and temperature (bottom); $F = 5 \times 10^{-5}$, $R_x = 700$.

Comparison with Experiments

As above, the TS–wavelength (table 6.4) is used to confirm the generation of the same kind of disturbances as in the experiments. The good agreement verifies the capturing of the right disturbance frequency and assures that no sound-wave or numerical noise is amplified to the order of the wave under
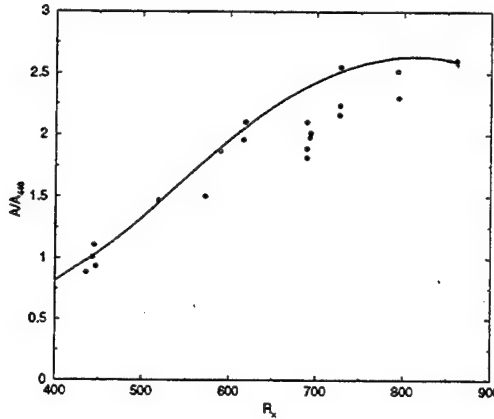
Figure 6.13 Amplitude distribution comparison of experiment with computation for $F = 8.1 \times 10^{-5}$ $(f^* = 17,000 Hz)$.

investigation. The amplification rate in figure 6.10 (right) for the computations is about 10% larger than Graziosi (1999) found in his experiments. Taking the uncertainty of supersonic experiments into account, the computations match the experiments reasonably well. In figure 6.13, the amplitude distribution in downstream direction is shown. The overall agreement is remarkable. Farther downstream, the computation shows a higher amplitude than the experiments. This could again be due to nonlinear interaction which is avoided in the computation.
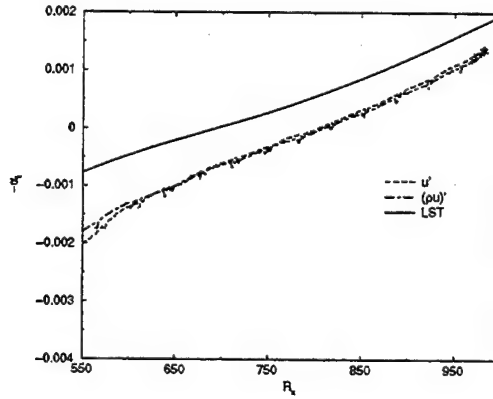
Figure 6.14 Amplification rate comparison of u' and $\rho u'$ with LST for $F = 8.1 \times 10^{-5}$ $(f^* = 17,000 Hz)$.
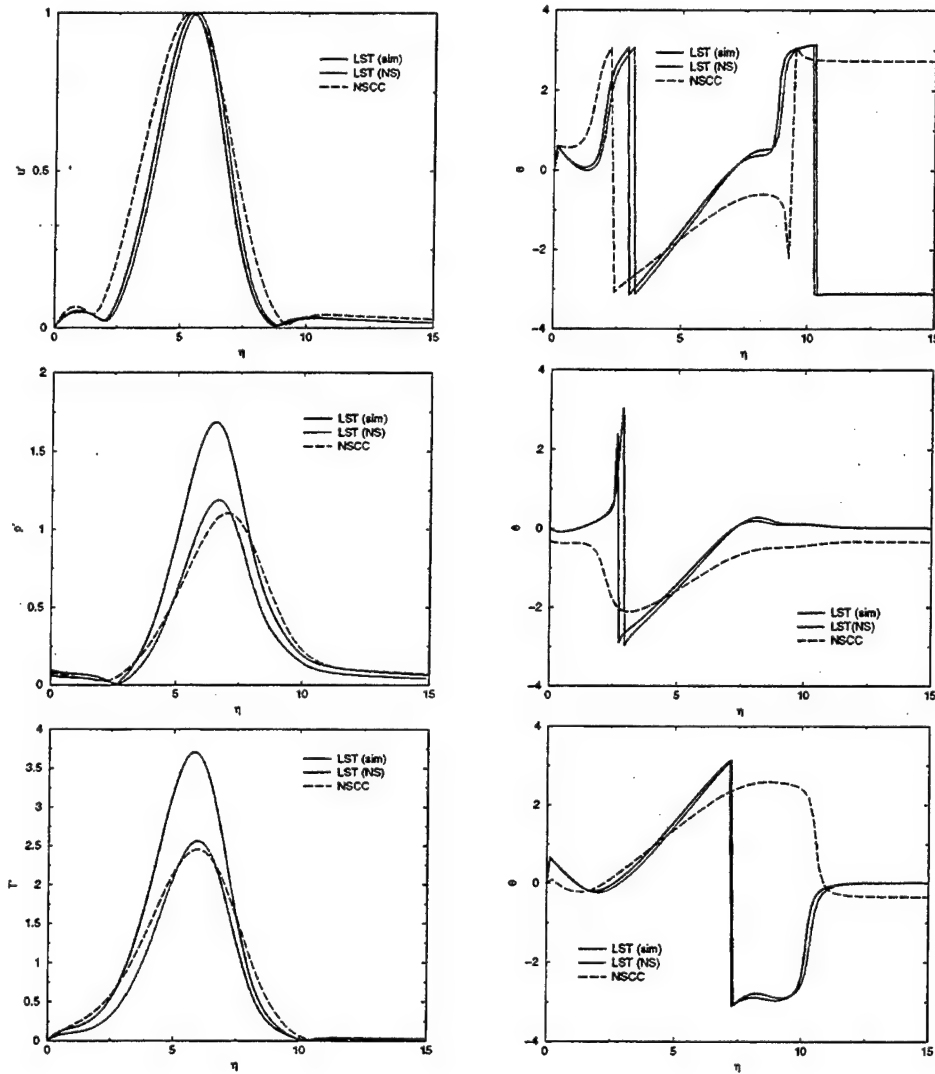
Figure 6.15 Comparison of amplitude (left) and phase (right) distribution of the computation to LST based on the similarity and the Navier–Stokes solution; ahown are u-velocity (top), density (center) and temperature (bottom); $F = 8.1 \times 10^{-5}$, $R_x = 700$.

Comparison with LST

Although only small disturbances of v' are introduced, the larger amplification rate and the shift of the instability region farther downstream are significant (see figure 6.14). For detailed discussion see § 6.2.4. Looking at the amplitude distribution in figure 6.15, the LST based on the similar-

ity solution overestimates the temperature and density amplitude, while the eigenfunctions of the computations are closer to the eigenfunctions computed with the Navier–Stokes solution. Because the differences between the baseflows obtained using the similarity and Navier–Stokes solutions are small (see § 6.1.1), it is unclear what causes the large deviation in the ρ'- and T'-eigenfunction of the LST similarity solution. The phase distribution of the computation shows the same properties than the LST-phase distributions, for both the similarity and the Navier–Stokes baseflow.

6.2.4   Non-Parallel Effects

The growth of the boundary-layer in the downstream direction causes a change in the wavenumbers of the downstream traveling TS-waves. This effect is not included in the investigations employing linear stability theory. For LST, a "parallel flow assumption" is used which inherently assumes that the baseflow cannot change in the downstream direction. In the following, we will investigate how the growth of the boundary layer changes the region of instability, i.e., whether it moves the start (branch I of the neutral curve in a linear stability diagram) and the end (branch II) of the unstable region.

6.2.4.1   Investigation of Branch I

In § 6.2.1, the simulation with frequency $F = 1.4 \times 10^{-5}$ was carried out such that the generated TS-wave crosses branch I. However, due to the fact that the space between the end of the disturbance slot and the beginning of the unstable region is only $\lambda_x/2$ in downstream direction, the TS–wave was not fully developed when entering the unstable region. Nevertheless, the amplitude comparison of figure 6.8 suggests that an increased unstable region for branch I may exist due to non-parallel effects of the compressible boundary layer. This is corroborated by the experiments where the amplitude growth is significant enough to exceed any error in the measurements.

6.2.4.2   Investigation of Branch II

To determine the increase of the unstable region near branch II due to non-parallel effects, four frequencies are considered:

- $F = 5 \times 10^{-5}$, from $R_x = 700$ to $R_x = 1450$

- $F = 8.1 \times 10^{-5}$, from $R_x = 400$ to $R_x = 1000$

- $F = 1.5 \times 10^{-4}$, from $R_x = 100$ to $R_x = 650$

- $F = 2 \times 10^{-4}$, from $R_x = 100$ to $R_x = 550$

For a detailed description of the two lower frequencies, see § 6.2.2 and § 6.2.3, where the lowest frequency is shifted downstream to cross the neutral curve at branch II. The two higher frequencies are chosen to investigate the non-parallel effects on high-frequency disturbances. Detailed listings of used parameters can be found in appendix C.

In the incompressible case, the best criterion for the unstable region of the stability diagram is the inner maximum of u' (Fasel & Konzelmann, 1990). Here, the second maximum of a given parameter is chosen, because the second maximum is much larger than the first maximum for the compressible eigenfunction. In this study, different criteria are presented to determine non-parallel effects, but no conclusion is drawn on how non-parallel effects are measured, i.e., how the downshift of the neutral point is related to non-parallel effects. Generally, the following quantities are investigated:

- streamwise velocity u'

- wall-normal velocity v'

- density ρ'

- temperature T'

- pressure p'

- spanwise vorticity ω_z'

- disturbance mass flux in streamwise direction $\rho u'$

Independent of the frequency, the parameters u', ρ', T' and $\rho u'$ are all amplified in the same manner while v', p' and ω_z' show different behavior. To ensure that the downshift is not governed by the influence of a pressure-gradient in the simulation, the neutral curve of the LST based on the Navier–Stokes solution is also computed. The Navier–Stokes solution has a smaller unstable region compared to the LST governed by the similarity solution which is consistent with a favorable pressure-gradient. This results in an even farther downshift of the neutral point which seems to be accurate since the computation captures the experimental results very well.

The long-wavelength oscillations in ρ' indicate that sound waves overlay the amplification rate. These oscillations also influence $\rho u'$ and T'. The small oscillations are introduced by the post-processing. Therefore, the amplification rates are averaged to obtain the neutral point.

Frequency $F = 5 \times 10^{-5}$

The lowest frequency is closest to the neutral curve computed with LST leading to the conclusion that the non-parallel effects are less pronounced. Looking at u', ρ', T' and $\rho u'$ the neutral point in figure 6.16 (left) is shifted from $R_x = 1220$ to $R_x = 1270$, that is a difference of $\Delta R_x = 50$ or 1.5 λ_x compared to the LST results employing the similarity solution as baseflow. Compared to the LST using the Navier–Stokes baseflow, the shift is from $R_x = 1025$ to $R_x = 1270$ or 6.8 λ_x. The v'-amplification rate and the LST similarity solution are the same so that non-parallel effects could not be determined, but the downshift compared to the LST with Navier–Stokes baseflow is from $R_x = 1025$ to $R_x = 1220$ (5.3 λ_x). The v'-amplification rate also takes much longer before it is fully developed. Even worse is the p'-amplification rate which gives the smallest difference to the LST with Navier–Stokes baseflow, i.e., a downshift to $R_x = 1140$ or a difference of three λ_x (this point may still vary because of the late development).
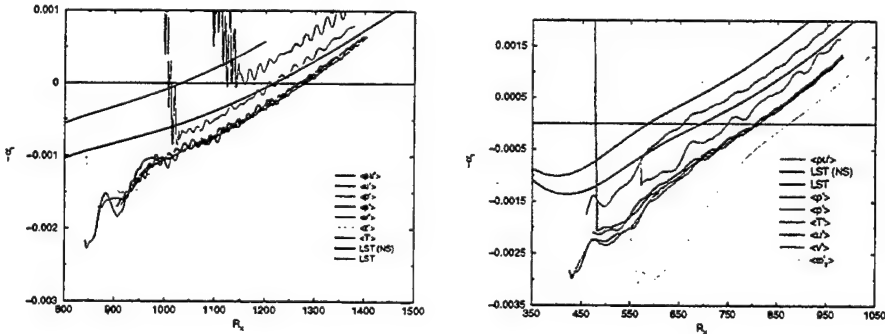
Figure 6.16 Amplification rate for different reference quantities; $F = 5 \times 10^{-5}$ (left) and $F = 8.1 \times 10^{-5}$ (right).

Frequency $F = 8.1 \times 10^{-5}$

For the frequency of $f^* = 17,000 Hz$ (see figure 6.16, right), the instability region is shifted about $\Delta R_x = 105$ (from $R_x = 700$ to $R_x = 805$) or 3 λ_x downstream if the u'-amplification rate and equivalent parameters are compared to the LST similarity solution. Compared to the LST Navier–Stokes solution, the shift is from $R_x = 600$ to $R_x = 805$ (5.3 λ_x). Looking at the v'-amplification rate, the shift is less than for the latter parameters, i.e. the shift is about $\Delta R_x = 50$ and $\Delta R_x = 150$ compared to the LST similarity solution and to the LST Navier–Stokes solution respectively. A relationship between the development of the v' and the ω_z'-amplification rate is clearly

visible–once the v'-amplification has developed, the vorticity amplification rate is getting smaller until it is parallel to the other amplification rate curves. The same mechanism can be seen for all frequencies under investigation, although it is not this obvious. For the frequency of $F = 8.1 \times 10^{-5}$, the ω'_z-amplification stays also different to the u'-amplification rate curve while for the other frequencies it approaches the same values due to this mechanism. The pressure is again less amplified than the LST similarity solution predicts and has therefore the smallest downshift to $R_x = 655$ ($1.5\ \lambda_x$) compared to the LST Navier–Stokes solution.

Frequency $F = 1.5 \times 10^{-4}$

Unfortunately, the second highest frequency shows some slight oscillations around the neutral point so that no precise location can be specified (see figure 6.17, left). Figure 6.17 (left) also shows that these oscillations are not produced by a reflected expansion fan as experienced for the grid convergence study in appendix B.1.1, since the oscillations appear with the same severity at the same location independent of the domain height. It is more likely that they are caused by a numerical error when the amplitude is close to zero during the post-processing procedure. Computations at a lower frequency do not show this behavior because of the higher amplification rate. Nonetheless, the amplitude distribution over the flow field (see figure 6.17,
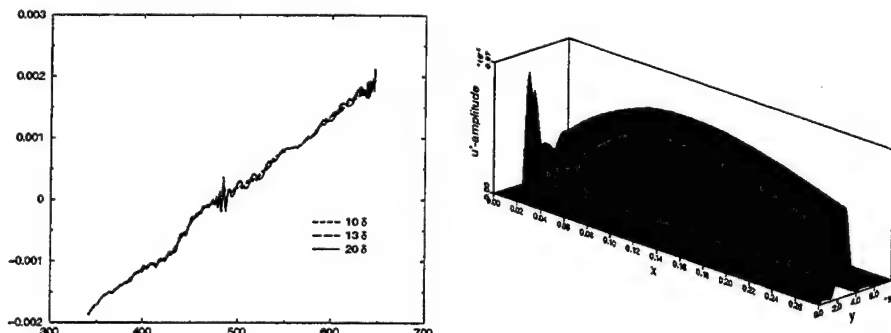
Figure 6.17 Amplification rates for different domain heights (left) and amplitude distribution of u' (right); $F = 1.5 \times 10^{-4}$ ($f^* = 31{,}250 Hz$).

right) is smooth so that the physical properties of the flow are captured correctly. The comparison to LST is done with a domain height of 20 boundary layer thicknesses. Considering u' and the equivalent parameters as criterion to determine non-parallel effects, the region of the neutral point in figure 6.18 (left) lies therefore between $R_x = 465$ and $R_x = 500$ revealing an enormous

shift downstream compared to $R_x = 350$ from the LST similarity solution. The maximum amplitude distribution leads to the conclusion that the neutral point is considered to be at $R_x = 480$ (see figure 6.19, left). The overall shift is therefore $\Delta R_x = 130$ or $3\ \lambda_x$. The difference between the LST similarity solution and LST Navier–Stokes solution is only $\Delta R_x = 40$ so that the difference between the u'-amplification rate and the LST Navier–Stokes solution is about $\Delta R_x = 170$ $(4\ l_x)$. The v'-amplification rate is closer the u'-amplification rate curve than for the lower frequencies leading to the conclusion that the non-parallel effects are stronger for v' than for the smaller frequencies. Considering v' as criterion to determine non-parallel effects results in a downshift of $\Delta R_x = 90$ $(2\ \lambda_x)$ or $\Delta R_x = 130$ $(2.5\ \lambda_x)$ for the comparison with the LST employing the similarity solution and Navier–Stokes baseflow, respectively. The pressure amplification rate develops too late to determine the neutral point, but because of the difference to the other amplification rates farther downstream, it is considered to give the best agreement with the LST using the Navier–Stokes baseflow.
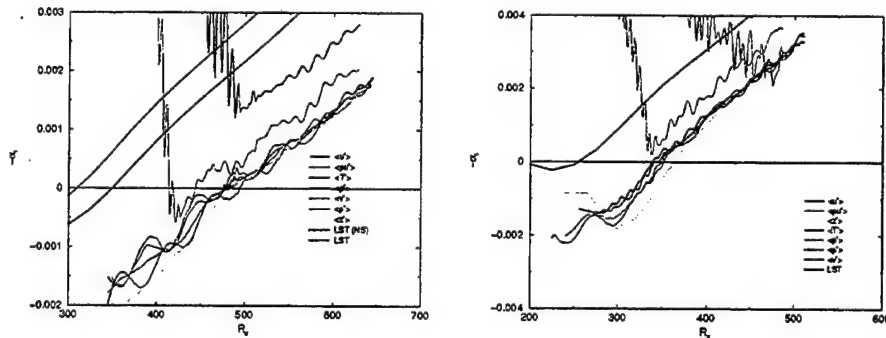
Figure 6.18 Amplification rate for different reference quantities; $F = 1.5 \times 10^{-4}$ (left) and $F = 2 \times 10^{-4}$ (right).

Frequency $F = 2 \times 10^{-4}$

Figure 6.18 (right) shows that for this frequency the Navier–Stokes solution is already stable according to LST. Looking at the amplitude distribution of u' in figure 6.19 (right), the neutral point is at about $R_x = 345$. The resulting shift of the neutral point downstream, as shown in figure 6.18 (right), is about $R_x \simeq 100$ or $2.5\ \lambda_x$ compared to the LST similarity solution where the neutral point is at $R_x = 250$. Because of the later development of the v' and p'-amplification rate no data to determine the neutral point can be extracted. Taking the ω_z'-amplification rate into account the the neutral point is slightly
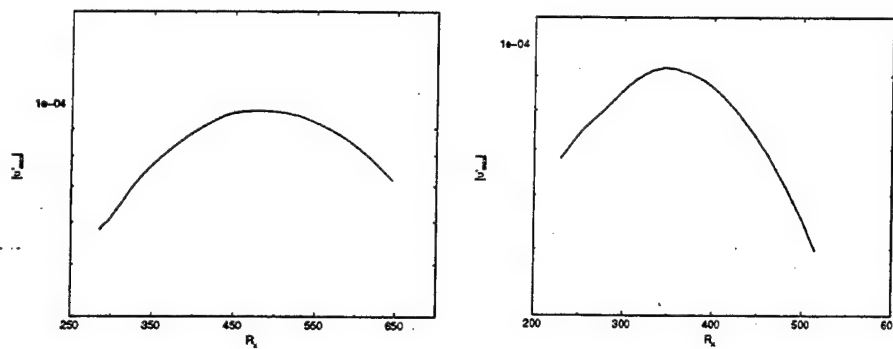
Figure 6.19 Maximum amplitude distribution of u'; $F = 1.5 \times 10^{-4}$ (left) and $F = 2 \times 10^{-4}$ (right).

farther downstream, namely at $R_x = 360$.

6.2.4.3 Summary of Observed Non-Parallel Effects

Non-parallel effects are most likely present for the flat plate boundary layer at $Ma = 3$. Because the experiments experience effects that agree qualitatively with the computations, it is unlikely that the downshift is caused by a numerical effect. But the far downstream shift of the neutral point for u', ρ', T' and $\rho u'$ is not only governed by non-parallel effects. This tremendous shift may be explained by an interaction of a higher mode which is for this Reynolds and Mach number not yet unstable (otherwise it would be present in the LST–diagram). Figure 6.6 shows an upcoming second mode for a 2D disturbance.
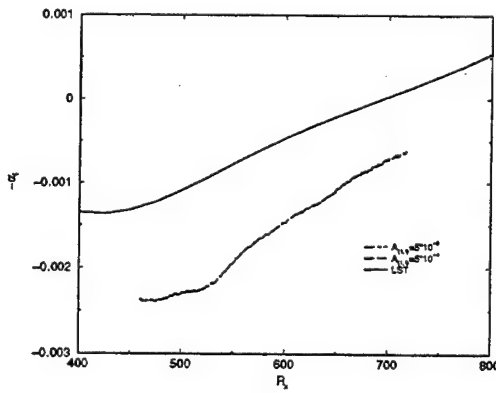
Figure 6.20 Verification of linear disturbance assumption.

Another reason could be the resolution in the spanwise direction so that, although linear disturbances are introduced, the energy wants to shift to

higher modes. To check that the introduced perturbations are small enough and, consequently, the linearity assumption holds, the already small forcing amplitude is reduced by a factor of 100 (see figure 6.20). The perfect alignment of the curves demonstrates that the disturbances behave linearly and the comparison with LST is valid. Therefore, the spanwise resolution is not considered to influence the stability behavior.

The good agreement between the v'-amplification rate and the LST similarity solution is remarkable leading to the conclusion that the other mechanism influencing the stability behavior, whatever that mechanism is, has less influence on the v'-velocity. Nonetheless, the downshift compared to the LST Navier–Stokes solution is remarkably large.
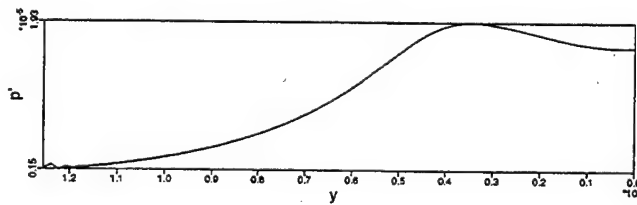
Figure 6.21 Pressure eigenfunction at $R_x = 940$.

Without proof, the p'-amplification rate compared to the LST with Navier-Stokes baseflow is probably best suitable to determine non-parallel effects. Mack categorizes the modes by the zero crossings of the pressure eigenfunction (Mack, 1984). Because no zero crossing is visible in the computations (see figure 6.21), the pressure distribution is associated with the first mode, i.e., the TS-mode. Therefore, it is less likely that higher modes are influencing the amplification of the pressure disturbances.
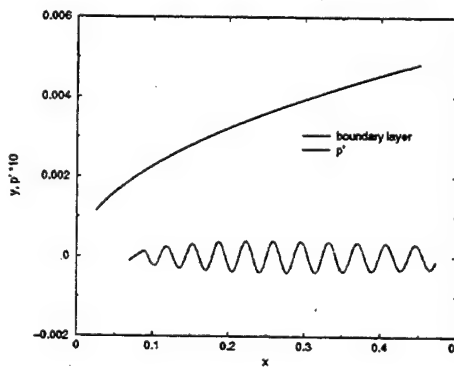
Figure 6.22 Boundary layer growth and development of p'-wave over x.

This study shows that independent of the criterion, non-parallel effects are much stronger than in the incompressible case (c.f. Fasel & Konzelmann,

1990). To demonstrate that the result is still plausible, figure 6.22 shows the boundary layer growth over the x-direction in comparison to the development of the wall pressure disturbance wave. The fast growing boundary layer and, consequently, the increasing v-velocity indicate that the assumption of a locally parallel flow used in LST is not necessarily fulfilled for the current investigation.

6.3 Nonlinear Resonances

6.3.1 Classical Fundamental Resonance
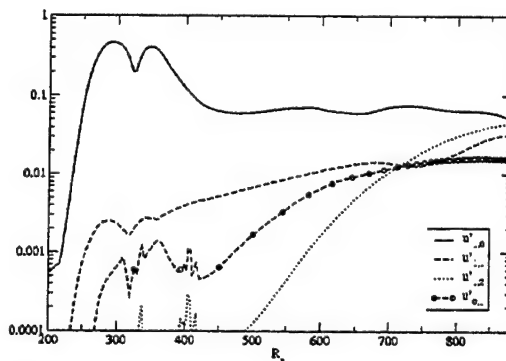
Figure 6.23 Fundamental Breakdown. Amplitude distribution of u-perturbation versus downstream direction. $Re = 10^5$, $F = 5 \times 10^{-5}$, $\Psi_{1,1} = 60°$.

Known from incompressible investigations the fundamental and subharmonic resonances are both strong mechanisms to transition. Now for the supersonic boundary layer, our simulations should shed some light on the question if they are also a relevant mechanism for $Ma = 3$. Several computations were conducted to reproduce a fundamental and subharmonic resonance. These simulations indicated that the largest secondary growth rate occurs between a two-dimensional disturbance and a disturbance with the wave angle close to the one associated with the linearly most amplified wave.

For a fundamental resonance to take place within the computational domain, the "classical" fundamental breakdown needs a disturbance amplitude of 10% of the free-stream velocity (see figure 6.23). Due to these large amplitudes, the fundamental breakdown does not seem to play an important role for $Ma = 3$ transition. It is to the authors opinion that the high amplitudes levels are necessary because of the small linear amplification of two-dimensional first and second mode waves (c.f. figure 6.6). An APG only weakly influences
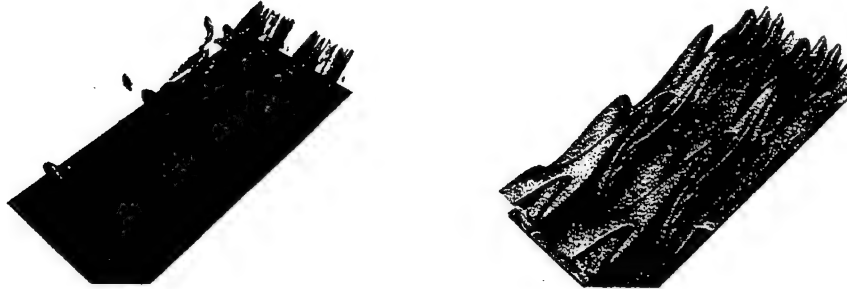
Figure 6.24 Isosurface of Q-criterion $Q = 2$ (left) and spanwise vorticity $\omega_z = 15$ (right) for a classical fundamental resonance; $Re = 10^5$, $R_x = 740 - 895$, $F = 5 \times 10^{-5}$, $\Psi_{1,1} = 60°$.

the growth rates of a two-dimensional wave whereas waves with a wave angle unequal to zero are strongly amplified. Since the resonance mechanisms of a fundamental or a subharmonic resonance is dependent on the amplitude of the primary wave and not on the amplitude of the secondary wave, an APG does not enhance the "classical" fundamental or subharmonic breakdown scenarios.

Figure 6.24b shows the lambda leg formation typically associated with this breakdown. The stretching of the peak stations can be observed in the spanwise vorticity isosurface plot (see figure 6.24c). Smaller amplitudes ($\leq 1\%$ of the free-stream velocity) of the primary $(1, 0)$-wave show no fundamental resonance within the computational domain so that then an oblique breakdown occurs.

6.3.2   Classical Subharmonic Resonance

While Thumm (1991) was able to find a weak subharmonic resonance for $Ma = 1.6$, Bestek & Eissler (1996) could not successfully find it for $Ma = 4.8$. At $Ma = 3$, there has been no indication of a subharmonic resonance with a fundamental 2D wave in our simulations.

6.3.3   Oblique Fundamental Resonance

To find a breakdown scenario which might be at least as viable as the oblique breakdown, we realized that a fundamental resonance between two three-dimensional waves is possible. A first hint was provided in the "classical" fundamental (Klebanoff-type) breakdown where the $(1, \pm 2)$-waves are strongly amplified (c.f. figure 6.23).
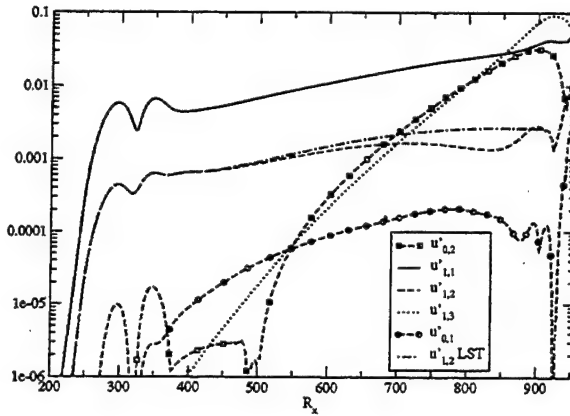
Figure 6.25 Oblique fundamental resonance: Amplitude distribution of u-pertubation versus downstream direction. $Re = 10^5$, $F = 5 \times 10^{-5}$, $\Psi_{1,1} = 60°$, $\Psi_{1,2} = 74°$.

Therefore, $(1, \pm 1)$ primary disturbance waves (amplitudes $\leq 0.06\%$ of the free-stream velocity) and $(1, \pm 2)$ secondary disturbance waves (amplitudes $\leq 0.005\%$ of the free-stream velocity) are combined for this breakdown scenario. Since the frequency ($F = 5 \times 10^{-5}$) is the same for both the primary and secondary waves, we call this an "oblique fundamental resonance". The wave angles were chosen to be $60°$ and $74°$ for the primary and secondary waves, respectively. So far, for the parameters tested, we found that the oblique fundamental resonance in comparison with the "classical" oblique breakdown is not an as strong mechanism.

Although figure 6.25 shows a deviation from the linear behavior of the secondary wave, the amplitude stays about 15 times smaller than the primary wave. Also the nonlinearly generated steady $(0, 1)$-vortex rises to the same amplitude level as the secondary wave, while the $(0, 2)$- and $(1, 3)$-modes, associated with a "classical" oblique breakdown amplify to the order of the primary wave. Because the flow structures shown in figures 6.26a and 6.26b resemble the ones of an oblique breakdown, we believe that in spite of the resonance of the secondary wave, the "classical" oblique breakdown is the superior mechanism.

6.3.4   Oblique Subharmonic Resonance

Three different combinations of an oblique primary disturbance with an oblique secondary disturbance with half the frequency of the primary wave are possible. Kosinov & Tumin (1996) concluded that a subharmonic resonance of two three-dimensional waves might play an important role in super-
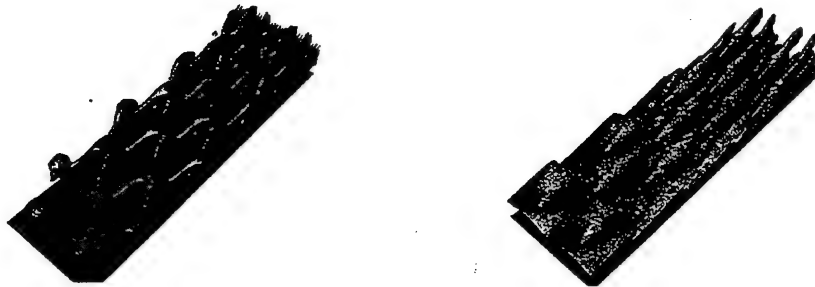
Figure 6.26 Isosurface of Q-criterion $Q = 0.2$ (left) and spanwise vorticity $\omega_z = 15$ (right) for a oblique fundamental resonance; $Re = 10^5$, $R_x = 705 - 925$, $F = 5 \times 10^{-5}$, $\Psi_{1,1} = 60°$.

	Primary wave		Secondary wave	
	frequency	wave angle	frequency	wave angle
case I	$F_{2,2} = 5 \times 10^{-5}$	$\Psi_{2,2} = 60°$	$F_{1,1} = 2.5 \times 10^{-5}$	$\Psi_{1,1} = 60°$
case II	$F_{2,1} = 5 \times 10^{-5}$	$\Psi_{2,1} = 60°$	$F_{1,2} = 2.5 \times 10^{-5}$	$\Psi_{1,2} = 82°$
case III	$F_{2,1} = 5 \times 10^{-5}$	$\Psi_{2,1} = 60°$	$F_{1,1} = 2.5 \times 10^{-5}$	$\Psi_{1,1} = 74°$

Table 6.5 Oblique Subharmonic Breakdown. Overview of studied cases.

sonic boundary transition based on their experimental findings at $Ma = 2$. Their numerical and theoretical work confirmed a possible resonance between a primary $(2,1)$-wave with secondary $(1,-2)$- and $(1,1)$-waves. In addition, primary $(2,2)$- and secondary $(1,1)$-waves can both travel with the same wave angle. To distinguish these subharmonic resonances from the "classical" one which involves a two dimensional primary and oblique secondary disturbance, we call this breakdown "oblique subharmonic resonance".

For our investigations for a Mach 3 boundary layer, three different cases were computed (see Table 6.5). First, the primary disturbances $(2, \pm 2)$ are excited with an amplitude of 0.3% (of the free-stream velocity), and the secondary disturbances $(1, \pm 1)$ have an amplitude of 0.005%. Thus both primary and secondary waves have the same wave angle of $\Psi = 60°$. For case II and case III, secondary waves of different wave angles are combined with a primary wave $(2, \pm 1)$ ($\Psi_{2,1} = 60°$, amplitude of 0.1%). For case II, the secondary waves are $(1, \pm 2)$-modes with $\Psi_{1,2} = 82°$ and also disturbed with an amplitude of 0.005%. For case III, the secondary disturbances are $(1, \pm 1)$-modes with an amplitude of 0.005% and $\Psi_{1,1} = 74°$. The primary disturbance amplitude in case I is three times higher than in the other two cases to see at least a small deviation from the linear eigen-behavior of the secondary wave.
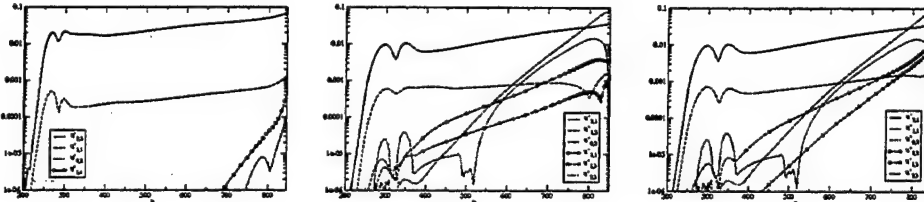
Figure 6.27 Oblique subharmonic resonance: Amplitude distribution of u-perturbation versus downstream direction for cases I, II and III from left to right, respectively; $Re = 10^5$, $F_{2,x} = 5 \times 10^{-5}$, $F_{1,x} = 2.5 \times 10^{-5}$, $\Psi_{2,x} = 60°$.
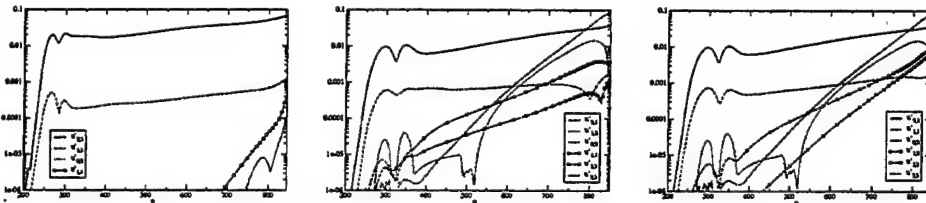
Figure 6.28 Oblique subharmonic resonance: Isosurface of Q-criterion for cases I ($Q = 3$), II ($Q = 0.2$) and III ($Q = 0.2$) from left to right, respectively; $Re = 10^5$, $F_{2,x} = 5 \times 10^{-5}$, $F_{1,x} = 2.5 \times 10^{-5}$, $\Psi_{2,x} = 60°$

But, as can be seen in figure 6.27a, the nonlinear generation of higher modes is still not emphasized. However, the amplification curves of figures 6.27b and 6.27c clearly indicate that strong nonlinear interaction can occur indicating that oblique subharmonic breakdown mechanisms may be relevant for the Mach 3 boundary layer. Surprisingly, the oblique subharmonic breakdown produces a more rapid amplitude growth in the downstream direction at lower amplitudes if the primary and the secondary waves are forced with different wave angles than if primary and secondary waves have the same wave angle (c.f. figure 6.27a with figures 6.27b and 6.27c). This is an indication that the wave angle between primary and secondary waves plays an important role for energy transfer from the base flow to the disturbance waves and between primary and secondary waves. In case II, where the secondary wave is mode $(1,2)$, the nonlinearly generated $(1,1)$-wave also shows some nonlinear resonance slightly downstream of the resonance location of the $(1,2)$-wave. But in case III, where the forced $(1,1)$-wave shows resonance about the same location as in case II, the generated $(1,2)$-wave reveals no nonlinear resonance.

The structures in figures 6.28a, 6.28b and 6.28c all strongly resemble the
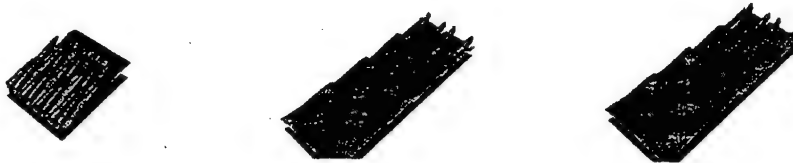
Figure 6.29 Oblique subharmonic resonance: Isosurface of spanwise vorticity $\omega_z = 15$ for cases I, II and III from left to right, respectively; $Re = 10^5$, $F_{2,x} = 5 \times 10^{-5}$, $F_{1,x} = 2.5 \times 10^{-5}$, $\Psi_{2,x} = 60°$

structures found in an oblique breakdown (see figure 6.40 in § 6.4). For the simulations with different wave angles (case II and case III), the spanwise vorticity (ω_z) exhibits an additional "tongue" in-between the two main structures (see figures 6.29b and 6.29c in comparison with figure 6.26c). Overall, it appears that similar mechanisms as for the "classical" oblique breakdown are present.

6.4 Oblique Breakdown

Thumm (1991) was the first who realized the importance of the oblique breakdown as a mechanism that could lead to turbulence. He described in detail the physics of the start up of the oblique breakdown. Until now it is still not clear if an oblique breakdown really leads to turbulence and if this mechanism plays a significant role in nature.
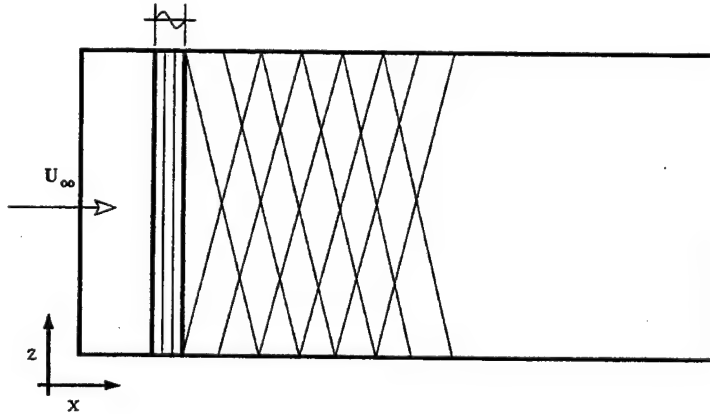

Figure 6.30 Wave front of the 3D waves in the computational domain.

What is oblique breakdown? According to Mack (1984), the Squire theorem, which states that the critical Reynolds number is defined by the location where 2D waves are amplified, is not valid for compressible flow. Instead, 3D waves are highly amplified and for a given Mach number there is a specific wave angle which leads to most amplified TS-waves. Oblique breakdown is caused by the nonlinear interaction of these 3D waves. In the numerical simulations presented in this work, the development of a 3D wave throughout the computational domain is simulated, similar to the § 6.2, but with higher amplitudes. Since the DNS code employs symmetric Fourier transforms in the spanwise direction, two 3D waves, with Ψ and $-\Psi$ as their wave angles, are excited simultaneously in the disturbance slot (figure 6.30). If the 3D waves reach large amplitudes farther downstream, they will start to interact with themselves and with each other. For a more detailed investigation the flow properties are decomposed using a Fourier-transform with respect to time and the spanwise direction:

$$\phi(x,y,z,t) = \sum_{h=-H}^{H} \sum_{k=-K}^{K} \hat{\phi}(x,y)e^{i(h\beta t + k\gamma z)}, \qquad (6.2)$$

where H is the number of Fourier modes in time and K in the z-direction. This formulation has the advantage that it can be used to show how higher modes in time and space are created by the nonlinear terms of the Navier–Stokes equations. For example,

$$u_j \cdot \frac{\partial u_i}{\partial x_j} \qquad (6.3)$$

creates terms like

$$e^{i(h_1\beta t + k_1\gamma z)} \cdot e^{i(h_2\beta t + k_2\gamma z)} = e^{i((h_1+h_2)\beta t + (k_1+k_2)\gamma z)}. \qquad (6.4)$$

Equation (6.4) indicates that the modes in time and in the z-direction of the interacting waves must be added to generate higher solutions. As an abbreviation equation (6.4) can also be written as

$$(h_1, k_1) + (h_2, k_2) = (h_1 + h_2, k_1 + k_2); \qquad (6.5)$$

where (h_1, k_1) indicates a mode combination with the frequency $h_1\beta$ and the spanwise wave number $k_1\gamma$. For a 3D wave with a frequency β and a wave number γ, h and k are equal to one. The wave, which is mirrored at the symmetry line of the domain, which is parallel to x and located in the middle of the spanwise direction, has $-\Psi$ as its wave angle and, consequently, $h = 1$ and $k = -1$. The possible mode combinations, that are created by these two

waves, are listed in table 6.6. The resulting waves exist in addition to the original waves and can also interact with them to produce even higher mode combinations like (1,3) or (4,0). An interesting consequence of the oblique breakdown is that mode combinations with odd modes in time have only odd modes in z and with even modes in time only even modes in z (Thumm, 1991).

$(h_1, k_1) + (h_2, k_2)$	$(h_1 + h_2, k_1 + k_2)$
$(1, 1) + (1, 1)$	$(2, 2)$
$(1, 1) + (1, -1)$	$(2, 0)$
$(1, 1) + (-1, 1)$	$(0, 2)$
$(1, 1) + (-1, -1)$	$(0, 0)$
$(1, -1) + (1, -1)$	$(2, -2)$
$(1, -1) + (-1, -1)$	$(0, -2)$
$(-1, 1) + (-1, 1)$	$(-2, 2)$
$(-1, 1) + (-1, -1)$	$(-2, 0)$
$(-1, -1) + (-1, -1)$	$(-2, -2)$

Table 6.6 Selected mode combinations of a (1,1) and (1,-1) wave-pair.
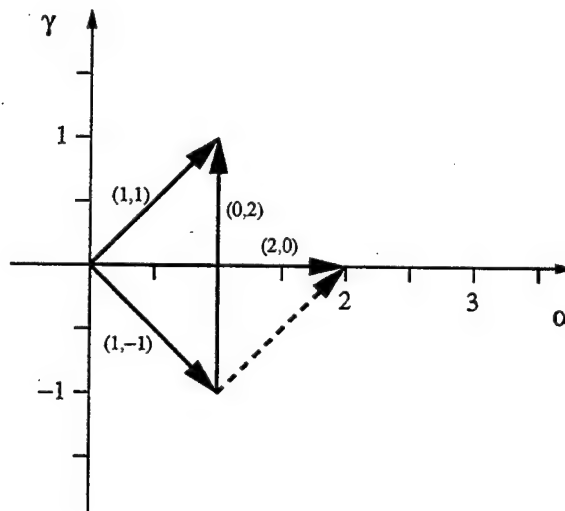
Figure 6.31 Wave number diagram for the mode combinations (1,1), (1,-1), (2,0) and (0,2).

The mode combinations can be plotted as vectors in a wave number diagram (figure 6.31). The generation of the higher mode combinations is equivalent to a vector summation or subtraction. In figure 6.31 two examples are

shown. Note that (1,1) and (1,-1) are the subharmonic mode combinations
of (2,0). However, there is no subharmonic resonance (staggered Λ-vortices)
since the 3D waves are linearly more amplified than the 2D wave. Thumm
(1991) observed that the mode combination (0,2) has the highest influence
on oblique breakdown in its start up.

It is of interest to see how a mode combination would look in physical space.
Since we are interested in vorticity waves, i.e., TS-waves, a wave ansatz is
introduced which has the form

$$\phi(x,y,z,t) = \hat{\phi}(y)e^{i(h\alpha x + k\gamma z + h\alpha c t)}. \tag{6.6}$$

If h is increased the wave will have a smaller wavelength (divided by h)
and if k is increased the wave will have a larger wave angle. ϕ represents a
arbitrary flow quantity, e.g., the u-velocity. An instantaneous plot of the u-
velocity of the wave at a specific y-location includes positions of the maximum
and minimum of the u-velocity. The positions of the maximum (minimum)
are repeated every wavelength as is illustrated in figure 6.32. The plot is
calculated with the real part of equation (6.6), but without amplification of
the waves. The values on the z-axis do not match any values obtained from
a DNS, since they are intended for visualization purposes only. Since the
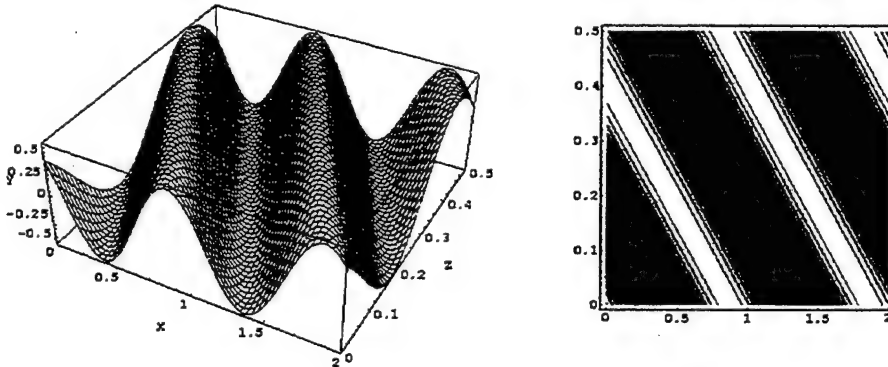
Figure 6.32 Example of a 3D wave traveling with the wave angle $\Psi = 65°$.

u-velocity vector is parallel to the flow direction, a wave in the u-velocity is
a longitudinal wave.

The interference of waves with the wave angle Ψ and $-\Psi$ is visualized in
figure 6.33. It represents a superposition of two 3D waves. The linear stage
of oblique breakdown should be dominated by such structures. They have a
shape similar to the letter "X" where the maxima are located in the center
and at the ends of the "X". Structures with a "X"-shape in the pressure
distribution were observed in preliminary simulations of the nonlinear stage

of oblique breakdown, and we will look for them in the results presented in the following sections. Before the results obtained by the DNS are discussed, attention is being devoted to the influence of the (0,2) and (0,4) mode combination on the "X"-shape. The (0,2) and the (0,4) are stationary distortions of the baseflow. Figures 6.34 and 6.35 illustrate how the distortion of the baseflow alters the "X"-Shape.
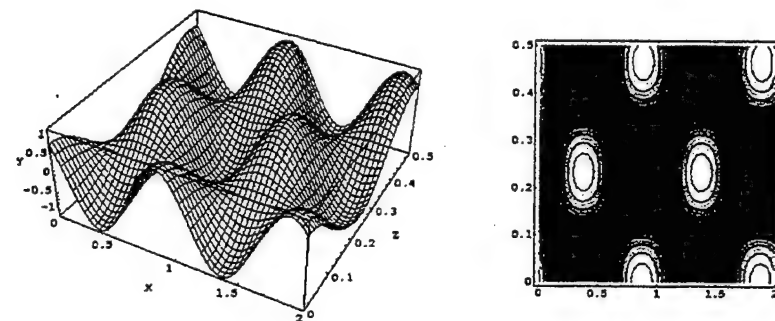
Figure 6.33 Interference of the mode combinations (1,1) and (1,-1).
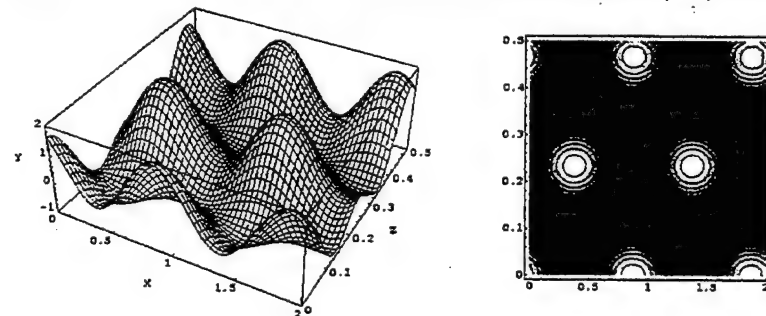
Figure 6.34 Influence of mode combination (0,2).
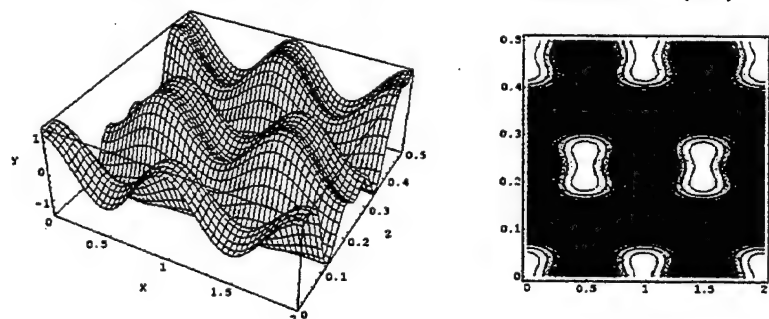
Figure 6.35 Influence of mode combination (0,4).

6.4.1 Without Pressure Gradient

All oblique breakdown calculations are conducted with the flow properties which were used for the supersonic validation cases in § 4.5. A detailed summary of the computational parameters for case OBLNP3, the simulation presented in this section, can be found in appendix C. The computational domain starts at $R_x = 750$ and ends at $R_x = 1438$. Disturbances with the amplitude $A_{1,1} = 0.003$ and angular frequency $F = 3 \times 10^{-5}$ are introduced into the computational domain between $R_x = 927$ and $R_x = 993$. The computational domain is four boundary layer thicknesses high. The buffer domain starts at $R_x = 1380$. At the location where the disturbances are introduced, the grid is equidistant in x and 22 points resolve one streamwise wavelength λ_x. Downstream of the disturbance slot, the grid is stretched until the position $R_x = 1365$. At this location Δx has such a value that 176 points resolve one streamwise wavelength λ_x. 55 modes are used in the spanwise direction. The resolution of the calculation is higher than the resolution of
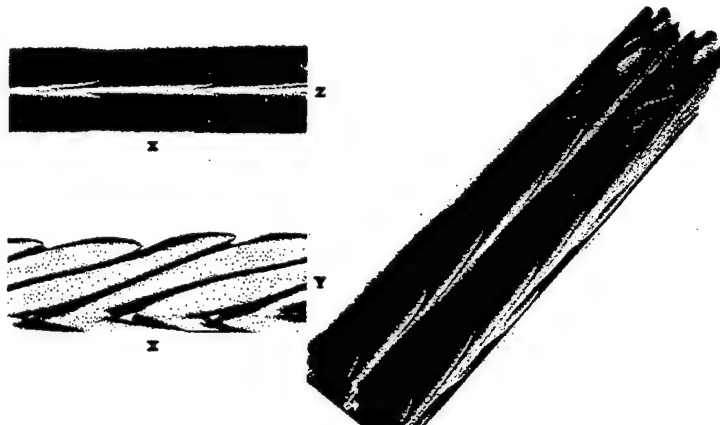
Figure 6.36 Isosurface of streamwise vorticity $|\omega_x| = 1$ between $R_x = 1085$ and $R_x = 1291$.

the simulations presented by Thumm (1991) and Eissler (1995). For that reason it is possible to compute deeper into transition and to investigate how new structures arise. Thumm (1991), in his work, discussed structures visualized by the streamwise vorticity ω_x which have the shape of tongues. The tongues split into two tips further downstream. Preliminary simulations carried out for the present research had shown that for higher Mach numbers the tips developed more strongly on one side. In figure 6.36 these structures are plotted for $|\omega_x| = 1$ between $R_x = 1085$ and $R_x = 1291$ for the simulation OBLNP3. The top view of figure 6.36 also shows the previously discussed "X"-shape. However, the structures do not really look like the predicted
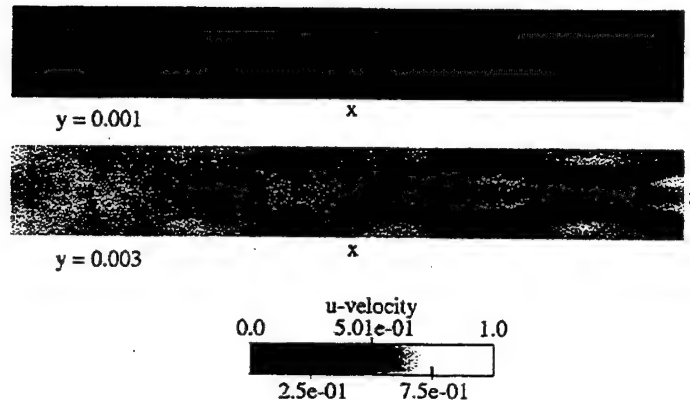
Figure 6.37 Contour of u-velocity between $R_x = 1085$ and $R_x = 1291$ at location $y = 0.001$ and $y = 003$.

shape shown in figure 6.33. For that reason, the u-velocity was checked whether there the "X-shape" appears. In figure 6.37 contours of the u-velocity at different y-locations in the boundary layer are plotted. At $y = 0.003$ the predicted "X"-shape is visible. Upstream, two parallel black lines are getting stronger which are caused by the (0,2) mode combination. It
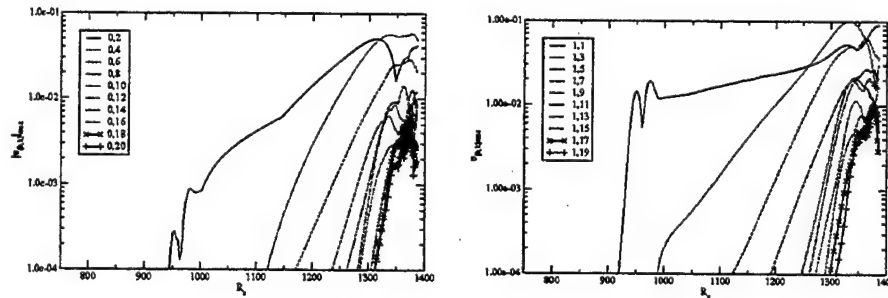
Figure 6.38 Distribution of $|u_{[0,k]}|_{max}$ (left) and $u_{[1,k]max}$ (right) versus R_x.

is very interesting that at a different y-location the contours look differently. At $y = 0.001$ the "X" is almost not visible anymore and only two parallel black lines (the (0,2) mode combination) dominate the velocity field. The explanation for that behavior can be found in the following two figures. The mode combinations (0,2) and (1,1) are strongly amplified and they have high amplitudes between $R_x = 1085$ and $R_x = 1291$ (figure 6.38). The amplitude distribution of these two mode combinations over y for different downstream
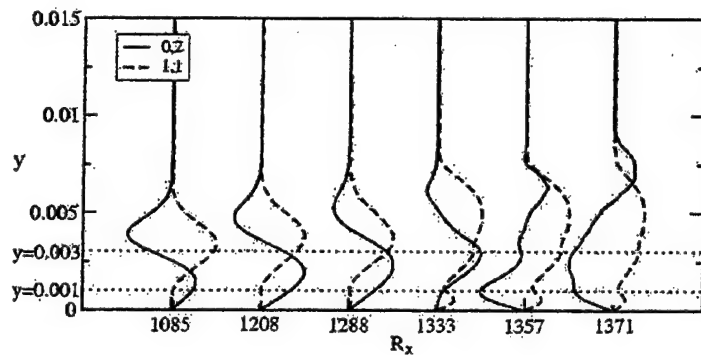
Figure 6.39 Development of the amplitude distribution of $u_{[h,k]}/u_{[h,k]max}$ over y.

locations is illustrated in figure 6.39. The maximum of the (1,1) is located at a different location than the maximum of the (0,2). This means that the mode combinations have a different influence for changing y locations. At $y = 0.001$ the (1,1) is very weak and that is why the (0,2) is strongly visible in figure 6.37. At $y = 0.003$ both modes are present. It is also of interest that the (0,2) mode combination is significantly changing in the downstream direction. Its maximum is shifted to higher values of y and the absolute value of the minimum is decreasing until position $R_x = 1357$ where the locations of the maximum and the minimum are inverted. Note that at $R_x = 1085$ the absolute value of the minimum is higher than the maximum. At position $R_x = 1208$ the maximum is higher than the absolute value of the minimum. For that reason there is a significant change in the slope of the amplitude distribution of the (0,2) at around $R_x = 1140$ in figure 6.38. The shift of the maximum to higher y-values is the explanation for the changing pattern of the u-velocity contour at location $y = 0.003$ (figure 6.37). Upstream, the flow is dominated by the "X"-shape. Farther downstream, the (0,2) is getting stronger because its amplitude value is changing from a negative to a positive value for higher local Reynolds numbers (until $R_x = 1357$).

The latter discussion emphasizes that in the u-velocity, the predicted "X"-shape can be found since the "X"-shape is caused by the mode combinations (1,1) and (1,-1). However, it is not clear if this is a dominant structure since in every quantity different patterns arise at different y-locations. A good identification of structures can be obtained by employing a vortex identification technique called Q-criterion. It is based on the vortex definition given by Chong et al. (1990). A vortex is located in a region in the flow field where the vorticity is sufficiently strong to cause the velocity gradient tensor to be dominated by the rotation tensor. That means mathematically that
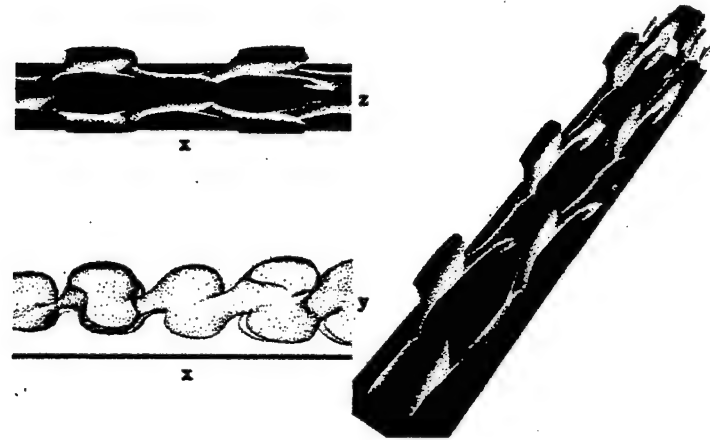
Figure 6.40 "X"-shape vortices identified by Q-criterion with $Q = 10$ between $R_x = 1085$ and $R_x = 1291$.
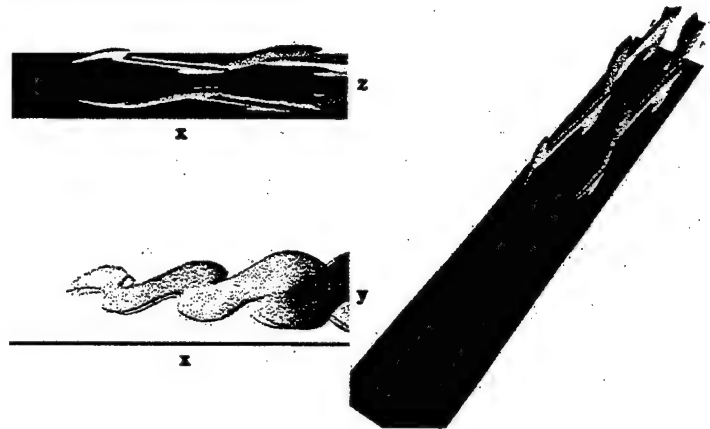
Figure 6.41 "X"-shape vortices identified by Q-criterion with $Q = 30$ between $R_x = 1085$ and $R_x = 1291$.

the magnitude of the symmetric part of the velocity gradient tensor, which describes the strain, is smaller than the asymmetric part that describes the rotation. Q identifies the difference between the magnitude of rotation and the magnitude of strain, so that

$$Q = \frac{1}{2}(W_{ij}W_{ij} - S_{ij}S_{ij}), \tag{6.7}$$

where W_{ij} indicates an element of the rotation tensor and S_{ij} an element of the strain tensor. For positive values of Q, rotation is stronger than strain. Note that equation (6.7) is an incompressible definition. For an incompressible flow, Q is invariant with respect to its reference frame. That

is not true for compressible flows. Nevertheless, it still defines locations where rotation dominates the flow field. If equation (6.7) is applied to the previously discussed flow field it visualizes structures presented in the figures 6.40 and 6.41. The Q-criterion confirms the "X"-shape.

Since the integration domain extended further downstream than at $R_x = 1291$, the deformation of the "X"-shape can·be investigated. Figures 6.38 and 6.39 already give an impression of what will happen further downstream. Higher mode combinations are gaining importance. The amplitude distribution in y of the (0,2) (figure 6.39) is significantly changing between $R_x = 1333$ and $R_x = 1357$. This is also connected with its amplitude distribution in x where its value is strongly decreasing downstream of $R_x = 1320$ (figure 6.39). The mode combination (0,4) has the highest value of all stationary mode combinations downstream of $R_x = 1300$. Its effect on the u-velocity is demonstrated in figure 6.42. The four bright lines parallel to the x-axis represent the four maxima of the (0,4). At the end of the domain six black lines are getting stronger which are the minima of the (0,6). A 3D view of
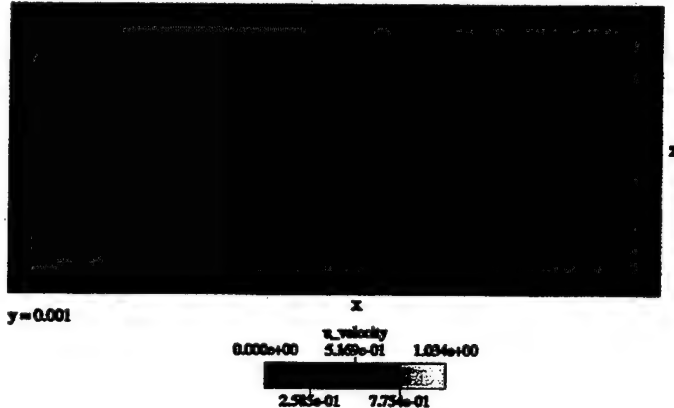
Figure 6.42 u-velocity at $y = 0.001$ between $R_x = 1333$ and $R_x = 1380$.

an isosurface of the u-velocity for the value $u = 0.65$ is given in figure 6.43. The previously discussed "X"-shape is visible. Further downstream, the legs of the "X" which are closer to the buffer domain are pushed away from the wall. This process clearly thickens the boundary layer (figure 6.44). Particles with high velocity are transported closer to the wall and particles with low velocity are pushed away from the wall. At the end of the domain in figure 6.43 new structures arise parallel to the x-axis at $z = \lambda_z/2$ (along the symmetry line). The Q-criterion confirms the new structure in figure 6.45. At the start of the buffer domain ($R_x = 1380$), the resolution becomes too coarse to resolve the small structures. Grid mesh due to the lack of resolution
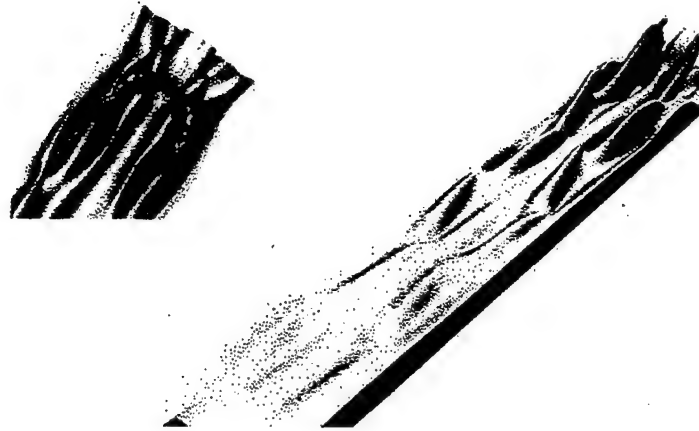
Figure 6.43 3D isosurface of the u-velocity with $u = 0.65$ between $R_x = 1208$ and $R_x = 1380$.
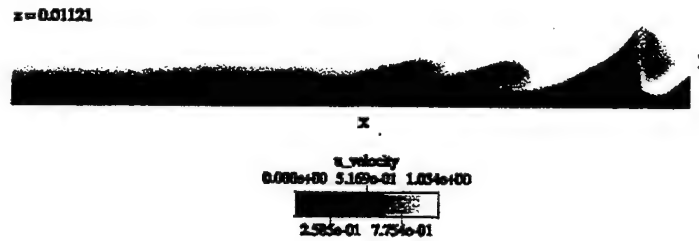
Figure 6.44 Contours of the u-velocity in the computational domain between $R_x = 1208$ and $R_x = 1380$ at $z = 0.273 \times \lambda_z$, the position where one leg of the "X" is pushed away from the wall.

occurs in the z-direction (figure 6.45). The influence of higher modes in time on the generation of the new structures is limited. Only the mode combinations (2,0), (2,2), (2,4) and (2,6) have high enough amplitudes (figure 6.46) to significantly alter the flow field.

6.4.2 With Adverse Pressure Gradient

In this section two simulations are compared, one with (case OBLPG) and one without pressure gradient (case OBLNP4). The computational domain and flow quantities are the same with the exception of the pressure gradient and the disturbance amplitude which is almost four times higher for the simulation without APG. The domain starts at $R_x = 1226$ and ends at $R_x = 1782$. Disturbances with the angular frequency of $F = 3 \times 10^{-5}$ are introduced into the domain through a blowing and suction slot located between
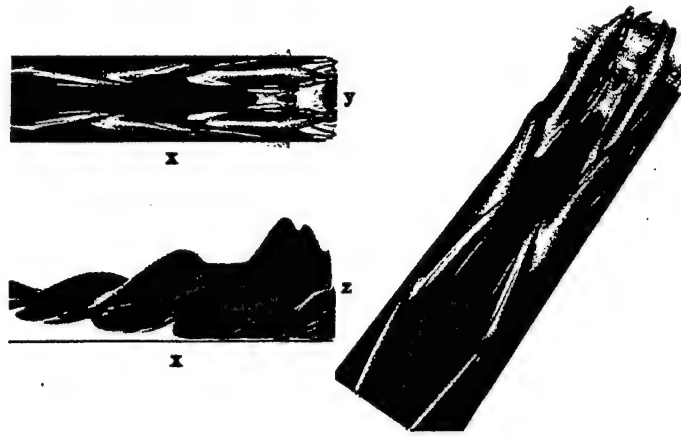
Figure 6.45 "New structures" between the legs of the "X"-Shape identified by the Q-criterion for $Q = 500$ between $R_x = 1333$ and $R_x = 1380$.
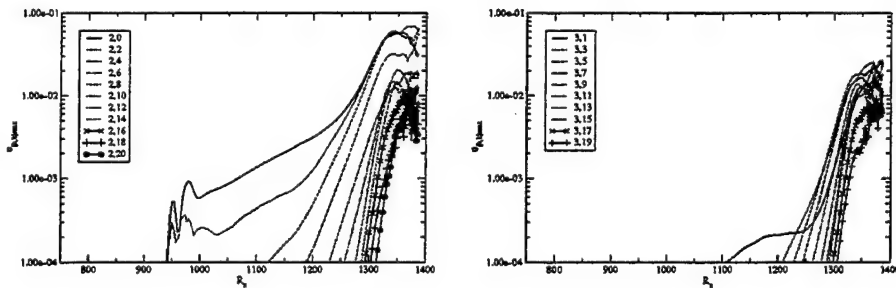
Figure 6.46 Distribution of $u_{[2,k]max}$ (left) and $u_{[3,k]max}$ (right) versus R_x.

$R_x = 1332$ and $R_x = 1369$. The buffer domain starts at $R_x = 1715$. The domain is about four boundary layer thicknesses high. The grid stretching starts downstream of the disturbance slot and ends at $R_x = 1657$. The ratio $\frac{\Delta x}{\Delta \hat{x}}$ is chosen in such way that 88 points are in one streamwise wavelength λ_x downstream of $R_x = 1657$. 16 modes are used to resolve the spanwise direction. With this low resolution only the start up of oblique breakdown with and without APG can be simulated. It was not possible to compute farther into transition and, therefore, to choose a higher resolution since the pressure distribution at the free-stream drifts from its desired value. This may well be the correct physical behavior; however, more investigations are required to prove this. The simulation OBLPG has a moderate APG. The distribution of the Hartree parameter β_H over R_x indicates an almost constant value of $\beta_H \approx -0.12$ (figure 6.47).
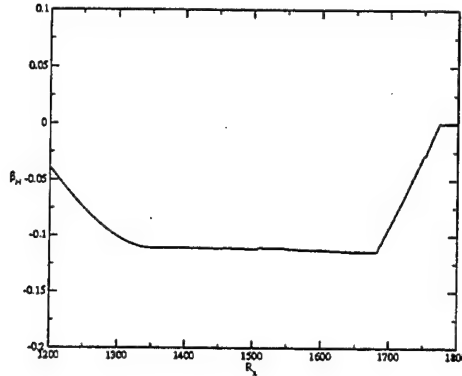
Figure 6.47 Distribution of Hartree parameter β_H versus R_x for case OBLNP4.
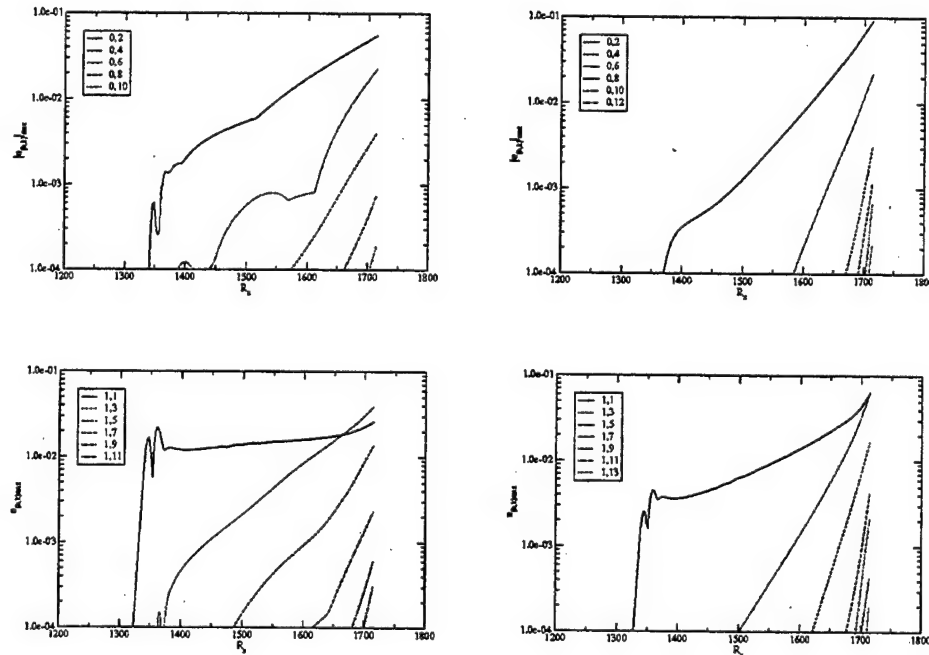
Figure 6.48 Distribution of $|u_{[0,k]}|_{max}$ (top) and $u_{[1,k]max}$ (bottom) versus R_x for cases OBLNP4 (no APG, left) and OBLPG (with APG, right).

The amplitude distributions of the individual mode combinations (h,k) versus R_x for both simulations are plotted in figure 6.48. All mode combinations (h,k) experience a much higher amplification for case OBLPG than for case OBLNP4. The APG has a strong impact on the amplification rate. For that

reason the disturbance amplitude in the suction and blowing slot has to be much smaller than for case OBLNP4, as mentioned earlier, otherwise the disturbance waves would reach much faster the nonlinear stage and the flow would start to transition further upstream. However, this is not desired since in both simulations the flow is required to transition shortly upstream of the buffer domain, so that the calculation can run stable and can converge out. The abrupt changes of the slope of the stationary mode combinations (0,2) and (0,4) in figure 6.48 (top left) can be explained in the same way like for figure 6.38. For example, the absolute value of the minimum (of the (0,2)) is at one R_x-location bigger and at another R_x smaller than the absolute value of the maximum (also of the (0,2)), so that at the position where it changes an abrupt switch in the slope of the amplitude distribution over R_x is visible. In the case OBLPG abrupt changes cannot be found in figure 6.48 (top right). However, they exist at lower amplitude levels and therefore at lower local Reynolds numbers. The mode combination (1,1) for case OBLNP4 is weakly amplified (figure 6.48, bottom left). The amplitude value of the (1,3) is increasing much faster than the amplitude value of the (1,1). For that reason, downstream of $R_x \approx 1650$ the (1,3) has a higher amplitude than the (1,1). For the case OBLPG, the (1,1) is strongly amplified and that is the reason why the (1,3) does not reach higher amplitude values than the (1,1) in the presented computational domain.
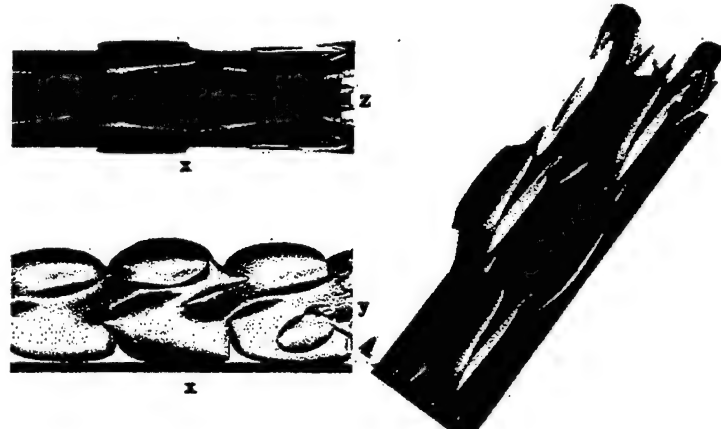
Figure 6.49 Isosurface of $Q = 2$ for case OBLNP4 between $R_x = 1644$ and $R_x = 1715$.

The structures which are identified by the Q-criterion look very similar to the structures obtained by simulation OBLNP3 (figure 6.49, 6.50, 6.51 and 6.52). The "X"-shape is dominant for both calculations. In the simulation OBLNP4, the maximum in the center of the "X" is divided in three parts and
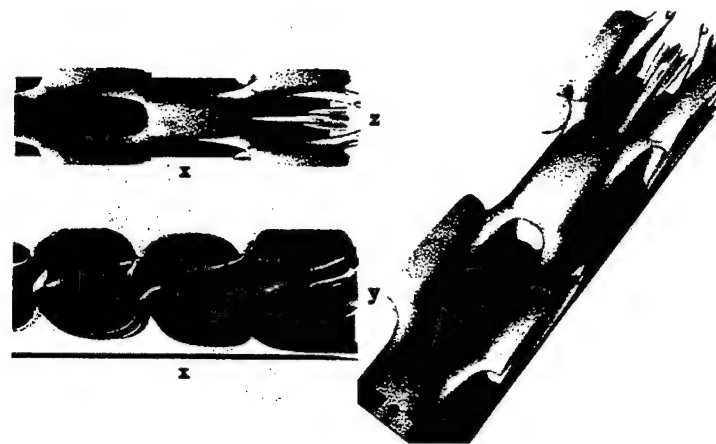
Figure 6.50 Isosurface of $Q = 5$ for case OBLPG between $R_x = 1644$ and $R_x = 1715$.
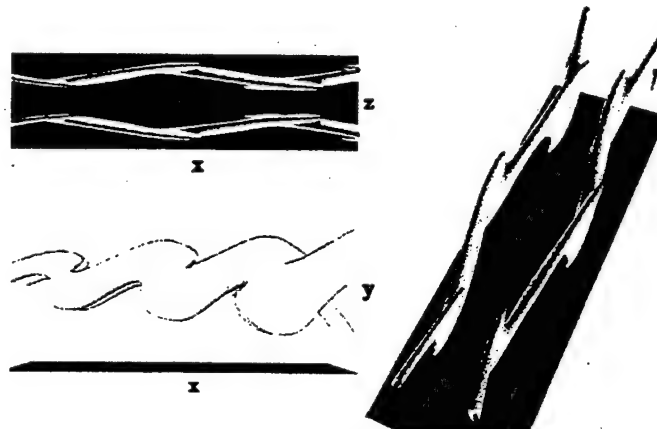
Figure 6.51 Isosurface of $Q = 30$ for case OBLNP4 between $R_x = 1644$ and $R_x = 1715$.

two spikes are coming out of its head for small values of Q. This behavior was also observed in simulation OBLNP3 (however, no plot in the last chapter indicated this because attention was being devoted to different properties of the "X"-shape). Most likely the division of the maximum is caused by the (1,3) mode combination since the calculation with APG does not show this. Nevertheless, detailed investigations have to be performed to prove this statement. The slim structure along the symmetry line in figure 6.50 at the end of the domain can also be observed in the simulation without APG at a lower level of Q. It does not serve as an indication for the differences between both calculations.
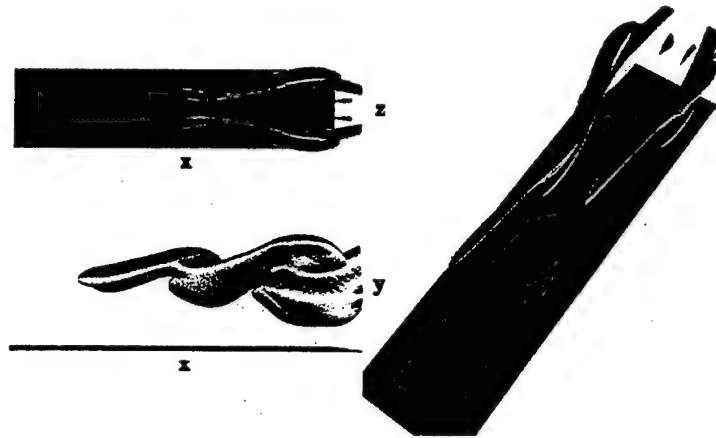
Figure 6.52 Isosurface of $Q = 50$ for case OBLPG between $R_x = 1644$ and $R_x = 1715$.

6.5   Summary of Nonlinear Breakdown Scenarios

An overview of the nonlinear breakdown scenarios we investigated can be found in table 6.7. As already discussed in § 2.3, in addition to the classical subharmonic and fundamental breakdown scenarios of incompressible boundary layers, the so-called "oblique breakdown" may play a role for supersonic boundary layers. For the oblique breakdown, only modes $(1, \pm 1)$ have to be forced. We first discovered the oblique breakdown mechanism for $Ma = 1.6$ (Thumm, 1991), and it was found later that it may also be relevant for $Ma = 4.8$ (Eissler, 1995). Thus, we first needed to confirm if the oblique breakdown was also relevant for the $Ma = 3$ case of the Princeton experiments. Nonlinear transition scenarios for $Ma = 3$ are likely to be more interesting than for $Ma = 1.6$ (albeit also more complicated) because, depending on the local Reynolds number, first and second modes can both be excited linearly and nonlinearly.

In flight vehicles, boundary layers are subject to streamwise pressure gradients, both favorable and adverse. Adverse pressure gradients are more critical as they accelerate transition while favorable pressure gradients delay transition. Therefore, in anticipation of the planned experiments with adverse pressure gradients at the Princeton facility, we started oblique breakdown simulations (under the conditions of the Princeton experiments) to investigate if the oblique breakdown is also relevant for $Ma = 3$ when an adverse pressure gradient is imposed. As is characteristic for the oblique breakdown, only $(1, \pm 1)$ modes are forced, in this case two oblique waves with a wave angle of 65 degrees (most amplified according to linear theory). For the forcing, a blowing and suction slot is used that is located one streamwise wavelength

case	description	forcing
oblique breakdown with and without pressure gradient	$T_\infty = 103.6K$, $\Psi_{1,1} = 65°$ $A_{1,1} = 0.3\%, F_{1,1} = 3 \times 10^{-5}$	
"classical" fundamental breakdown	1st mode, $T_\infty = 103.6K$ $\Psi_{1,1} = 60°$, $F = 5 \times 10^{-5}$ $A_{1,0} = 8\%$, $A_{1,1} = 0.05\%$	
oblique subharmonic breakdown	$T_\infty = 103.6K$ $\Psi_{2,2} = 60°$, $F_{2,2} = 5 \times 10^{-5}$ $\Psi_{1,1} = 60°$, $F_{1,1} = 2.5 \times 10^{-5}$ $A_{2,2} = 0.3\%$, $A_{1,1} = 0.005\%$	
oblique subharmonic breakdown	$T_\infty = 103.6K$ $\Psi_{2,1} = 60°$, $F_{2,1} = 5 \times 10^{-5}$ $\Psi_{1,2} = 81°$, $F_{1,2} = 2.5 \times 10^{-5}$ $A_{2,1} = 0.1\%$, $A_{1,2} = 0.005\%$	
oblique subharmonic breakdown	$T_\infty = 103.6K$ $\Psi_{2,1} = 60°$, $F_{2,1} = 5 \times 10^{-5}$ $\Psi_{1,1} = 74°$, $F_{1,1} = 2.5 \times 10^{-5}$ $A_{2,1} = 0.1\%$, $A_{1,1} = 0.005\%$	

Table 6.7 Overview of breakdown scenarios: $(h, \pm k$, where h is the frequency, k the spanwise Fourier mode; ■ primary wave, ○ secondary wave.

(λ_x) downstream of the inflow boundary. It was shown that for the adverse pressure gradient case (Hartree parameter β_H varied between -0.11 and -0.12 in the computational domain) the nonlinear wave components grow more rapidly than for the zero pressure gradient case, a manifestation that an adverse pressure gradient does not only not interfere with this mechanism but rather enhances it.

To study the mechanisms present in an oblique breakdown in more detail, a high resolution simulation which extended farther into the late stages of transition was also investigated. The oblique modes $(1, \pm 1)$ were rapidly amplified in the downstream direction and, as their amplitudes grew, multiple other modes were generated from nonlinear interactions. Prominent in this respect was the generation of steady longitudinal modes $[(0,2), (0,4), \ldots]$, which are steady vortices. This implies, that steady vortices (such as, for example, those produced by distributed roughness) could also trigger this breakdown mechanism when only very small oblique disturbances are present. Typical flow structures that arise during the later stages of this oblique breakdown scenario were documented in § 6.4. An important observation gained from these simulations is the fact that the nonlinear mechanism of the oblique breakdown sets in at very low amplitudes $(= 0.3\%$ of the free-stream velocity) and thus is a potentially highly relevant breakdown mechanism for $Ma = 3$ at low free-stream turbulence levels (free flight). We therefore recommend strongly future investigations of this mechanism, preferably in collaboration with the Princeton experiments.

In addition to the oblique breakdown, we investigated, if the "classical" fundamental (Klebanoff) breakdown scenario $[(1,0), (1, \pm 1)]$ is also relevant. The amplification curves and the structures resulting from the "classical" fundamental breakdown were shown in § 6.3. However, since much larger amplitudes were required to initiate the fundamental breakdown, it is likely to be relevant only for high free-stream turbulence conditions. Nevertheless, this breakdown mechanism needs to be investigated because of its possible relevance for interpreting experimental measurements from "noisy" (high free-stream turbulence level) facilities. It should be noted that measurements in the Russian experiments for a sharp-nosed cone at $Ma = 6$ (Shiplyuk et al., 2003) indicated that a two-dimensional second-mode subharmonic instability was present. In our Navier–Stokes simulations at $Ma = 3$, resonance occurred at much lower amplitudes for the second-mode "classical" fundamental breakdown scenario than for the first-mode scenario. Therefore, "classical" fundamental and "classical" subharmonic breakdown scenarios are likely important for second-mode disturbances.

In addition to the "classical" nonlinear resonance mechanisms, we investigated other resonance mechanisms that may become relevant due to the fact

that, for supersonic boundary layers, the first-mode oblique disturbances are linearly more amplified than first-mode two-dimensional disturbances (which are most amplified in incompressible flows). Assuming that this behavior also holds for the nonlinear stages, we investigated subharmonic and fundamental nonlinear resonance mechanisms for oblique fundamental waves where both primary and secondary disturbance waves are three-dimensional. For the oblique fundamental resonance, disturbances in the $(1,\pm1)$ modes for the primary waves (amplitudes $= 0.02\%$ of the free-stream velocity) and in the $(1,\pm2)$ modes for the secondary waves (amplitudes $= 0.005\%$ of the free-stream velocity) resulted in a wave angle of 60 degrees and 74 degrees for the primary and secondary waves, respectively. Our results indicate that the oblique fundamental breakdown triggers an essentially "oblique breakdown," however, at even lower disturbance amplitudes than when only one pair of oblique waves is introduced. Simulations with different free-stream temperatures showed that the influence of the free-stream temperature on the nonlinear development is not profound as the onset of transition moves only slightly upstream for $T = 103.6K$ when compared with $T = 300K$. The extent of the nonlinear transition regime is somewhat larger for $T = 103.6K$ than for $T = 300K$. Therefore, an outflow treatment (buffer domain) had to be used for this calculation in order to prevent a "blow up" in the case with $T = 300K$ with equal resolution.

In § 6.3, we also investigated the subharmonic resonance that Kosinov & Tumin (1996) suggested to be relevant in the experiments of a Mach 2 boundary layer. Three different scenarios were considered. First, the primary disturbances $(2,\pm2)$ were excited with an amplitude of 0.3% (of the free-stream velocity), and the secondary disturbances $(1,\pm1)$ had an amplitude of 0.005%. Thus both primary and secondary waves had the same wave angle of $\psi = 60$ degrees. For the second and the third case, secondary waves of different wave angles were combined with a primary wave $(2,\pm1)$ ($\psi = 60$ degrees, amplitude of 0.1%). For the second case, the secondary waves were $(1,\pm2)$ modes with $\psi = 81$ degrees and also disturbed with an amplitude of 0.005%. For the third case, the secondary disturbances were $(1,\pm1)$ modes with an amplitude of 0.005% and $\psi = 74$ degrees. The amplification curves clearly indicated that strong nonlinear interaction can occur. Surprisingly, the oblique subharmonic breakdown produced a more rapid amplitude growth in the downstream direction at lower amplitudes if the primary and the secondary waves are forced with different wave angles than if primary and secondary waves travel with the same wave angle. This is an indication that the wave angle between primary and secondary waves plays an important role for energy transfer from the baseflow to the disturbance waves. The different wave angles between primary and secondary waves also

have an effect on the flow structures during breakdown, in particular also on the spanwise vorticity structures. Again, the experiments in the Princeton tunnel and more detailed numerical investigations need to confirm this.
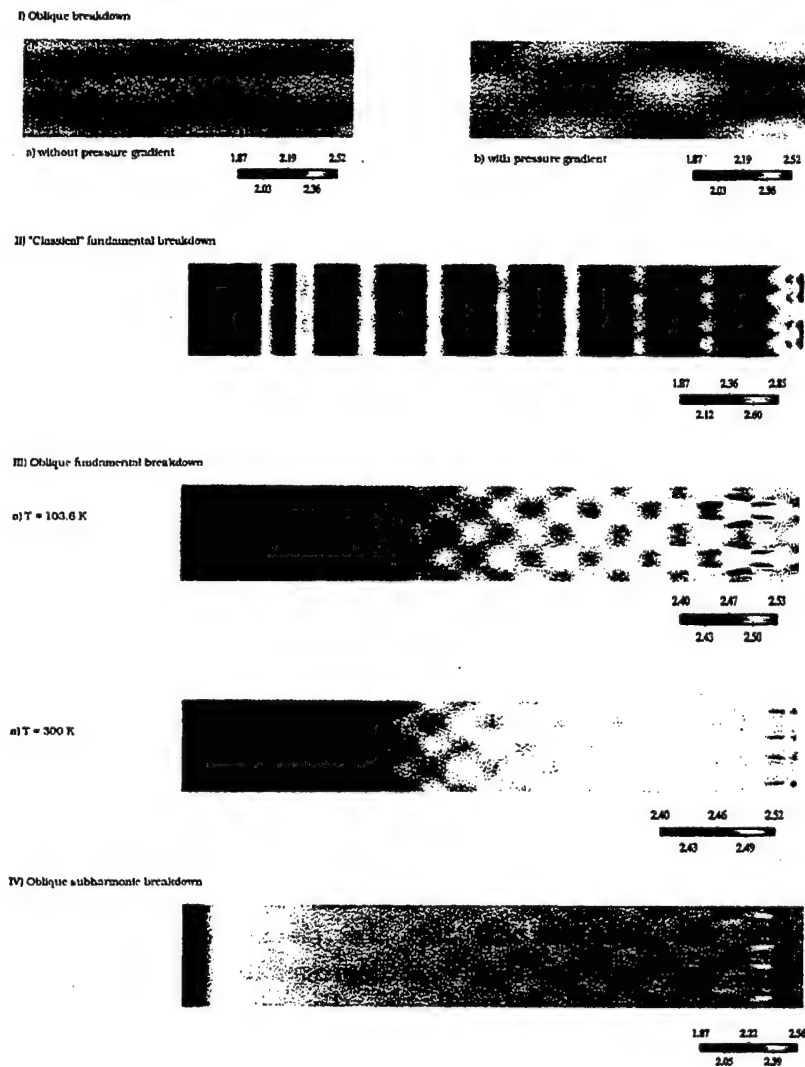
Figure 6.53 Near-wall temperature distribution for different breakdown scenarios. I) Oblique breakdown, $F = 3 \times 10^{-5}$, $T_\infty = 103.6K$. a) without pressure gradient. b)with pressure gradient. II) "Classical" fundamental breakdown, 1st mode, $F = 5 \times 10^{-5}$, $T_\infty = 103.6K$. III) Oblique fundamental breakdown, $F = 2 \times 10^{-5}$. a) $T_\infty = 103.6K$. b) $T_\infty = 300K$. IV) Oblique subharmonic breakdown, $F_{2,1} = 5 \times 10^{-5}$, $F_{1,2} = 2.5 \times 10^{-5}$, $T_\infty = 103.6K$.

As can be seen in figure 6.53, the various breakdown scenarios also leave a strong imprint on the near-wall temperature distribution. This is of significance, of course, as heat loads associated with laminar-turbulent transition are a major concern in the design and safe operation of high-speed flight vehicles. Interesting in this respect is the fact that certain breakdown scenarios such as the oblique and oblique subharmonic resulted in higher temperatures than the various fundamental breakdown scenarios with the "classical" (Klebanoff) breakdown resulting in the lowest temperatures. This may possibly be exploited by alternating the natural transition process using artificial means, such as surface texturing, or changing the design altogether so that certain disadvantageous (from a wall heating point of view) breakdown scenarios are avoided. From an experimental point of view, it is of interest if the various nonlinear breakdown scenarios could be observed with visualization techniques that are realizable for supersonic flows, such as Schlieren techniques. Therefore, in figure 6.54, Schlieren pictures obtained from the various breakdown simulations are shown. Clearly, the different breakdown mechanisms leave a distinct mark on the Schlieren patterns. Notice, for example, the rope-like structures that were observed in the experiments (see Pruett & Chang, 1995). Therefore, when simulations are combined with experiments, dominant breakdown mechanisms may be identified from experimental Schlieren pictures before going into detailed and expensive measurements.
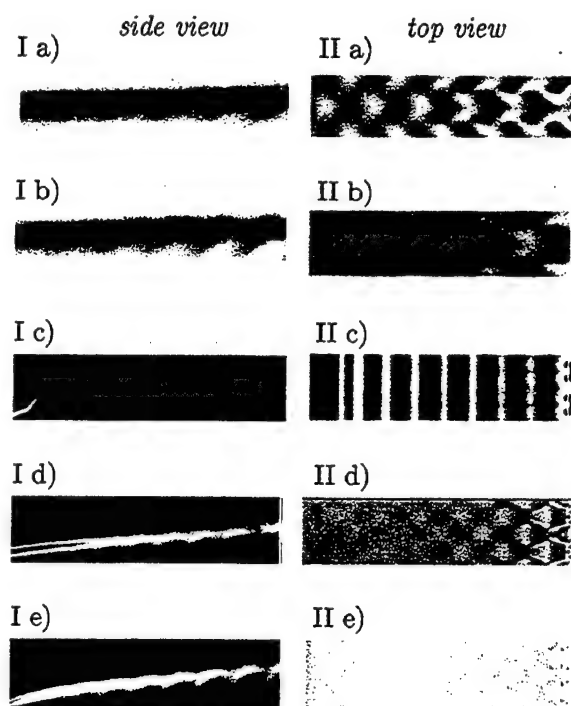
Figure 6.54 Simulated Schlieren pictures of various breakdown mechanisms. Shown are side view of wall-normal density gradient (I) and top view of streamwise density gradient (II): a) oblique breakdown with zero pressure-gradient, b) oblique breakdown with APG, c) classical fundamental breakdown, d) oblique fundamental breakdown, e) oblique subharmonic breakdown.

7. CONCLUSIONS

With the funding from the current AFSOR grant, we focused our numerical simulation efforts on a collaboration with the experiments for a Mach 3 flat-plate boundary layer carried out at Princeton University (G. Brown). Brown and co-workers (see Graziosi, 1999; Graziosi & Brown, 2002) have been performing "natural" and "controlled" transition experiments in the Low Turbulence Variable Geometry wind tunnel. Typical results from our simulations of the "natural" transition experiments were presented in this report. To confirm that simulations and experiments were based on the same "baseflow," the experimental baseflow profiles were compared with our Navier–Stokes results. The agreement was reasonably good, except for the last downstream location which was outside the "quiet" region. The downstream development and the spatial growth rates of the disturbances obtained from the Navier–Stokes computations were compared with the experimental measurements. The agreement was remarkable, considering that the data were from natural transition experiments and considering the difficulties and uncertainties when trying to carry out supersonic stability and transition experiments.

From these and other comparisons of our Navier–Stokes results with experimental data, we are reasonably sure that more challenging transition experiments can be performed in the experimental facility such as, for example, investigations of the nonlinear stages of transition and the onset of the breakdown to turbulence. Towards this end, G. Brown has been developing a technique to allow for "controlled" transition experiments using a loudspeaker upstream of the contraction nozzle to generate controlled (for example single frequency) disturbances (Brown & Fan, 2003). The experimental data obtained so far clearly indicate that "controlled" experiments can indeed be carried out in this facility. In addition, because of the forcing technique employed in these experiments, the receptivity to sound can also be investigated. In order to perform such receptivity investigations, we have already modified our code. Towards this end, we first had to implement free-stream boundary conditions to allow for variable free-stream pressure. To validate the modified code, transition simulations with adverse pressure-gradients for a flat plate were performed at low Mach number ($Ma = 0.1$) and the results were compared to simulations from an incompressible code. Towards the understanding of the nonlinear mechanisms, we simulated numerous nonlinear resonance and breakdown scenarios for a Mach 3 flat-plate boundary layer with and without adverse pressure gradients. The objective of these simulations was to identify scenarios that may be relevant for laboratory and/or realistic flight conditions. With such simulations we can screen

the extremely large parameter space for possible nonlinear interaction and breakdown scenarios so that the most viable and relevant ones can be investigated rigorously in experiments and detailed simulations. This will result in considerable savings of time and experimental costs of future investigations.

APPENDIX A: Code Parallelization

For the present investigation, most simulations have been carried out on machines of the *SGI Origin 3k* series with MIPS 400-700 MHz R12k or R16k processors, IP35 or IP27 architecture and 8 MB cache and *HP Alpha* machines. The efficiency of the parallelization algorithm for these shared memory machines has been tested and it turned out to be high enough to justify the use of up to 400 processors — the maximum number of CPUs possible for the largest problem size investigated. For some calculations even a superlinear speedup could be obtained, i.e., running a simulation with n-times the processors is more than just n-times faster. The reason for this lies in the fact that for smaller computations the memory requirements can exceed the cache of one processor but do not exceed the combined cache available to the n processors. Thus, if feasible, the number of processors was chosen to be sufficiently large for exploiting cache effects.

In order to evaluate the performance of the parallel algorithm, we define the *speedup*

$$Sp = \frac{t(1)}{t(n)} \tag{A.1}$$

and the *parallel efficiency*

$$Ep = \frac{Sp}{n}, \tag{A.2}$$

where $t(n)$ is the elapsed time of the computation using n processors. *Amdahl's law* states that the speedup is limited by the parallel fraction fp of the program:

$$Sp = \frac{1}{\frac{fp}{n} + 1 - fp} < \frac{1}{1 - fp}, \tag{A.3}$$

for $n \to \infty$. A lower bound of the performance of any program can be estimated in millions of floating-point operations per second (MFLOPS).

Program performance on an *SGI Origin 3800* with IP35 architecture is evaluated by computing 200 timesteps of a three-dimensional turbulent boundary layer simulation using 240×130 points and 16 Fourier modes (33 physical points). It represents a typical calculation which includes data input and output. The number of processors are varied and the problem size is kept constant, thus increasing the relative overhead of the parallelization with increasing number of CPUs. The memory requirements for this case are such that more than 33 processors are needed to fit the memory completely into cache, and 40 processors are the maximum possible due to domain length limitations.

Number of CPUs	MFLOPS per process	Total MFLOPS	CPU time [s]	S_p	E_p
1	101	101	2,500	1.0	100%
2	106	212	1,197	2.1	104%
4	94	376	691	3.6	91%
8	90	720	348	7.2	90%
12	89	1068	239	10.5	87%
16	80	1280	198	12.6	79%
20	72	1440	177	14.1	71%
24	77	1848	142	17.6	73%
30	84	2520	106	23.6	79%
36	87	3132	86	29.1	81%
40	85	3400	79	31.7	79%

Table A.1 Program performance on an *SGI Origin 3800* for different numbers of processors and a fixed problem size.

Table A.1 and figure A.1 clearly show that increasing the number of processors incurs a performance penalty because of the additional communication associated with the parallelization. The penalty is visible in the decrease of MFLOPS per processor and parallel efficiency. Nevertheless, overall program performance (speedup and total MFLOPS) is still increasing and computation time is decreasing. Starting with the use of 20 CPUs, the communication penalty is more than compensated by the appearance of cache effects. With increasing number of processors and hence increasing total cache size, more and more of the data can be accessed faster and parallel efficiency increases considerably. At 36 processors all data fit in cache. A further increase in CPUs does not enhance any cache effects and, consequently, can not compensate any concomitant increase in communication penalty. Thus the efficiency decreases again. However, the theoretical lines in figure A.1 show that fitting the data in cache is still equivalent to computing with an algorithm of higher parallel fraction — shifting the maximum speedup to higher values.

In addition to exploiting cache effects, program performance can be enhanced by optimizing the scheduling environment of the multi-processor computer. In figure A.1, results using the system default environment (squares) are compared with a user defined environment (solid circles). For more than four CPUs, the effect of an optimized scheduler is again equivalent to increasing the parallel fraction of the algorithm and hence highly effective in the case of a larger number of processors. Clearly, any time invested in optimizing the scheduler environment is time well spent.
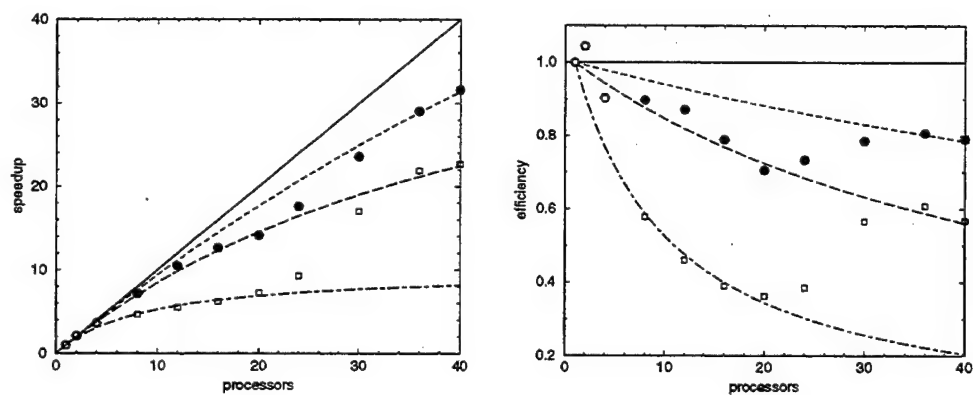
Figure A.1 Speedup (left) and efficiency (right) of parallization on an *SGI Origin 3800*; circles (•) and squares (□) from computation with and without optimized multiprocessing environmental variables, respectively; theoretical lines from *Amdahl's law* with parallel fractions —— 100%, - - - 99.3%, – – 99%, and - ·· - 90%.

APPENDIX B: Grid Convergence Studies

B.1 Linear Stability Investigations
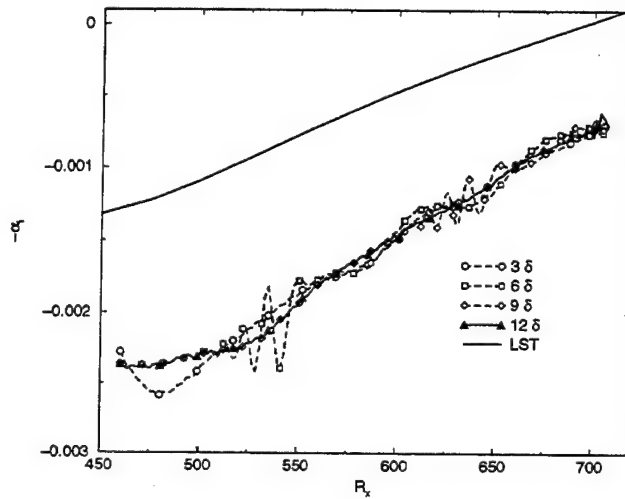
Figure B.1 Influence of different domain heights on amplification rate (32 points per λ_x, 10 points per δ).

B.1.1 Domain Height

Computations with 3, 6, 9 and 12 $\delta_{outflow}$ are carried out to assure that the free-stream boundary is not influencing the results. All other parameters stay the same while the number of points in the y-direction are increased. Figure B.1 shows that three boundary layer thicknesses are too low and, therefore, the amplification rates differ, especially where the wave is highly amplified, from the other three cases. The cases with six and nine boundary layer thicknesses in the domain are identical except the fact that the expansion fan originating from the disturbance slot hits the free-stream boundary later and causes a slight oscillation of the amplification rate farther downstream. For the three boundary layer thickness case, this modulation is farther upstream and therefore not visible in figure B.1.

The domain height can also have an influence on the amplitude and phase distribution. Figure B.2 shows slight deviations of the free-stream ($\eta \geq 10$) only for a domain height of 3 $\delta_{outflow}$.

From these results, a domain height of 6 $\delta_{outflow}$ should be reasonable for further computations, but the oscillations in the amplification rate are unsatisfactory. The computation with 12 $\delta_{outflow}$ is high enough so that the
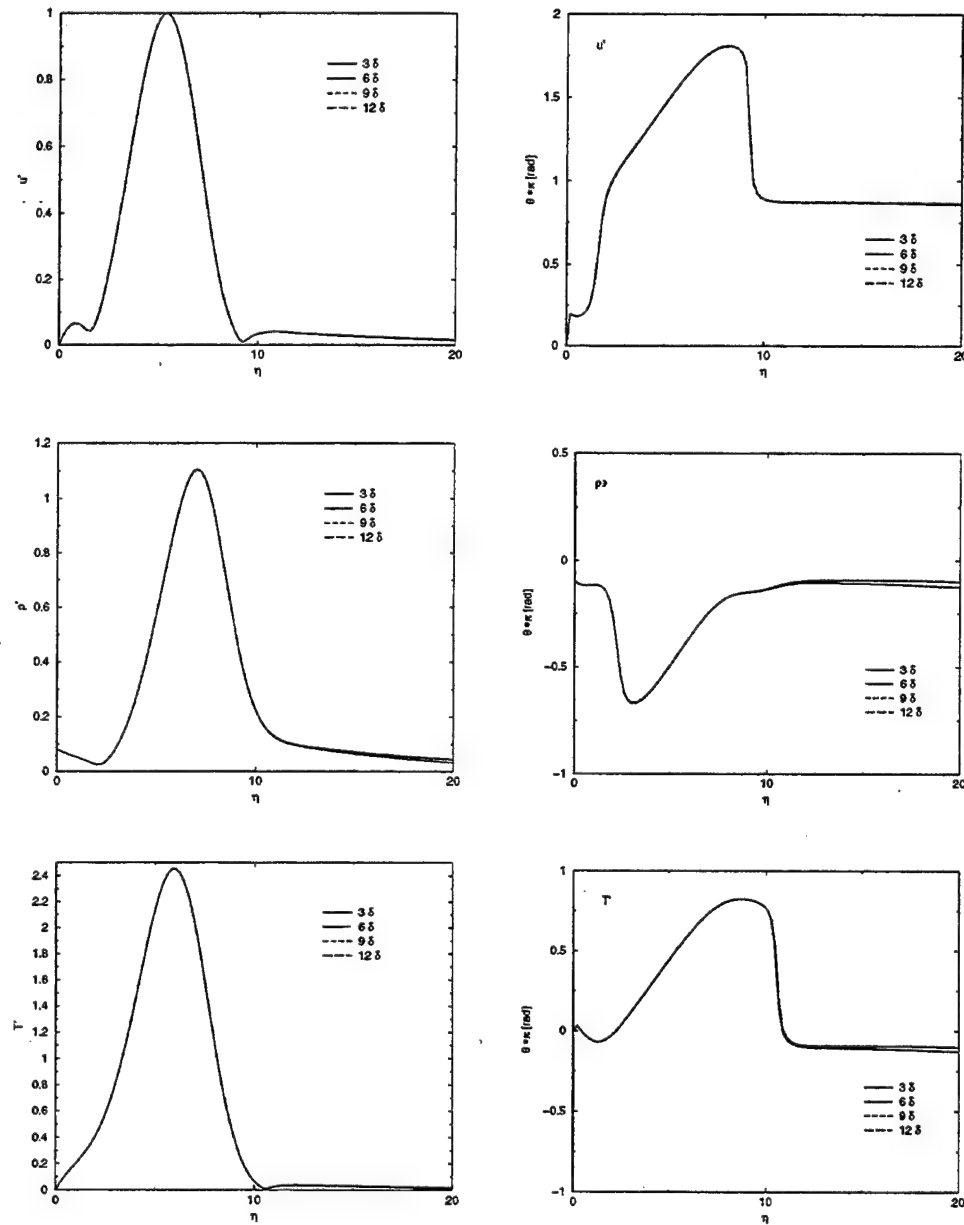
Figure B.2 Influence of different domain heights on the amplitude distributions (left column) and phase (right column) of u', ρ' and T' at $R_x = 500$ (32 points per λ_x, 10 points per δ).

expansion fan does not hit the free-stream and no wiggles are present. It
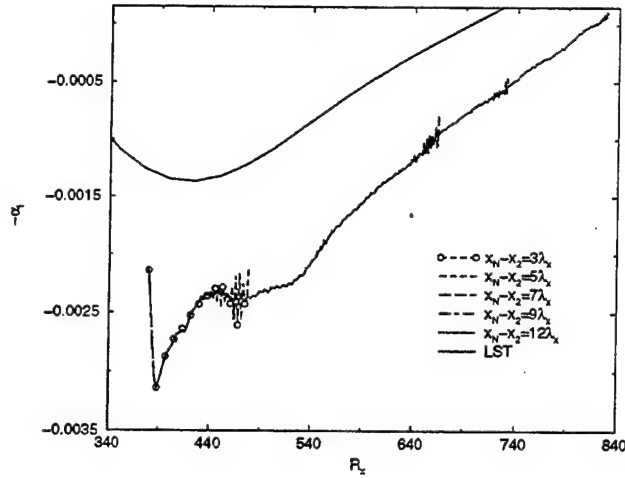
Figure B.3 Influence of the domain length (32 points per λ_x, 10 points per δ, stretched 9 δ high).

shows a perfect alignment with the 9 $\delta_{outflow}$ case upstream of the oscillations. Because of the computational cost an equidistant grid is unreasonable. Therefore, stretched grid studies are also performed (see appendix B.1.7).

B.1.2 Domain Length

To ensure a domain without any interferences of the inflow and outflow boundaries, the overall domain length is under investigation in this section. In figure B.3 all results are perfectly aligned demonstrating that the upstream influence of the outflow is negligible. Figure B.3 also shows that three wavelengths after the disturbance slot (x_2) this wave has not fully developed before propagating out of the domain. The five, seven and nine wavelength cases all coincide leading to the conclusion that the domain length has to be at least 5 λ_x long. Nonetheless, the overall domain length also depends on the region of interest.

B.1.3 Inflow Location

If the inflow boundary is too close to the disturbance slot, a modulation of the amplification rate can be experienced. To exclude this possible influence, four different locations of the inflow are investigated, where the disturbance slot stays at a fixed physical position. Figure B.4 shows that there is no visible difference between the one wavelength-case and the half wavelength case. For a spacing of a quarter wavelength between the disturbance slot
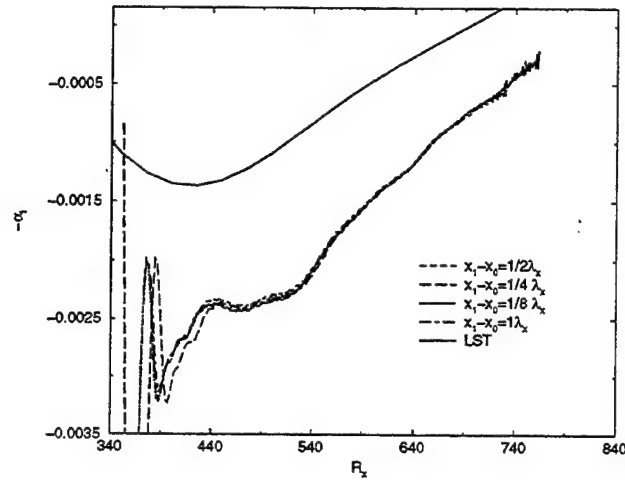
Figure B.4 Influence of the inflow boundary location (32 points per λ_x, 10 points per δ, 9 δ high).

and the inflow boundary, the amplification rate is first larger than for the other cases, but, from $R_x = 500$ on, all amplification rates agree well. For a distance of $\lambda_x/8$, the amplification rate curves do not differ from the case with the largest largest spacing.

B.1.4 Disturbance Slot Location

The influence of the inflow on the amplification rate is investigated by looking at different downstream locations of the disturbance slot. The chosen distances of $\lambda_x/2$, λ_x and $2\lambda_x$ show that the location of the disturbance slot does not significantly influence the amplification rates far downstream (see figure B.5). Farther upstream ($R_x \leq 650$), the differences in the amplification rates show that there is still some adjustment and wave development for the $2\lambda_x$-case. Due to the outcome of the study on different inflow locations (see appendix B.1.3) the differences between the two cases with $\lambda_x/2$ and λ_x stam from the ongoing adjustment of the wave of the λ_x-case. Because the differences of all three cases are within acceptable limits and a farther downstream location is more applicable for this study, a disturbance slot location of one wavelength downstream of the inflow is chosen.

B.1.5 Outflow Location

For the linear stability investigations in 6.2, no relaminarization zone is used because only small amplitudes are under investigation and consequently a
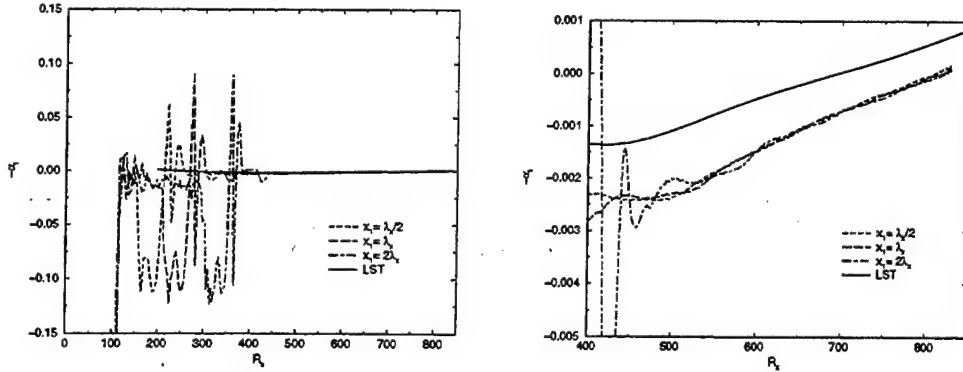
Figure B.5 Influence of the disturbance slot location (32 points per λ_x, 10 points per δ, 9 δ high).
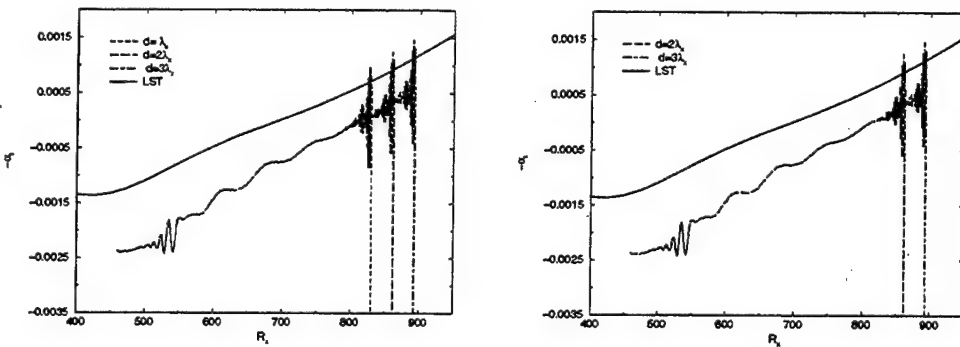
Figure B.6 Upstream influence of the outflow boundary (32 points per λ_x, 10 points per δ, 6 δ high).

buffer zone would only increase the number of points without enlarging the usable domain. Therefore, the upstream influence of the outflow boundary condition has to be examined. For a frequency of $F = 8.1 \times 10^{-5}$, the last point of interest is at about $R_x = 800$. From that point on, the domain is enlarged downstream by 1, 2 and 3 λ_x for this investigation. Figure B.6 shows that two wavelengths are sufficient to avoid any upstream influences.

B.1.6 Wall-Normal Resolution

To investigate how the resolution in the y-direction is influencing the amplification rates, computations with 5, 10 and 15 points per δ_{inflow} are carried out. Figure B.7 shows the low resolution case results in a wrong amplifica-
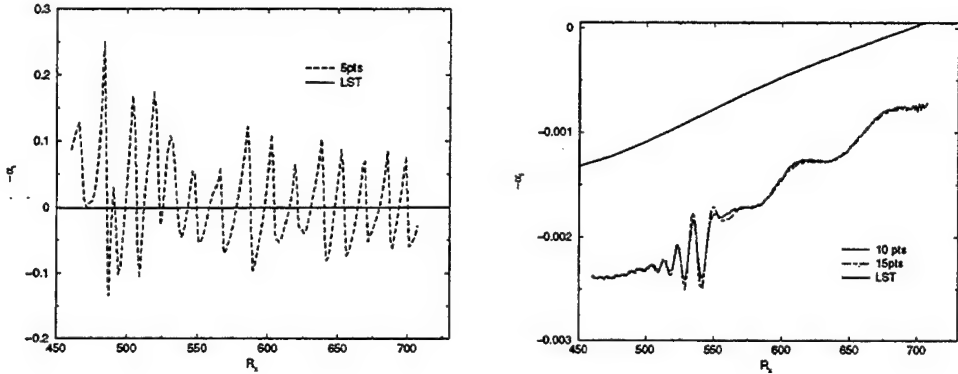
Figure B.7 Low resolution case (left) and higher resolution cases (right) in the y-direction (32 points per λ_x, 6δ high).

tion rate. The two higher resolution cases (see also figure B.7) collapse to one curve suggesting that ten points per δ_{inflow} are sufficient to capture the right amplification rate.

B.1.7 Grid Stretching in the Wall-Normal Direction

Not to influence any physical properties of the flow, the grid is only stretched above two boundary layer thicknesses. Thus, the second maximum of the amplitude distribution remains in the equidistant region. The stretching function enlarges the domain to 6 and 9 $\delta_{outflow}$, keeping the stretching factor constant. Comparing the results to the computations performed on an equidistant grid show that the wiggles of the amplification rate disappeared. The reason for this that the grid stretching introduced an additional damping by an artificial viscosity caused by the stretching function. So the expansion fan hitting the free-stream boundary is an order of magnitude smaller and, therefore, small enough not to influence the amplification rate any more. Nevertheless, the six and nine domain height cases agree well with the 12-$\delta_{outflow}$ case on an equidistant grid (see figure B.8). The lowest domain height for a stretched grid still shows a slight oscillation revealing that the reflection from the shock wave still has a small impact on the amplification rate. The stretched 9 and equidistant 12-$\delta_{outflow}$ cases are in perfect agreement (see figure B.9), hence a domain height of 9 boundary layer thicknesses on a stretched grid is suited for this investigation. To verify that the stretching has no influence on the amplitude and phase distribution, a comparison with the equidistant 12 $\delta_{outflow}$-case is performed (see figure B.10).

The resulting domain height of nine boundary layer thicknesses seems high,
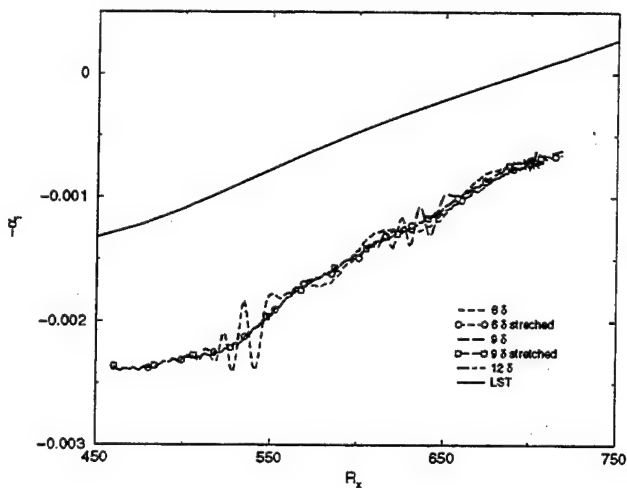
Figure B.8 Comparison of stretched with equidistant grid.
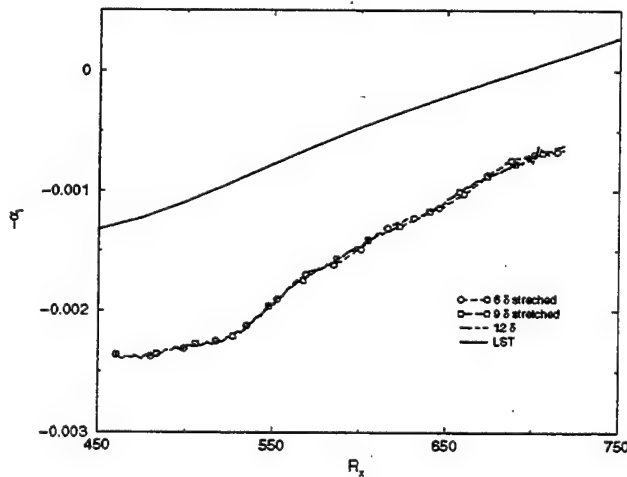
Figure B.9 Comparison of stretched grid to equidistant 12 δ (32 points per λ_x, 10 points per δ).
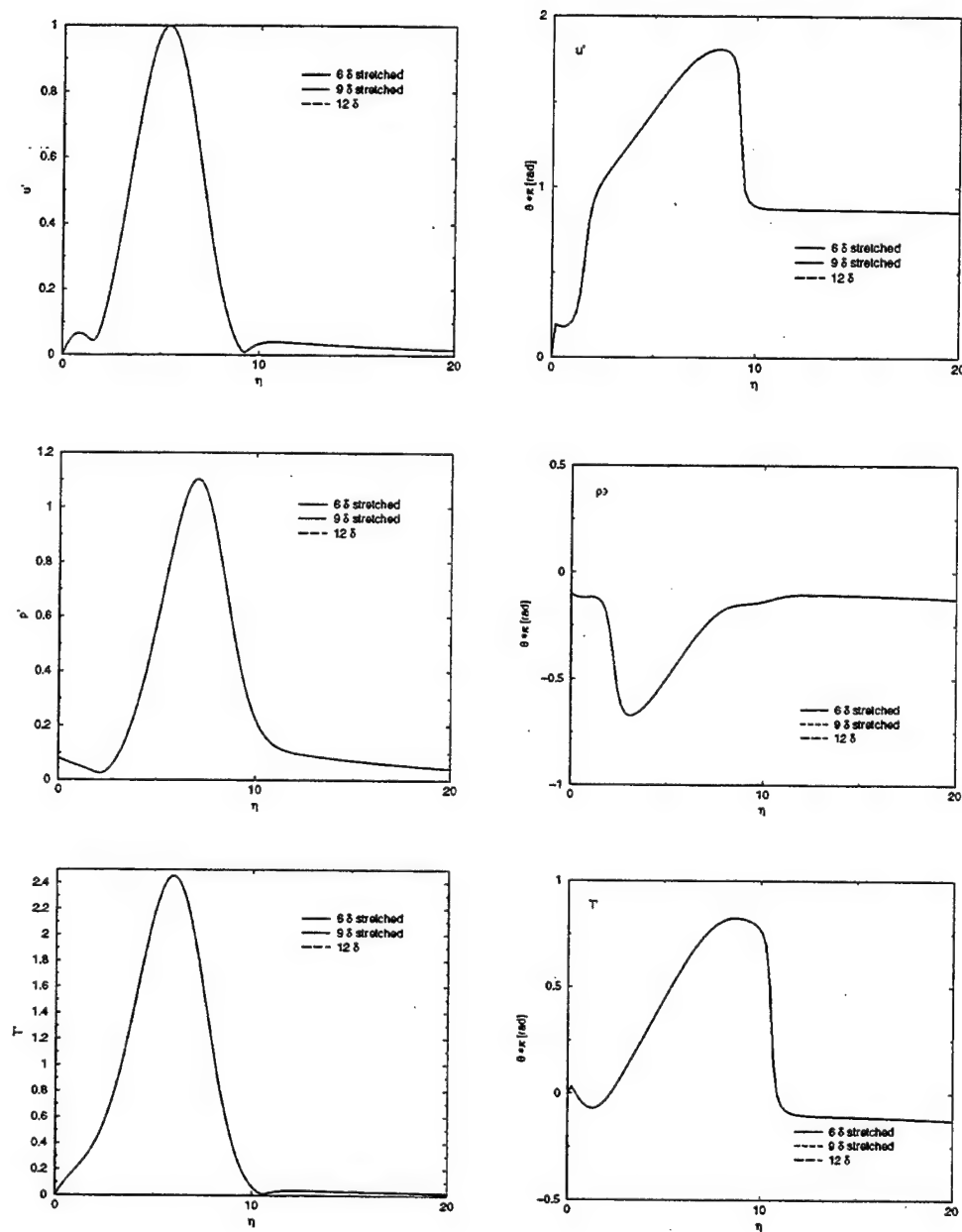
Figure B.10 Influence of the grid stretching on the amplitude distribution (left column) and phase (right column) of u', ρ' and T' at $R_x = 500$ (32 points per λ_x, 10 points per δ).
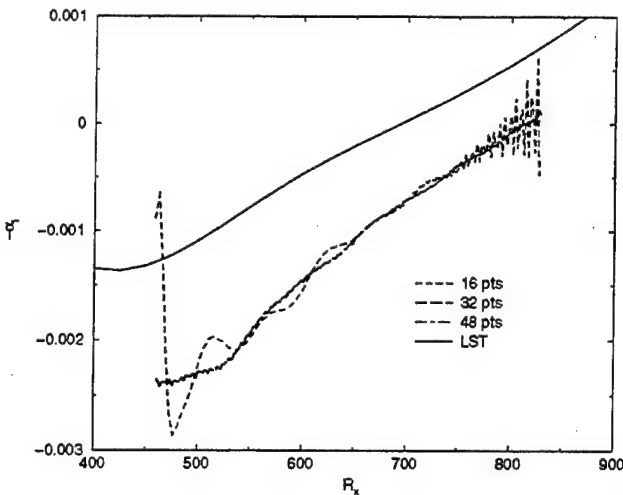
Figure B.11 Influence of resolution in x on the amplification rate on a stretched grid (10 points per δ, 9 δ high).

but as pointed out in section 3.4.4, the flow is assumed to be steady at the free-stream. For the high frequencies under investigation this is a rough approximation, so the domain height increases. The additional damping caused by the stretched grid and the fact that only a third of the points as in the equivalent equidistant case are used, clearly shows that the stretched grid is not only the better choice from a physical point of view but also from a computational point of view, reducing the computation time drastically.

B.1.8 Streamwise Resolution

Computations are performed on a grid which is equidistant over the first two boundary layer thicknesses from the wall and is then stretched to a total height of nine boundary layer thicknesses (chosen in accordance to section B.1.7). The grid in the downstream direction is equidistant. The number of grid points per TS-wavelength are varied to determine the regular resolution. The 16 points per TS-wave case still shows strong oscillations, however, the two higher resolutions are in very good agreement(see figure B.11). Therefore, 32 points per wavelength are chosen in the stability investigations.

B.2 Oblique Breakdown Simulations

For the validation cases and the linear stability investigations, all calculations were performed on an equidistant grid. Since the resolution does not need

to be high to simulate 3D waves in the linear stage, an equidistant grid is not a disadvantage. For oblique breakdown this is not true anymore. When the 3D waves start to interact with each other, smaller structures are being created and these structures need to be resolved. For that reason, a high resolution is required at positions where smaller structures emerge and not further upstream where the 3D waves are in the linear stage. The DNS code used for all presented simulations has the capability to use a stretched grid in the x- and in the y-direction. This feature was applied for all oblique breakdown simulations. Figure B.12 shows the computational grid used for the simulation of case OBLNP2. The grids for all other oblique breakdown simulations (cases OBLNP3, OBLNP4 and OBLPG) are similar. The parameters which are necessary to create such a grid can be found in
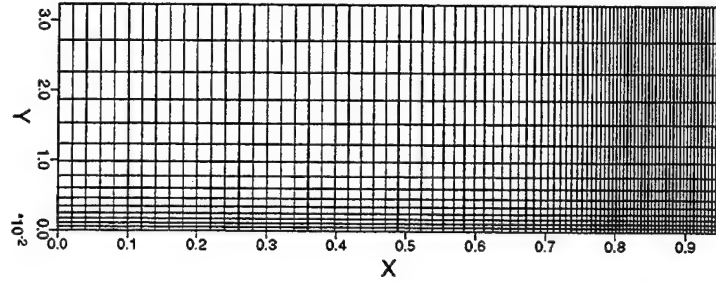
Figure B.12 Computational grid for the simulation OBLNP2. Every fifth point is plotted for clarity.
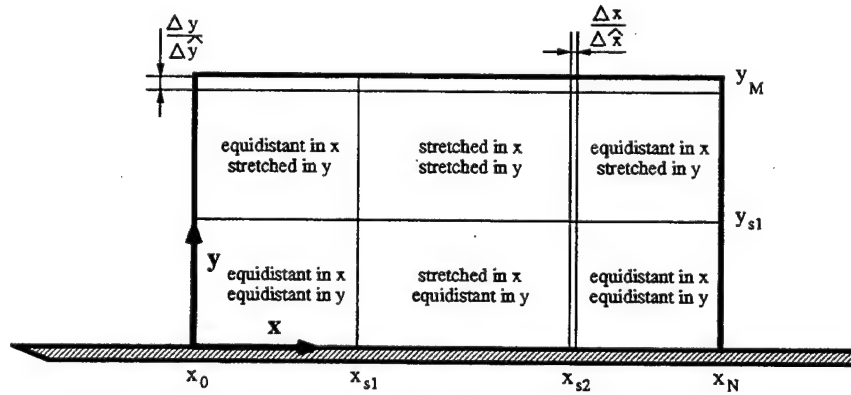
Figure B.13 Parameters for the generation of the computational grid.

figure B.13. For the x-direction, x_{s1} is the location where the stretching starts. The equidistant grid upstream of x_{s1} has the stepsize $\Delta \hat{x}$. At position x_{s2} the stretching ends and downstream of x_{s2} the grid is equidistant again with the stepsize Δx. The stepsize Δx is calculated from the stepsize $\Delta \hat{x}$

and the specified ratio $\Delta x/\Delta \hat{x}$. For the oblique breakdown calculations this ratio is smaller than 1, so that the grid becomes finer with increasing x. For the y-direction, y_{s1} is the location where the stretching starts. The stretching ends at the upper boundary, that means at y_M with the stepsize $\Delta \hat{y} \cdot \Delta y/\Delta \hat{y}$. Simulation OBLNP2 is a test case which was conducted to find out if the grid stretching has an influence on the amplification rate α_i of a 3D disturbance in the linear stage. Case OBLNP1 is a calculation performed on an equidistant grid with a fine resolution. Both calculations have the same flow and forcing properties as the simulations for the supersonic validation. A more detailed summary of the input data for the DNS can be found in appendix C. The amplitude distribution over x of the u-velocity of case OBLNP1 serves as comparison for case OBLNP2. Since the grid of case OBLNP1 is finer than for the supersonic validation cases presented in § 4, the amplitude distribution of case OBLNP1 describes the correct physical behavior. Figure B.14 contains the results of both calculations. The slope of the curves are the same which means that both simulations produce the same amplification rate α_i.
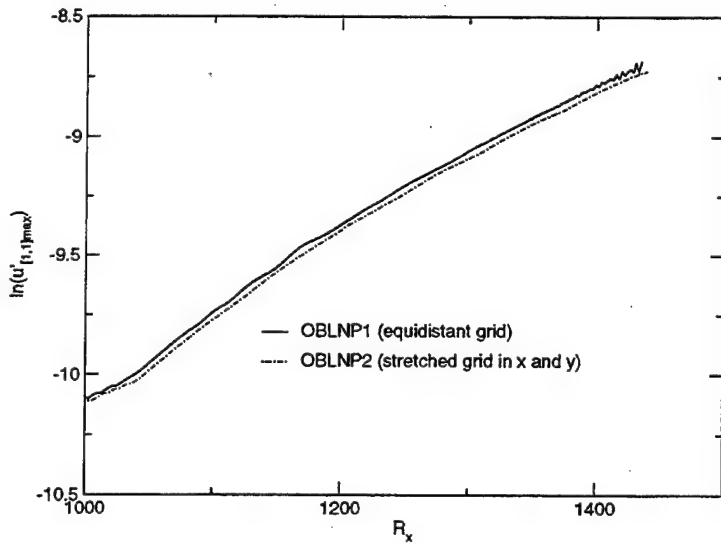
Figure B.14 Amplitude distribution versus x for cases OBLNP1 and OBLNP2.

APPENDIX C: Computational Details

The parameters that are used for the computational simulations are listed in the following tables. All baseflow calculations are performed with adiabatic walls (unless stated otherwise), whereas the (unsteady) forced flow calculations are carried out with isothermal walls, i.e., the baseflow temperature distribution.

	Thumm A1	Eissler C
Physical parameters:		
Ma	1.6	4.8
Re	100,000	100,000
Pr	0.71	0.71
κ	1.4	1.4
T_{wall}	adiabatic	650 K
T'_{wall}	0	0
T_∞	300 K	220 K
p_∞	101.3 kPa	2.5501 kPa
Computational parameters:		
n_x	300	800
n_y	150	121
Δt	0.001256	0.0062831853
Δx	0.03704	0.0238
Δy_{wall}	0.00125	0.007
Δy_{fs}	0.1875	0.007
λ_z	0.4133	0.5711987
x_0	0.225	44.1
$y_{stretch}$	0.125	N/A
y_M	3.0	0.847
x_{ramp}	N/A	51.5
Forcing parameters:		
β	5.0025	10
$A_{1,0}$	0	5×10^{-2}
$A_{1,1}$	5×10^{-5}	1×10^{-3}
x_1	1.44732	44.9568
x_2	1.8332	45.2424

Table C.1 Parameters for the supersonic validation cases of Thumm (1991) and Eissler (1995).

	ICVALDC	ICVALFR	CVALNP	CVALPG
Physical parameters:				
Re	10^5	10^5	1578102	1578102
Ma	0.25	0.1	3.0	3.0
T_∞^*	$300K$	$224K$	$103.6K$	$103.6K$
Pr	0.71	0.71	0.71	0.71
κ	1.4	1.4	1.4	1.4
β_H	0.0	-0.18	0.0	$-0.04...-0.08$
Domain size:				
x_0	0.54	1.585	0.0396	0.5116 (0.0396)
x_N	4.124	5.844	2.2716	2.1036 (3.1920)
y_M	≈ 0.1	0.22	0.0199	0.0199
λ_z	N/A	2.0520×10^{-1}	4.4239×10^{-2}	3.7920×10^{-2}
Buffer domains and decay condition:				
x_{start}^{in}	N/A	1.673	N/A	N/A
x_{end}^{in}	N/A	2.060	N/A	N/A
x_{start}^{out}	N/A	2.800	1.8796	1.7036
x_{end}^{out}	N/A	4.200	2.1756	2.0236
α	37.6	29.8	70.0	74.0
c	N/A	N/A	0.7	0.7
Grid size and resolution:				
n_x	513	506	280	200 (400)
n_y	88	292	200	200
K	0	2	1	1
Δt	1×10^{-4}	4.8481×10^{-5}	3.3179×10^{-5}	3.3179×10^{-5}
$\Delta \hat{x}$	7×10^{-3}	8.4340×10^{-3}	8.0000×10^{-3}	8.0000×10^{-3}
$\Delta \hat{y}$	5×10^{-4}	5.7300×10^{-4}	1.0000×10^{-4}	1.0000×10^{-4}
Forcing parameters:				
β	14.0	10.8	47.343	47.343
$A_{1,0}$	1×10^{-4}	1×10^{-6}	N/A	N/A
$A_{1,1}$	N/A	2×10^{-6}	1×10^{-6}	1×10^{-12}
x_1	0.82	2.082	0.2236	0.6956
x_2	0.89	2.293	0.2716	0.7436

Table C.2 Parameters for the pressure-gradient validation cases; baseflow computations are carried out in 2D, values which differ otherwise are given in brackets; pressure-gradient parameters for case CVALPG are: $x_3 = 0.6$, $x_4 = 2.0$, $x_5 = 2.6$, $\Delta p_1 = 0.8$, $\Delta p_2 = 0.6$ and $transdx = 0.1$.

	$F = 1.4 \cdot 10^{-5}$	$F = 5.0 \cdot 10^{-5}$	$F = 8.1 \cdot 10^{-5}$
Physical parameters:			
Ma	3.0	3.0	3.0
Re	1,578,102	1,578,102	1,578,102
Pr	0.71	0.71	0.71
κ	1.4	1.4	1.4
T_{wall}	adiabatic	adiabatic	adiabatic
T'_{wall}	0	0	0
T_∞	103.6 K	103.6 K	103.6 K
p_∞	0.7508 kPa	0.7508 kPa	0.7508 kPa
Computational parameters:			
n_x	400	280	434
n_y	236	328	182
Δt	$5.636138 \cdot 10^{-5}$	$1.61085 \cdot 10^{-5}$	$4.973063 \cdot 10^{-5}$
Δx	$4.20175 \cdot 10^{-3}$	$1.6228 \cdot 10^{-3}$	$1.07456 \cdot 10^{-3}$
Δy_{wall}	$9.72584 \cdot 10^{-5}$	$3.51 \cdot 10^{-5}$	$6.3776 \cdot 10^{-5}$
Δy_{fs}	$9.72584 \cdot 10^{-5}$	$2.2113 \cdot 10^{-3}$	$1.721952 \cdot 10^{-3}$
λ_z	0.0970526	0.0299817	0.0198527
x_0	0.017836	$1.591725 \cdot 10^{-3}$	$6.3669 \cdot 10^{-3}$
$y_{stretch}$	N/A	$9.7578 \cdot 10^{-3}$	$8.3706 \cdot 10^{-3}$
y_M	0.022953	0.047	0.0392
Forcing parameters:			
β	22.29607	78.0107	126.34437
$A_{1,1}$	$5 \cdot 10^{-4}$	$5 \cdot 10^{-5}$	$5 \cdot 10^{-4}$
x_1	0.08086225	0.027556525	0.04075282
x_2	0.101871	0.040519725	0.05794578

Table C.3 Parameters for the simulations for comparison with the experiments of Graziosi (1999) and Graziosi & Brown (2002).

	$F = 5.0 \cdot 10^{-5}$	$F = 8.1 \cdot 10^{-5}$	$F = 1.5 \cdot 10^{-4}$	$F = 2.0 \cdot 10^{-4}$
Physical parameters:				
Ma	3.0	3.0	3.0	3.0
Re	1,578,102	1,578,102	1,578,102	1,578,102
Pr	0.71	0.71	0.71	0.71
κ	1.4	1.4	1.4	1.4
T_{wall}	adiabatic	adiabatic	adiabatic	adiabatic
T'_{wall}	0	0	0	0
T_∞	103.6 K	103.6 K	103.6 K	103.6 K
p_∞	0.7508 kPa	0.7508 kPa	0.7508 kPa	0.7508 kPa
Computational parameters:				
n_x	600	570	384	384
n_y	174	134	180	224
Δt	$8.05426 \cdot 10^{-5}$	$4.973063 \cdot 10^{-5}$	$2.651 \cdot 10^{-5}$	$1.9899 \cdot 10^{-5}$
Δx	$1.6228 \cdot 10^{-3}$	$1.07456 \cdot 10^{-3}$	$7.3125 \cdot 10^{-4}$	$4.63 \cdot 10^{-4}$
Δy_{wall}	$1.3299 \cdot 10^{-4}$	$1.40307 \cdot 10^{-4}$	$6.63 \cdot 10^{-5}$	$3.536 \cdot 10^{-5}$
Δy_{fs}	$7.9794 \cdot 10^{-3}$	$2.806144 \cdot 10^{-3}$	$4.641 \cdot 10^{-3}$	$6.3648 \cdot 10^{-3}$
λ_z	0.0299817	0.0198527	0.01351	$8.55384 \cdot 10^{-3}$
x_0	0.3105	0.0254676	$1.591725 \cdot 10^{-3}$	$1.591725 \cdot 10^{-3}$
$y_{stretch}$	0.0170227	0.017858	$8.619 \cdot 10^{-3}$	$6.15264 \cdot 10^{-3}$
y_M	0.143	0.0631	0.087	0.111
Forcing parameters:				
β	78.0107	126.34437	237	315.758
$A_{1,1}$	$5 \cdot 10^{-5}$	$5 \cdot 10^{-4}$	$5 \cdot 10^{-5}$	$5 \cdot 10^{-5}$
x_1	0.3624296	0.05985352	0.024991725	$8.9997 \cdot 10^{-5}$
x_2	0.3883944	0.07704648	0.036691725	0.01641325

Table C.4 Parameters for the simulations for investigation of non-parallel effects.

	OBLNP1	OBLNP2	OBLNP3	OBLNP4	OBLPG
Physical parameters:					
Re	1578102	1578102	1578102	1578102	1578102
Ma	3.0	3.0	3.0	3.0	3.0
T_∞^*	$103.6K$	$103.6K$	$103.6K$	$103.6K$	$103.6K$
Pr	0.71	0.71	0.71	0.71	0.71
κ	1.4	1.4	1.4	1.4	1.4
β_H	0.0	0.0	0.0	0.0	≈ -0.12
Domain size:					
x_0	0.35644	0.35644	0.35644	0.95244	0.95244 (0.35644)
x_N	1.31244	1.31211	1.3095	2.01177	2.01177 (2.48277)
y_M	0.0369	0.03687	0.0366	0.037	0.037
λ_z	4.10×10^{-2}	4.10×10^{-2}	4.10×10^{-2}	4.10×10^{-2}	3.73×10^{-2}
Buffer domains and decay condition:					
x_{start}^{out}	N/A	N/A	1.20644	1.86277	1.86277
x_{end}^{out}	N/A	N/A	1.30644	2.00277	2.00277
α	70.0	70.0	70.0	70.0	78.5
c	0.7	0.7	0.7	0.7	0.7
Grid size, resolution and stretching:					
n_x	240	430	585	550	550 (1170)
n_y	370	80	130	140	140
K	1	1	54	15	15
Δt	1.33×10^{-4}	1.33×10^{-4}	1.33×10^{-4}	1.33×10^{-4}	1.33×10^{-4}
$\Delta \hat{x}$	4×10^{-3}	4×10^{-3}	4×10^{-3}	4×10^{-3}	4×10^{-3}
$\Delta \hat{y}$	1×10^{-4}	1×10^{-4}	1×10^{-4}	1×10^{-4}	1×10^{-4}
x_{s1}	N/A	0.63244	0.63244	1.25644	1.25644
x_{s2}	N/A	1.18044	1.18044	1.74044	1.74044
$\frac{\Delta x}{\Delta \hat{x}}$	N/A	0.25	0.125	0.25	0.25
y_{s1}	N/A	0.0	0.005	0.0	0.0
$\frac{\Delta y}{\Delta \hat{y}}$	N/A	12.0	10.0	6.0	6.0
Forcing parameters:					
β	47.343	47.343	47.343	47.343	47.343
$A_{1,1}$	10^{-5}	10^{-5}	0.003	0.0054	0.0014
x_1	0.54444	0.54444	0.54444	1.12444	1.12444
x_2	0.62444	0.62444	0.62444	1.19644	1.19644

Table C.5 Parameters for the oblique breakdown simulations; baseflow computations are carried out in 2D, values which differ otherwise are given in brackets; pressure-gradient parameters for case OBLPG are: $x_3 = 1.15644$, $x_4 = 1.97244$, $x_5 = 2.27644$, $\Delta p_1 = 0.53$, $\Delta p_2 = 0.53$ and $transdx = 0.1$.

References

ADAMS, N. A. & KLEISER, L. 1993 Numerical simulation of transition in a compressible flat plate boundary layer. In *Transitional and Turbulent Compressible Flows* (ed. L. D. Kral & T. A. Zang), *FED* 151, pp. 101–110. ASME.

BAYLISS, A., MAESTRELLO, L., PARIKH, P. & TURKEL, E. 1985 Wave phenomena in a high reynolds number compressible boundary layer. In *Stability for Time Dependent and Spatially Varying Flows* (ed. D. L. Dwoyer & M. Y. Hussaini), pp. 188–205. Springer.

BERTOLOTTI, F. P. 1991 Compressible boundary layer stability analyzed with the PSE equations. *AIAA Paper 91-1637* .

BERTOLOTTI, F. P., HERBERT, T. & SPALART, P. R. 1992 Linear and nonlinear stability of the Blasius boundary layer. *J. Fluid Mech.* **242**, 441–471.

BESTEK, H. & EISSLER, W. 1996 Direct numerical simulation of transition in Mach 4.8 boundary layers at flight conditions. In *Engineering Turbulence Modelling and Experiments 3* (ed. Rodi & Bergeles). Elsevier Science.

BROWN, G. & FAN, X. 2003 Experiments on the receptivity of a Mach 3 laminar boundary layer to acoustic, pure tone forcing. *Tech. Rep.* 49620-1-0040. AFSOR.

CAVALIERI, D. A. 1995 On the experimental design for instability analysis on a cone at Mach 3.5 and 6.0 using a corona discharge perturbation method. Master's thesis, Illinois Institute of Technology.

CHANG, C.-L. & MALIK, M. R. 1993 Linear and nonlinear PSE for compressible boundary layers. *Tech. Rep.* CR-191537. NASA.

CHANG, C.-L., MALIK, M. R., ERLEBACHER, G. & HUSSAINI, M. Y. 1991 Compressible stability of growing boundary layers using parabolized stability equations. *AIAA Paper* **91-1636**.

CHEN, F.-J., MALIK, M. R. & BECKWITH, I. E. 1989 Boundary-layer transition on a cone and flat plate at Mach 3.5. *AIAA J.* **27**, 687–693.

CHENG, F., ZHONG, X., GOGINENI, S. & KIMMEL, R. 2003 Magnetic effects on second-mode instability of a weakly ionized Mach 4.5 boundary layer. *Phys. Fluids A* **15** (7), 2020–2040.

CHONG, M. S., PERRY, A. E. & CANTWELL, B. J. 1990 A general classification of three-dimensional flow fields. *Phys. Fluids A* **2** (5), 765–777.

DINAVAHI, S. P. G. & PRUETT, C. D. 1993 Analysis of direct numerical simulation data of a Mach 4.5 transitional boundary-layer flow. In *Transitional and Turbulent Compressible Flows* (ed. L. D. Kral & T. A. Zang), *FED* 151, pp. 147–153. ASME.

EISSLER, W. 1995 Numerische Untersuchungen zum laminar-turbulenten Strömungsumschlag in Überschallgrenzschichten. PhD thesis, Universität Stuttgart.

EISSLER, W. & BESTEK, H. 1996 Spatial numerical simulations of linear and weakly nonlinear wave instabilities in supersonic boundary layers. *Theoret. Comput. Fluid Dyn.* **8**, 219–235.

EL-HADY, N. M. 1991 Spatial three-dimensional secondary instability of compressible boundary-layer flows. *AIAA J.* **29**, 688–696.

EL-HADY, N. M. 1992 Secondary instability of high-speed flows and the influence of wall cooling and suction. *Phys. Fluids A* **4**, 727–743.

ERLEBACHER, G. & HUSSAINI, M. Y. 1990 Numerical experiments in supersonic boundary-layer stability. *Phys. Fluids A* **28**, 94–104.

FASEL, H. 1976 Investigation of the stability of boundary layers by a finite-difference model of the Navier-Stokes equations. *J. Fluid Mech.* **78**, 355.

FASEL, H., THUMM, A. & BESTEK, H. 1993 Direct numerical simulation of transition in supersonic boundary layer: Oblique breakdown. In *Transitional and Turbulent Compressible Flows* (ed. L. D. Kral & T. A. Zang), *FED* 151, pp. 77–92. ASME.

FASEL, H. F. & KONZELMANN, U. 1990 Non-parallel stability of a flat-plate boundary layer using the complete Navier-Stokes equations. *J. Fluid Mech.* **221**, 311–347.

FASEL, H. F. & SARIC, W. S., ed. 2000 *Laminar–Turbulent Transition*. Springer.

FORCE, D. S. B. T. 1992 Report on the national aerospace plane program. AD-A274530 94-00052. Defense Science Board.

GRAZIOSI, P. 1999 An experimental investigation on stability and transition at Mach 3. PhD thesis, Princeton University.

GRAZIOSI, P. & BROWN, G. L. 2002 Experiments on stability and transition at Mach 3. *J. Fluid Mech.* **472**, 83–124.

HARRIS, P. J. 1997 Numerical investigation of transitional compressible plane wakes. PhD thesis, The University of Arizona.

HERBERT, T. 1994 Parabolized stability equations. AGARD Report 793. Advisory Group for Aerospace Research and Development.

HINGST, U. G. 1990 Laminar/turbulent flow transition effects on high speed missile domes. AGARD Report CP 493. Advisory Group for Aerospace Research and Development.

JOHNSON, H. B., CANDLER, G. V. & HUDSON, M. L. 1997 Numerical study of hypersonic boundary layer transition on a blunt body. *AIAA Paper* **97-0554**.

KENDALL, J. M. 1975 Wind tunnel experiments relating to supersonic and hypersonic boundary-layer transition. *AIAA J.* **13**, 290–299.

KLEISER, L. & ZANG, T. 1991 Numerical simulation of transition in wall-bounded shear flows. *Ann. Rev. Fluid Mech.* **23**, 495–537.

KLOKER, M. 1993 Direkte Numerische Simulation des laminar-turbulenten Strömungsumschlages in einer stark verzögerten Grenzschicht. PhD thesis, Universität Stuttgart.

KOREJWO, H. A. & HOLDEN, M. S. 1992 Ground test facilities for aerothermal and aero-optical evaluation of hypersonic interceptors. *AIAA Paper* **92-10744**.

KOSINOV, A. & TUMIN, A. 1996 Resonance interaction of wave trains in supersonic boundary layer. In *IUTAM Symposium on Nonlinear Instability and Transition in Three-Dimensional Boundary Layers* (ed. P. W. Duck & P. Hall), pp. 379–388. Kluwer Academic Publishers.

KOSINOV, A. D., MASLOV, A. A. & SHEVELKOV, S. G. 1990 Experiments on the stability of supersonic laminar boundary layers. *J. Fluid Mech.* **219**, 621–633.

LAUFER, J. & VREBALOVICH 1960 Stability and transition of a supersonic laminar boundary layer on an insulated flat plate. *J. Fluid Mech.* **9**, 257–299.

MACK, L. M. 1969 Boundary-layer stability theory. Internal Document 900-277. Jet Propulsion Laboratory, Pasadena, California.

MACK, L. M. 1975 Linear stability theory and the problem of supersonic boundary-layer transition. *AIAA J.* **13**, 278–289.

MACK, L. M. 1984 Boundary-layer linear stability theory. AGARD Report 709. Advisory Group for Aerospace Research and Development.

MACK, L. M. 2000 Early history of compressible linear stability theory. In *Laminar–Turbulent Transition* (ed. H. F. Fasel & W. S. Saric), pp. 9–34. Springer.

MALIK, M. R. 1989 Prediction and control of transition in supersonic and hypersonic boundary layers. *AIAA J.* **27**, 1487–1493.

MASAD, J. A. & NAYFEH, A. H. 1990 Subharmonic instability of compressible boundary layers. *Phys. Fluids A* **2**, 1380–1392.

MEITZ, H. 1996 Numerical investigation of suction in a transitional flat-plate boundary layer. PhD thesis, The University of Arizona.

NG, L. & ERLEBACHER, G. 1992 Secondary instabilities in compressible boundary layers. *Phys. Fluids A* **4**, 710–726.

NORMAND, X. & LESIEUR, M. 1992 Direct and large-eddy simulations in the compressible boundary layer. *Theoret. Comput. Fluid Dyn.* **3**, 231–252.

PARIKH, P. G. & NAGEL, A. L. 1990 Application of laminar flow control to supersonic transport configurations. Technical Report CR-181917. NASA.

PRUETT, C. D. & CHANG, C.-L. 1993 A comparison of PSE and DNS for high-speed boundary-layer flows. In *Transitional and Turbulent Compressible Flows* (ed. L. D. Kral & T. A. Zang), *FED* 151, pp. 57–67. ASME.

PRUETT, C. D. & CHANG, C.-L. 1995 Spatial direct numerical simulation of high-speed boundary-layer flows-part II: Transition on a cone in Mach 8 flow. *Theoret. Comput. Fluid Dyn.* **7**, 397–424.

PRUETT, C. D. & ZANG, T. A. 1992 Direct numerical simulation of laminar breakdown in high-speed, axisymmetric boundary layers. *Theoret. Comput. Fluid Dyn.* **3**, 345–367.

PRUETT, C. D., ZANG, T. A., CHANG, C.-L. & CARPENTER, M. H. 1995 Spatial direct numerical simulation of high-speed boundary-layer flows-part I: Algorithmic considerations and validation. *Theoret. Comput. Fluid Dyn.* **7**, 49–76.

REED, H. L. 1993 Direct numerical simulation of transition: The spatial approach. AGARD Report 793. AGARD-FDP-VKI Special Course.

SCHLICHTING, H. & GERSTEN, K. 2000 *Boundary Layer Theory*, 8th edn. Berlin: Springer.

SCHNEIDER, S. P., COLLICOTT, S. H., SCHMISSEUR, J. D., LADOON, D., RANDALL, L. A., MUNRO, S. E. & SALYER, T. R. 1996 Laminar-turbulent transition research in the Purdue Mach-4 quiet-flow Ludwieg tube. *AIAA Paper* **96-2191**.

SCOTT, W. 1996 USAF, NASA programs to push hypersonic boundaries. *Aviation Week and Space Technology* pp. 22–23.

SHIPLYUK, A., BOUNTIN, D., MASLOV, A. & CHOKANI, N. 2003 Non-linear mechanisms of the initial stage of laminar-turbulent tansition at hypersonic velocities. *Journal of Mechanics and Technical Physics* **44** (5), 1–12.

STETSON, K. F. 1988 On nonlinear aspects of hypersonic boundary-layer stability. *AIAA J.* **26**, 883–885.

STETSON, K. F. 1990 Hypersonic transition testing in wind tunnels. In *Instability and Transition* (ed. M. Y. Hussaini & R. G. Voigts), , vol. I, pp. 91–100. Springer.

STETSON, K. F. & KIMMEL, R. L. 1992*a* Example of second-mode instability dominance at a Mach number of 5.2. *AIAA J.* **30**, 2974–2976.

STETSON, K. F. & KIMMEL, R. L. 1992*b* On hypersonic boundary-layer stability. *AIAA Paper* **92-0737**.

STETSON, K. F. & KIMMEL, R. L. 1993 On the breakdown of a hypersonic laminar boundary layer. *AIAA Paper* **93-0896**.

STETSON, K. F., THOMPSON, E. R., DONALDSON, J. C. & SILER, L. G. 1983 Laminar boundary layer stability experiments on a cone at Mach 8; part I: Sharp cone. *AIAA Paper* **83-1761**.

VON TERZI, D. A. 2004 Numerical investigation of transitional and turbulent backward-facing step flows. PhD thesis, The University of Arizona.

THUMM, A. 1991 Numerische Untersuchungen zum laminar-turbulenten Strömungsumschlag in transsonischen Grenzschichtströmungen. PhD thesis, Universität Stuttgart.

WENDT, V. 1993 Experimentelle Untersuchung der Instabilität von ebenen und konischen laminaren Hyperschallgrenzschichten. DLR-FB 93-56. DLR, Göttngen, Germany.

ZANG, T. A., CHANG, C.-L. & NG, L. L. 1992 The transition prediction toolkit: LST, SIT, PSE, DNS, and LES. *Fifth Symposium on Numerical and Physical Aspects of Aerodynamic Flows* .

ZHONG, X. 2001 Leading-edge receptivity to free-stream disturbance waves for hypersonic flow over a parabola. *J. Fluid Mech.* **441**, 315–367.